

IEEE

microwave

for the Microwave & Wireless Engineer

MAGAZINE

Volume 22 • Number 3 • March 2021



Digital Signal Processing for RFID





IEEE Journal of Microwaves

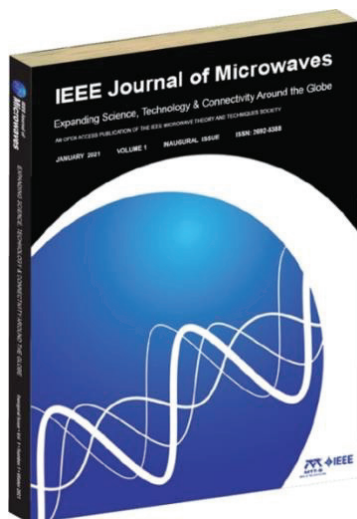
"Expanding science, technology and connectivity across the globe."

If you liked our January Inaugural Issue of *IEEE Journal of Microwaves* you will not want to miss our April issue – scheduled for release on the 15th of the month.

In Volume 1, Issue 2 of our new Open Access journal, we are continuing our special series articles including: *Microwave Pioneers* – this issue on RF-over-wireless entrepreneur and scientist, Professor Kam Lau, "*μWaves Meet Photons*," and our *Microwaves are Everywhere* feature with an enjoyable diversion, "*Ovens: from Magnetrons to Metamaterials*." We are also introducing a new continuing series, *Breakthroughs in Microwaves*, with a special article titled, "*Increasing Signal Strength in Swarms of Wireless Sensors - An Interview with Aydin Babakhani*."

Planned Invited paper topics include: Microwave Acoustics, SAR Imaging, Balloon Millimeter- and Sub-Millimeter-Wave Limb Sounding, Microwave Metrology, Non-Lethal Microwave Weapons, Microwave Sensing for Health Monitoring, Human Body Coupling of 5G, Innovations in Millimeter-Wave Integrated Circuit Packaging, THz Communications Transceivers, Millimeter-Wave FMCW Radar, Advances in High Frequency Electromagnetic Modelling, 3D Printing for Microwave Applications, Software-Defined Radios, Microwave Metasurfaces *and more*. We are also publishing our first batch of unsolicited manuscripts covering all areas of microwave science, technology and applications.

You can still (while supplies last) get a FREE copy of our 500+ page INAUGURAL ISSUE mailed directly to you by signing up at: <https://mtt.org/publications/journal-of-microwaves/inaugural-issue>



Learn more about the *IEEE Journal of Microwaves*

[HOME PAGE](https://mtt.org/publications/journal-of-microwaves) (<https://mtt.org/publications/journal-of-microwaves>)

[Manuscript Submission](#) (link above plus append: /manuscript-submission/)

[Author Information](#) (HOME PAGE plus append: /information-for-authors/)

[Editorial Board](#) (HOME PAGE plus append: /editorial-board/)

Play a part in our future by following our progress, downloading our papers, and submitting your highest quality manuscripts to us.

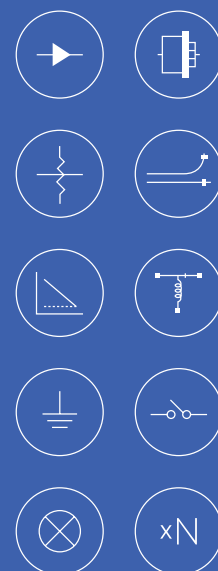


26 TO 86 GHZ

mmWave Components

400+ Models and Counting

- In-house design and manufacturing capability
- Industry-leading quality
- Supply chain security—no EOL target through the life of your system

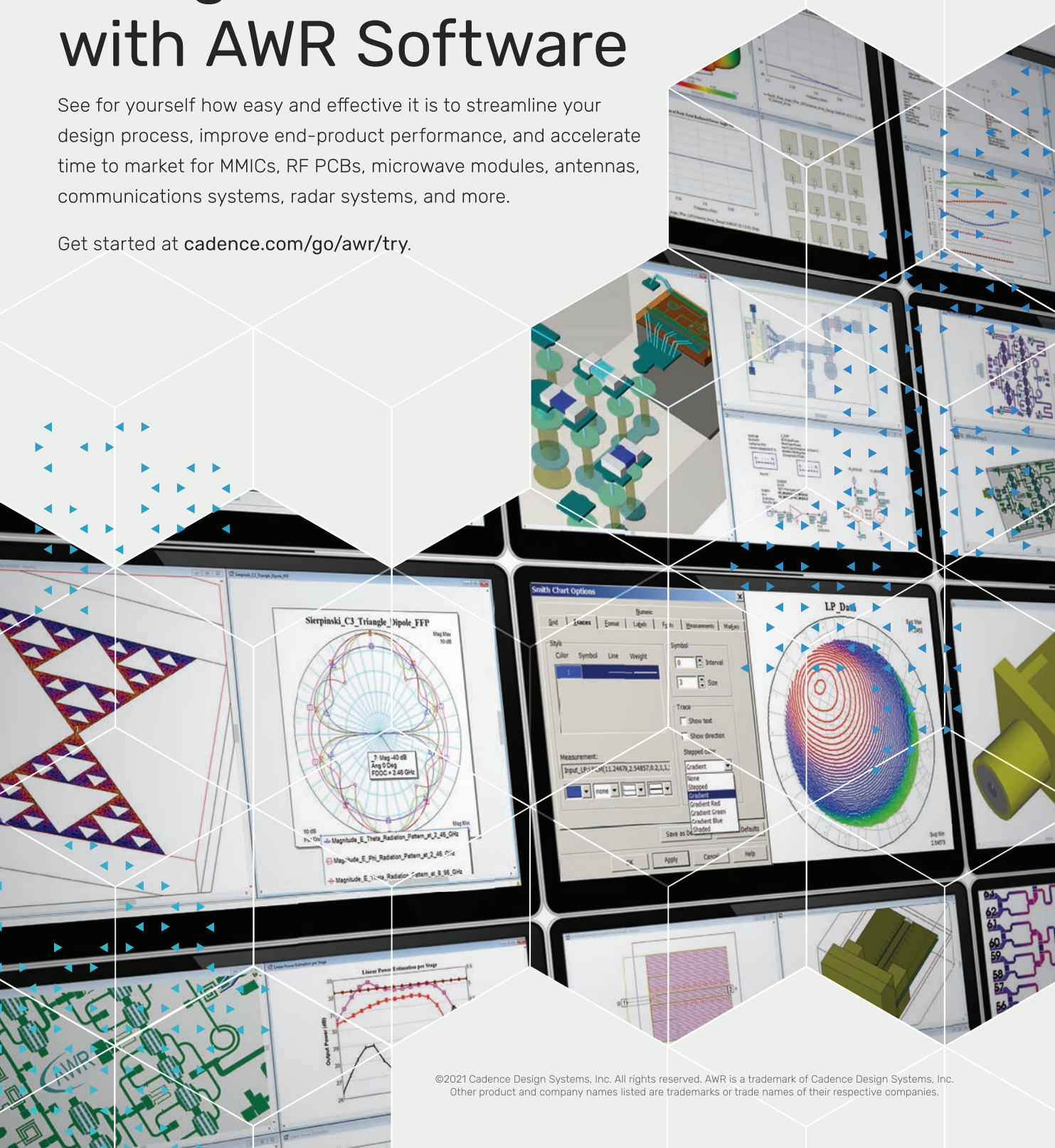




Design Smarter with AWR Software

See for yourself how easy and effective it is to streamline your design process, improve end-product performance, and accelerate time to market for MMICs, RF PCBs, microwave modules, antennas, communications systems, radar systems, and more.

Get started at cadence.com/go/awr/try.



Editor

Robert H. Caverly, Villanova University,
Pennsylvania, USA, microwave.editor@ieee.org

Assistant Editor

Sharri Shaw, JWM Consulting LLC, USA,
microedt@outlook.com

Associate Editors

Nuño Borges Carvalho, University of Aveiro,
Portugal, nbcarvalho@ua.pt

Simone Bastioli, RS Microwave, New Jersey,
USA, sbastioli@rsmicro.com

Chia-Chan Chang, National Chung-Cheng
University, Taiwan, ccchang@ee.ccu.edu.tw

Ali Darwish, American University in Cairo,
Egypt, ali@darwish.org

Christian Fager, Chalmers University of Technology,
Sweden, christian.fager@chalmers.se

Jianguo Ma, Guangdong University of
Technology, China, mjg@gdut.edu.cn

Alfy Riddle, Quanergy Systems, Inc., Sunnyvale,
California, USA, alfred.riddle@quanergy.com

Luca Roselli, University of Perugia, Italy,
urlofi@tin.it; luca.roselli@unipg.it

Kamal Samanta, Sony Europe, U.K.,
kmalsamanta@googlemail.com

Almudena Suarez, University of Cantabria,
Spain, almudena.suarez@unican.es

Anding Zhu, University College Dublin,
Ireland, anding.zhu@ucd.ie

Columns and Departments

MicroBusiness

Fred Schindler, Newtonville, Massachusetts,
USA, m.schindler@ieee.org

Health Matters

James C. Lin, University of Illinois-Chicago,
Chicago, Illinois, USA, lin@uic.edu

Microwave Surfing

Rajeev Bansal, University of Connecticut,
Storrs, Connecticut, USA, rajeev@engr.uconn.edu

Book Reviews

James Chu, Kennesaw State University, Marietta,
Georgia, USA, jameschu@bellsouth.net

Education Corner

Rashaunda Henderson, University of Texas
Dallas, Texas, USA, mh072000@utdallas.edu

Women in Microwaves

Wenquan Che, Nanjing University of Science
and Technology, China, yeeren_che@163.com

Membership News

Bela Szendrenyi, Advantest, San Jose, California,
USA, bela.szendrenyi@advantest.com

New Products

Ken Mays, The Boeing Company, Washington,
USA, microwave.newproducts@ieee.org

In Memoriam Contributions

Jerry Hausner, USA, j.hausner@ieee.org

Ombuds Officer

Edward C. Niehenke, Niehenke Consulting,
USA, e.niehenke@ieee.org

IEEE Periodicals Magazines Department

Mark Gallaher, Managing Editor

Geraldine Krolin-Taylor, Senior Managing Editor

Janet Dudar, Senior Art Director

Gail A. Schnitzer, Associate Art Director

Theresa L. Smith, Production Coordinator

Felicia Spagnoli, Advertising Production Manager

Peter M. Tuohy, Production Director

Kevin Lisankie, Editorial Services Director

Dawn Melley, Senior Director, Publishing Operations

Advertising Sales

Mark David, Director, Business Development—
Media & Advertising

+1 732 465 6473, fax +1 732 981 1855

Digital Object Identifier 10.1109/MMM.2020.3042043



IEEE prohibits discrimination, harassment, and
bullying. For more information, visit <http://www.ieee.org/web/aboutus/whatis/policies/p9-26.html>.



Volume 22 • Number 3 • March 2021 • ISSN 1527-3342

features

18 All-Digital RFID Readers

*An RFID Reader Implemented on an FPGA Chip
and/or Embedded Processor*

Arnaldo S. R. Oliveira, Nuno Borges Carvalho, João Santos,
Alirio Boaventura, Rui Fiel Cordeiro, André Prata,
and Daniel Costa Dinis

25 Making a Low-Cost Software-Defined UHF RFID Reader

*A Project for Electrical Engineers, Hobbyists,
Tinkerers, and Students*

Edward A. Keehr and Gregor Lasser

46 Software-Defined RFID Readers

*Wireless Reader Testbeds Exploiting
Software-Defined Radios for Enhancements
in UHF RFID Systems*

Georg Saxl, Lukas Görtschacher, Thomas Ussmueller,
and Jasmin Grosinger

57 Stocktaking Robots, Automatic Inventory, and 3D Product Maps

*The Smart Warehouse Enabled by UHF-RFID
Synthetic Aperture Localization Techniques*

Matthias Gareis, Andreas Parr, Johannes Trabert,
Tom Mehner, Martin Vossiek, and Christian Carlowitz



on the cover:

©SHUTTERSTOCK.COM/ANDREY SUSLOV

IEEE Microwave Theory and Techniques Society

The IEEE Microwave Theory and Techniques Society (MTT-S) is an organization, within the framework of the IEEE, of members with principal professional interests in the field of microwave theory and techniques. All Members of the IEEE are eligible for membership in the Society. Information about joining the IEEE or the Society is available on the web, <http://www.ieee.org/membership>.

MTT-S AdCom

The Society is managed by an Administrative Committee (AdCom) consisting of 21 elected members of the Society plus additional ex-officio members as provided in the MTT-S Constitution and Bylaws, which is available on the web, <http://www.mtt.org>.

Officers

President: Gregory Lyons
President-Elect: Rashaunda Henderson
Secretary: Joseph Bardin
Treasurer: Maurizio Bozzi

Elected Members

Scott Barker	Sherry Hess
Maurizio Bozzi	Sridhar Kanamaluru
Nuno Borges Carvalho	Dietmar Kissinger
Robert H. Caverly	Gregory Lyons
Goutam Chattopadhyay	Raafat Mansour
Wenquan Che	Daniel Pasquet
Terry Cisco	Ajay Poddar
Kamran Ghorbani	Jose Rayas-Sanchez
Xun Gong	Peter Siegel
Ramesh Gupta	Anding Zhu
Rashaunda Henderson	

Ex-Officio Members

Immediate Past Presidents:

Alaa Abunjaileh* (2020)
Dominique Schreurs* (2018–2019)
Dylan Williams* (2017)

Honorary Life Members*
(max. three votes):

Józef Modelski
John T. Barr IV
Tatsuo Itoh
Richard Sparks
Peter Staecker

MTT-S Publications

IEEE Trans. Microwave Theory & Techniques Editor:	Jianguo Ma*
IEEE Microwave & Wireless Components Letters Editor:	Thomas Zwick*
IEEE Microwave Magazine Editor:	Robert H. Caverly
IEEE Trans. Terahertz Science & Technology Editor:	Imran Mehdi*
IEEE Journal of Electromagnetics, RF, and Microwaves in Medicine and Biology Editor:	Yongxin Guo
IEEE Journal on Multiscale and Multiphysics Computational Techniques Editor:	Costas Sarris
IEEE Journal of Microwaves Editor:	Peter Siegel

*Indicates voting AdCom ex-officio member

IEEE Microwave Magazine (ISSN 1527-3342) (IEMMF) is published 12 times a year by the Institute of Electrical and Electronics Engineers, Inc. Headquarters: 3 Park Avenue, 17th Floor, New York, NY 10016-5997 USA. Responsibility for the contents rests upon the authors and not upon the IEEE, the Society, or its members. IEEE Service Center (for orders, subscriptions, address changes): 445 Hoes Lane, Piscataway, NJ 08854. Telephone: +1 732 981 0060, +1 800 678 4333. Individual copies: IEEE members US\$20.00 (first copy only), nonmembers US\$37.00 per copy. Subscription rates: Subscriptions for Society members are included with membership dues. Nonmember subscription rates available upon request. Copyright and reprint permissions: Abstracting is permitted with credit to the source. Libraries are permitted to photocopy beyond the limits of U.S. Copyright law for the private use of patrons those articles that carry a code at the bottom of the first page, provided the per-copy fee is paid through the Copyright Clearance Center, 222 Rosewood Drive, Danvers, MA 01923 USA. For other copying, reprint, or republication permission, write Copyrights and Permissions Department, IEEE Service Center, 445 Hoes Lane, Piscataway, NJ 08854 USA. Copyright © 2021 by the Institute of Electrical and Electronics Engineers, Inc. All rights reserved. Periodicals postage paid at New York, N.Y., and at additional mailing offices. Ride along enclosed. Postmaster: Send address changes to *IEEE Microwave Magazine*, IEEE Operations Center, 445 Hoes Lane, Piscataway, NJ 08854 USA. Canadian GST #125634188
PRINTED IN THE USA

Digital Object Identifier 10.1109/MMM.2020.3042044

columns & departments

5 From the Editor's Desk

■ Robert H. Caverly

Welcome to the March 2021 Issue!

6 President's Column

■ Gregory Lyons

Introducing New AdCom Members

10 MicroBusiness

■ Fred Schindler

Success and Failure Part 1:

In Celebration of Failure

12 Microwave Bytes

■ Steve C. Cripps

Coupling Factors

16 From the Guest Editors' Desk

■ Thomas Ussmueller and Christian Carlowitz

Advancing Ultrahigh-Frequency RFID Through Digital Signal Processing

69 Book/Software Reviews

■ James Chu

A Must-Have Reference on Antenna Technology

71 Health Matters

■ James C. Lin

Sonic Health Attacks by Pulsed Microwaves in Havana Revisited

74 In Memoriam

George Matthaei

76 MTT-S Society News

■ Chinmoy Saha

Inauguration of the GECBH Student Branch Chapter and L4 Talk Series

82 New Products

■ Ken Mays, Editor

86 Enigmas, etc.

■ Takashi Ohira

Sinusoidal Wave Output

88 Conference Calendar



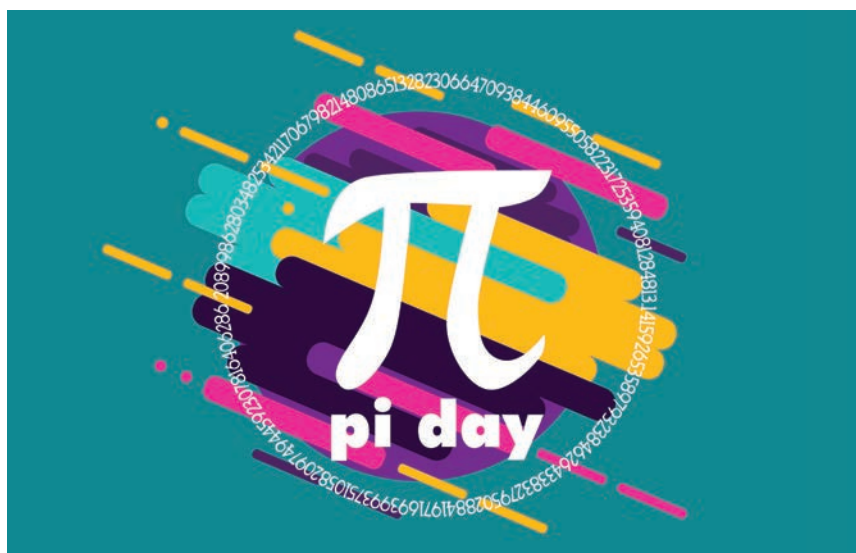
From the Editor's Desk

Welcome to the March 2021 Issue!

■ Robert H. Caverly

Even though the issue date says March 2021, I am writing this welcome on a cold, blustery day in early December. Numerous conferences are scheduled between this writing and when you receive the issue: the IEEE International Microwave Bio-medical Conference, IEEE Radio and Wireless Week, and European Microwave Conference, to name just a few. I hope that you took advantage of those conferences to keep yourself up to date on the latest developments in the microwave and wireless field.

Another way to keep current with technical developments or learn about a new technology is with *IEEE Microwave Magazine*; this month, thanks to the efforts of Prof. Thomas Ussmuel-ler and Prof. Christian Carlowitz, we have an issue focused on digital signal processors for RFID. This focus issue is a joint effort by two IEEE Microwave Theory and Techniques Society (MTT-S) technical committees (TCs): MTT-15, the RF/Mixed-Signal Integrated Circuits



and Signal Processing TC, and MTT-26, the RFID, Wireless Sensor, and IoT TC.

The issue includes four technical articles by authors from both industry and academia that provide an in-depth look at signal processing as applied to RFID in applications such as object identification as well as other types of identification. An excellent introduction to the issue can be found in the "From the Guest Editors' Desk" column, and I suggest that this column be

your first stop, to read summaries of the focus issue articles.

These articles came out of a conference workshop on the topic, which is an excellent way to develop a focus issue as the leaders in the topic area are already identified and the material is organized. If you have organized a workshop for the IEEE MTT-S International Microwave Symposium or any other conference, I encourage you to consider

(continued on page 75)

Robert H. Caverly (rcaverly@villanova.edu) is with Villanova University, Villanova, Pennsylvania, USA.

Digital Object Identifier 10.1109/MMM.2020.3043648
Date of current version: 3 February 2021



President's Column

Introducing New AdCom Members

■ Gregory Lyons

Each year, the IEEE Microwave Theory and Techniques Society (MTT-S) elects seven voting members to our Administrative Committee (AdCom) for a three-year term. This month, it is my pleasure to introduce you to four new AdCom members who were elected to a 2021–2023 term during our Fall 2020 AdCom elections. They are Sridhar Kanamaluru, who served as the 2020 AdCom secretary; Kamran Ghorbani, a previous AdCom member; Robert Caverly, editor-in-chief of *IEEE Microwave Magazine*; and Xun Gong, an active MTT-S volunteer. In addition, I am pleased to introduce the 2021 AdCom secretary, Joseph (Joe) Bardin, another dedicated MTT-S volunteer.

Each new AdCom member has provided a brief biography and a statement of his perspectives on the MTT-S, representing a snapshot of where the Society is likely heading in the near future. It is the job of the AdCom to keep the MTT-S healthy and move the Society in new directions for the benefit of our membership, the microwave engineering profession, and humanity. The complete AdCom orga-



©SHUTTERSTOCK.COM/DICKGAGE

nization can be found at www.mtt.org/administrative-committee-officers.

The MTT-S is a very active IEEE Society. If you would like to get involved as a volunteer, fill out the contact form at www.mtt.org/connectme, and we will make sure you get connected.

New AdCom Members

Sridhar Kanamaluru

Sridhar Kanamaluru is the chief architect for aerospace instrumentation at Curtiss-Wright, serving the U.S. Department of Defense flight test instrumentation industry. He received his B.S. degree from Anna University, Chennai, India, in 1987 and his M.S. and Ph.D. degrees from Texas A&M

University, College Station, in 1993 and 1996, respectively. Since then, he has served in increasingly senior roles in the microwave industry, including as senior antenna engineer (Millitech), manager of microwave systems (Sarnoff), director of engineering (Herley), and principal scientist (DRS Technologies). He has also been an adjunct professor at the New Jersey Institute of Technology and Villanova University. He has served the MTT-S in various capacities, including a member of Technical Committee MTT-8, a member

multiple times on the Technical Program Review Committee of the IEEE MTT-S International Microwave Symposium (IMS), IMS2018 general chair, and MTT-S 2020 AdCom secretary.

AdCom Member Perspectives

My experience with the Society's activities, as IMS general chair and AdCom



Gregory Lyons (glyons@ieee.org), 2021 MTT-S president, is with Lincoln Laboratory, Massachusetts Institute of Technology, Lexington, Massachusetts, USA.

Digital Object Identifier 10.1109/MMM.2020.3042028
Date of current version: 3 February 2021



DC TO 67 GHz

Cables and Adapters

System Interconnect and Precision Test

- 375+ models in stock
- Custom assemblies available on request
- Rugged design and construction

Precision Test Cables

- Options for every environment: armored, phase stable, temperature stable, ultra-flexible, and more.

Interconnect Cables

- Wide selection of connector options from SMA to 2.4mm
- 0.141, 0.086 and 0.047" center diameter

VNA Cables

- Crush and torque resistant
- Competitive pricing, starting at \$1,795 ea.

Adapters:

SMA, BNC, N-Type, 3.5mm, 2.92mm, 2.92mm-NMD, 2.4mm, 2.4mm-NMD, 1.8mm



Sridhar Kanamalur.

secretary, has shaped my objectives for how to serve the Society. The IMS is the single greatest Society asset to reach our worldwide members and industry partners and to share and exchange information interactively. To address new realities related to face-to-face and virtual meetings, I strongly advocate that future IMS meetings provide recordings of all workshops and technical sessions, even when in-person gatherings are possible. The recorded sessions, hosted in the MTT-S Resource Center, would enable industry practitioners to access materials at their convenience, thereby increasing the Society's value. In addition, because future technical advancements will require a multidisciplinary skillset, I plan to engage with sister Societies that strongly overlap with the MTT-S field of interest, such as the IEEE Aerospace and Electronic Systems Society, the IEEE Communications Society, and the Association of Old Crows, to provide multidisciplinary "system" workshops at conferences and Chapter meetings to benefit industry practitioners and increase new member recruitment.

Kamran Ghorbani

Kamran Ghorbani received his B.Eng. degree (with honors) and his Ph.D. degree from RMIT University, Melbourne, Australia, in 1994 and 2001, respectively. From 1994 to 1996, he was a graduate RF engineer with AWA Defense Industries, working on early warning radar systems.

In June 1996, he joined RMIT to pursue his Ph.D. studies. From 1999 to 2001, he was a senior RF engineer with Tele-IP, working on very-high-frequency transceivers for commercial aircraft. He joined the Department of Communication and Electronic Engineering (now the School of Engineering) at RMIT University in 2001 as a continuing academic. Prof. Ghorbani is currently the director of the Communication Technologies Research Center, RMIT University. He is responsible for strategic planning and management. His research interests include multifunctional structure, radar systems, ferroelectric materials, metamaterials, RF energy harvesting, and composite materials for RF applications.

AdCom Member Perspectives

I see four areas of focus for the MTT-S:

- 1) *Bridge academia and industry:* Increase membership and involvement from industry, initiate large and small industry projects, and involve industry in more technical committees/activities and conference organization. Enhance the career platform session at both large and small conferences, where industry can meet academics and young professionals.
- 2) *Promote diversity:* Increase activities and committee participation with Young Professionals and Women in Engineering. Provide funding packages such as dedicated scholarships and travel allowances for developing countries
- 3) *Membership development:* Enhance member activities at smaller conferences, including student competitions,



Kamran Ghorbani.

conference travel allowances, and industry workshops. Create new student travel grants, expand fellowships, and expand webinar topics. Create attractive membership packages.

- 4) *Global vision:* Expand and enhance the collaboration between the MTT-S, European Microwave Association, Asia-Pacific Microwave Conference, and sister Societies.

Robert H. Caverly

Robert H. Caverly received his B.S. and M.S. degrees in electrical engineering in 1976 and 1978, respectively, from North Carolina State University, Raleigh. He received his Ph.D. degree from Johns Hopkins University, Baltimore, Maryland, in 1983. His first academic position, in 1983, was in the Department of Electrical and Computer Engineering, South-eastern Massachusetts University, which later became the University of Massachusetts-Dartmouth. In 1997, he joined Villanova University, Pennsylvania, where he is currently a professor in the Department of Electrical and Computer Engineering. He has published more than 100 journal and conference papers and is the author of the books *Microwave and RF Semiconductor Control Device Modeling* (2016) and *CMOS RFIC Design Principles* (2007). In 2014, he was appointed an MTT-S Distinguished Microwave Lecturer (DML), with the talk "RF Aspects of Magnetic Resonance Imaging," and he is currently an Emeritus MTT-S DML. An IEEE Life Fellow, Prof. Caverly is the editor-in-chief of *IEEE Microwave Magazine*.



Robert H. Caverly.

AdCom Member Perspectives

As editor-in-chief of *IEEE Microwave Magazine*, as well as during my tenure as a DML, I have personally seen the vibrant technical expertise that is the hallmark of the MTT-S as the “Megahertz to Terahertz Community.” Transmitting this vibrancy to current and next-generation microwave engineers is crucial if the MTT-S is to continue to be the leader of the microwave/RF community. Our mission will require a deep commitment to reach out to all fields that fall within our MHz to THz Community. Expanding our influence includes welcoming technical areas that might be considered outside traditional microwaves but still within our field of interest. It also includes educational outreach beyond just academia, working with our Young Professionals to welcome them to the field and increasing support to further stimulate interest in microwaves through Women in Microwaves and other outreach activities among a globally diverse audience, especially in Regions 9 and 10 and in Africa.

Xun Gong

Xun Gong received his B.S. and M.S. degrees in electrical engineering from Fudan University, Shanghai, China, in 1997 and 2000, respectively, and his Ph.D. degree in electrical engineering from the University of Michigan, Ann Arbor, in 2005. He is currently the Lockheed Martin Professor of Electrical and Computer Engineering at the University of Central Florida, Orlando, and director of the Antenna, RF, and Microwave Integrated Systems Labo-



Xun Gong.

ratory. His research interests include microwave passive components and filters, sensors, antennas and arrays, flexible electronics, and packaging. He has more than 130 publications and holds four patents in his field. He served as associate editor of *IEEE Transactions on Microwave Theory and Techniques* and *IEEE Microwave and Wireless Components Letters*. He is currently the MTT-S Region 3 Chapter coordinator.

AdCom Member Perspectives

My journey in the MTT-S began during IMS2002, in Seattle, Washington, as a Ph.D. student. Since then, I have engaged in various MTT-S activities through conference presentations, local Chapters, conference organization, editorial boards, associate editorships, technical coordinating committees, and regional coordinators. I benefited from what the MTT-S generously offered, and I would like to contribute to the MTT-S in return, particularly through promoting microwave education among students and membership development through Chapters. Efforts in developing global MTT-S-related educational materials are critical for the microwave community and for attracting students to study microwaves. I believe that effectively connecting MTT-S members in academia, industry, and government is the key factor to promoting education, employment, and conferences and can assist microwave practitioners with continued education.

Joseph Bardin

Joseph Bardin is a full professor of electrical and computer engineering at the University of Massachusetts–Amherst and a research scientist with Google Quantum AI. His research interests include the design and use of integrated circuit technologies for scientific applications, such as quantum computing and radio astronomy. In addition to his MTT-S AdCom appointment, Prof. Bardin serves as a Steering Committee member and associate editor of *IEEE Transactions on Quantum Engineering*, a track editor for *IEEE Journal of Microwaves*, and a member of the MTT-S Working Group on Quantum Computing as well as Technical Com-



Joseph Bardin.

mittees MTT-4 and MTT-11. He is the recipient of a 2011 DARPA Young Faculty Award, a 2014 National Science Foundation CAREER Award, a 2015 Office of Naval Research Young Investigator Program Award, a 2016 University of Massachusetts College of Engineering Outstanding Junior Faculty Award, a 2016 University of Massachusetts Convocation Award for Excellence in Research and Creative Activity, and a 2020 MTT-S Outstanding Young Engineer Award.

AdCom Member Perspectives

Throughout my academic and professional career, the MTT-S has been my go-to technical community, and I am enthusiastic to have the opportunity to contribute to this great Society through AdCom service. Historically, MTT-S members have been responsible for critical technological developments in the communications, aerospace, health-care, and security industries, and, in the coming decades, we can expect that new applications of microwave technologies will drive the development of markets that critically rely on MTT-S engineers. In fact, we are already seeing this with the rapid growth in the field of quantum computing. To support future needs, it is essential that the MTT-S inspire and educate a new generation of microwave engineers. Moreover, to build the best possible MTT-S of tomorrow, it is critical that we seek to structure our activities to maximize diversity, equity, and inclusion within today’s Society.





MicroBusiness

Success and Failure Part 1: In Celebration of Failure

■ Fred Schindler

I've only ever failed one class. It was a required course in my major, as an undergraduate. The failure was educational. Up to that point, I had been happy to go through the mechanics of solving problems, without really grasping the underlying rationale. As a result, I didn't always understand how to approach solutions. Needless to say, when I took the course again, I made sure I understood how and why to solve each problem. But much more important is that I had become a better student, which impacted every future course I took. If I hadn't failed that class, I might have continued to muddle through and would likely have been a less successful engineer.

Failure is all around us, and it can be a good thing. It is an opportunity to improve, though improvement is not guaranteed. Failure is a signal, and it's how we respond to it that determines whether we continue to fall short or pivot to success.

Roughly 40 years ago, a new variant of the GaAs MESFET was developed: the high-electron mobility transistor, or



HEMT. Clever bandgap engineering with aluminum GaAs and GaAs layers was used to coax carriers from one semiconductor layer to another. The result was much higher carrier mobility and greater transistor gain. In short order, superior low-noise amplifiers were demonstrated. A few years later, pseudomorphic HEMTs, or pHEMTs, were developed, extending the concept with some InGaAs.

I was working in a research lab when the first pHEMT results were published. We initiated a project to develop a better power transistor

based on the pHEMT approach. Most of the published pHEMT work focused on the gain and the noise figure. There was very little in the literature about power performance. It looked like a straightforward project. We would increase the doping to boost the saturated current and optimize the gate recess for the breakdown voltage. The first devices initially looked great: they had a high current and an adequate breakdown voltage.

But the microwave test results were disappointing. While the small-signal gain was excellent, the saturated power

Fred Schindler (m.schindler@ieee.org)
consults on management issues in the Boston,
Massachusetts, area.

Digital Object Identifier 10.1109/MMM.2020.3042031
Date of current version: 3 February 2021

was abysmal. We had found that RF performance was dramatically different than dc performance. The current-voltage curves of the transistor, measured at very low frequencies, were excellent. When we measured them with high-speed pulses, the current collapsed, with a significant dependence on the quiescent bias point. What followed was months of investigating why the current collapsed and optimizing the transistor design and fabrication process to reduce the effect. Ultimately, we were able to demonstrate excellent power transistor performance [1], [2]. Failure and disappointment had been turned into success and opportunity.

I had another successful failure early in my career while working at the same research lab. We decided to submit a proposal for an active filter project. As with most proposals, we had very little time. I was the technical lead; I came up with the approach and verified it with simulations. I made heavy use of the simulator's optimizer function and was satisfied with how the performance improved. We submitted the proposal and, a few weeks later, received a letter from the funding agency's technical lead. He was intrigued by our approach and duplicated our simulation. In doing so, he noticed that the filter, although effective, was not operating as we claimed. He was right. After

the optimizer was finished, I had not closely examined the circuit and how it functioned.

I then took some time to understand the optimized circuit and performed additional analysis. It wasn't what we had originally claimed, but it was interesting and useful. We met with the funding agency, and, after apologizing, I explained my follow-up analysis and the potential for the circuit approach. In the end, our work was funded, and we successfully demonstrated the technique [3]. Once again, we were able to turn failure into success. But there was greater value in what I learned about not letting an optimizer loose without understanding what it did. I also learned to be much more rigorous in my work.

Failure can be a useful thing but only if we learn from it. Take, for example, corporate acquisitions. There are companies, including some very successful technology businesses, that have been built on acquisitions. There are others that make acquisitions time and again, only to have the acquired companies disappear and never heard from again. I'm sure that, in the first case, for the successful company built on acquisitions, there have been failures. These must have been failures they learned from, so they could build a methodology for successful acquisition and continuous improvement. In the second case, where acquisitions

perpetually fail, the company never seems to learn. It's a double failure, first to do something poorly and then not to learn from it.

Let's celebrate failure, but not all failures. It's not that we want to fail—we don't design our projects for failure. But we shouldn't manage our work to avoid failure either. If our goal is to avoid failure, we may also avoid innovation. Let's not try to fail but understand that, to make progress, there is a real possibility of failure. Failure that is learned from can lead to future success.

Thinking back to that class I failed as an undergraduate, I wish I hadn't, even if it was a valuable failure. It would have been better to have failed a class much earlier in my educational career. There was a lesson I needed to learn, and the sooner I had, the better off I would have been.

References

- [1] J. C. Huang et al., "An AlGaAs/InGaAs pseudomorphic high electron mobility transistor (PHEMT) for X- and Ku-band power applications," in *Proc. 1991 IEEE MTT-S Int. Microw. Symp. Dig.*, Boston, MA, vol. 2, pp. 713–716. doi: 10.1109/MWSYM.1991.147103.
- [2] S. Shanfield et al., "A high linearity, high efficiency pseudomorphic HEMT," in *GaAs IC Symp. Tech. Dig. 1992*, Miami Beach, FL, pp. 207–210. doi: 10.1109/GAAS.1992.247189.
- [3] M. J. Schindler and Y. Tajima, "A novel MMIC active filter with lumped and transversal elements," *IEEE Trans. Microw. Theory Techn.*, vol. 37, no. 12, pp. 2148–2153, Dec. 1989. doi: 10.1109/22.44134.





Microwave Bytes

Coupling Factors

■ Steve C. Cripps

Some years ago in this column, I mused on the rather point-less challenge of summarizing my technical career in two words and came up with “Chasing Chebychev,” thus triggering an article about matching techniques [1]. I have, of late, been thinking along somewhat similar lines about what particular device, entity, gizmo I would nominate as playing some kind of a continuous role over my active decades in the microwave business, something that just keeps on appearing around corners. I think there is a clear winner on this one, and it’s the 3-dB quadrature coupler. This is, of course, in part closely coupled (er ... sorry ...) to a lengthy association with the balanced amplifier; more of that shortly, but maybe rather than launching into war stories about my lifelong battle of persuading fabricators that it is indeed possible to make 10 micron gaps (hope you’re listening, Ed), maybe I should “begin at the beginning.”

Steve C. Cripps (crippssc@cardiff.ac.uk) is with the School of Engineering, Cardiff University, United Kingdom.

Digital Object Identifier 10.1109/MMM.2020.3042578
Date of current version: 3 February 2021



Figure 1 shows, in schematic form, the essence of what we mean by a quadrature coupler. It is a matched four-port passive structure that has the well-known properties as shown in the figure; essentially, the input power at port 1

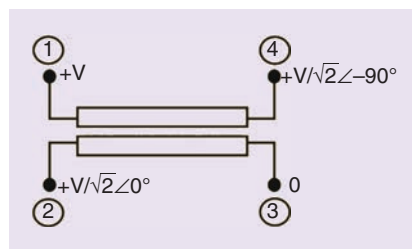


Figure 1. A quadrature coupler in its schematic form.

divides between ports 2 and 4, with no power coupled to port 3; the coupled outputs display a 90° phase difference. What is interesting about this configuration, and admittedly rarely commented upon in standard textbooks which launch straight into some formal analysis, is that the quadrature phase property is a direct result of the symmetry of the structure; it displays what I will term “port rotation symmetry.” By this I mean that the coupling pattern remains the same regardless of which port is used as the input. So, for example, if we select port 2 as the signal input, the power will divide between ports 1 and 3 with port 4 now “isolated.”

Taking a more general case, an input signal of magnitude $V \cos \omega t$ splits into two outputs, $\alpha V \cos \omega t$ at port 2 and $\gamma V \cos(\omega t + \phi)$ at port 4. We now apply a second input, also $V \cos \omega t$, at the “isolated” port 3, which results in additional components $\alpha V \cos(\omega t)$ at port 4 and $\gamma V \cos(\omega t + \phi)$ at port 2, the phase split ϕ at this point being “unknown.” So the combined voltages at the output ports are

Port 2: $\alpha V \cos(\omega t) + \gamma V \cos(\omega t + \phi)$

Port 4: $\gamma V \cos(\omega t) + \alpha V \cos(\omega t + \phi)$.

The normalized power at the output ports, for those who can remember the cosine rule, are

$$\text{Port 1: } V^2(\alpha^2 + \gamma^2 - 2\alpha V \cos \phi)$$

$$\text{Port 4: } V^2(\alpha^2 + \gamma^2 - 2\gamma V \cos \phi),$$

which must add up to the combined normalized input power, $2 V^2$. This can clearly only be true if $\alpha^2 + \gamma^2 = 1$, which we knew at the outset, but also $\cos(\phi) = 0$, hence $\phi = 90^\circ$.

Interesting. Throughout my long association with this device, I have always pondered why or how the quadrature relation is maintained, essentially over an infinite bandwidth, and have heard a number of “intuitive” explanations. I myself gave a somewhat a more lengthy derivation in an early “Microwave Bytes” column [2]. I first encountered this rather more elegant and fundamental symmetry derivation early one morning at an MTT Symposium (as it was then called) breakfast table from Ralph Levy, scribbled out on a table napkin. It does remain, of course, to show that this structure can achieve the port 4 cancellation property. There is also what is a slightly stickier issue regarding the absolute values of phase transmission, as opposed to their difference. Couplers have electrical length, which strictly should be added on to the differential phases shown in Figure 1; in fact, the phases I show assume that this length is equal to a quarter wavelength, which a full analysis shows to be a very reasonable, albeit slightly approximate, value.

I will refrain from now repeating in detail what is very well documented material that analyzes this structure by superimposing two configurations, shown in Figure 2. The original configuration can be considered to be the superposition of an “even mode” and “odd mode” excitation of the structure. Whilst very elegant, the details of a full generalized analysis are surprisingly complicated, but the main outcome is that more or less everything we want falls nicely into place by making the odd and even mode impedances, Z_{oe} and Z_{oo} , follow the relationship $Z_{oo}Z_{oe}$

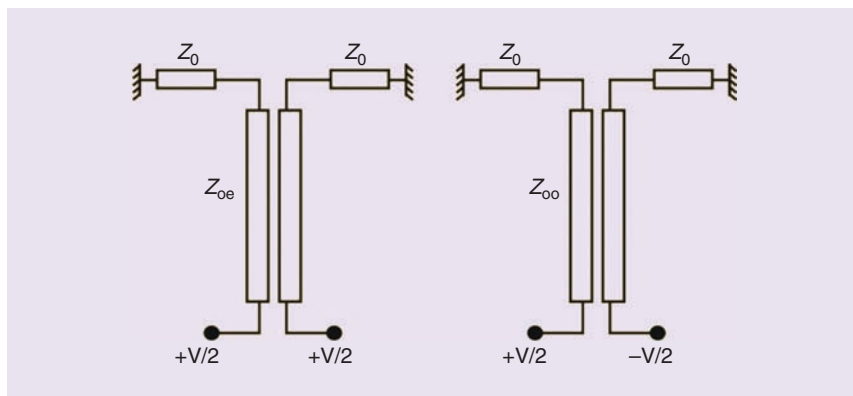


Figure 2. Even and odd mode coupler analysis.

$= Z_0^2$, along with the constraint that the propagation velocities associated with even and odd modes are equal. This delivers the matched port and isolated port requirements, and the individual values of Z_{oe} or Z_{oo} define the all-important coupling factor α . That said, I have from time to time found myself searching the archives for a reference that actually tackles the general analysis, in particular, nailing down the aforementioned absolute phase transmissions to the direct and coupled ports. My favorite for this reference, amongst numerous candidates [3], sits in my “archive” file box and dates back to the pre-plain paper copier days but does derive the full four-port s-matrix for the most general case of a coupled line pair.

Anyway, the fun now starts as we use the theory to design a 3-dB coupler. Ever since Kurokawa proposed the balanced amplifier [4], the 3-dB “hybrid,” as it is somewhat curiously known, became an item of much focus for broadband amplifier designers. Indeed, I remember a time when it seemed the lifetime goal of every designer was to invent a new type of 3-dB coupler. Essentially, to achieve the 3-dB coupling, the odd mode impedance has to be somewhere around 20 ohms, which, due to a floating rogue factor of 2, means that in the odd

mode excitation shown in Figure 2 the structure behaves as a balanced 40-ohm line. This is virtually impossible to achieve using a single pair of edge-coupled microstrip lines, for any remotely realizable gap dimension; and for broader bandwidths, taking in octave and even approaching double octave, this impedance needs to be even lower. Thereby hangs a long ledger of patents and ongoing newer attempts to be found in almost every issue of our *IEEE Microwave and Wireless Components Letters*. It is worth noting, in passing, that there is an “old way” around this prob-

lem, which was at one time quite widely used and is shown in Figure 3. Before the “Lange revolution,” the limitations of thin-film processing did just about allow couplers of around a 6-dB coupling factor to be made using single-coupled planar microstrip lines. As such, a “tandem” arrangement using

The layout is made considerably more convenient if the direct and isolated port connections are “crossed.”

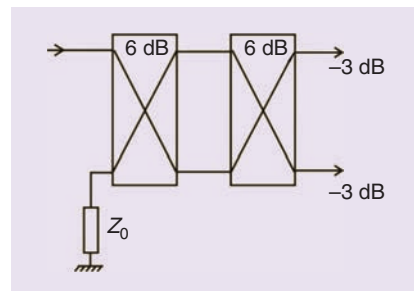


Figure 3. A “tandem” coupler configuration.

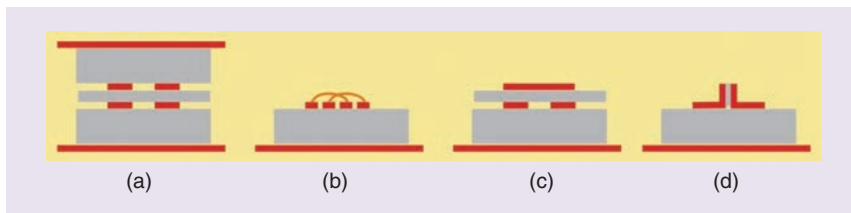


Figure 4. Enhanced coupling structures: (a) broadside, (b) interdigital ("Lange"), (c) strip overlay, and (d) vertical overlay.

a pair of 6-dB couplers was able to deliver the same response as the unrealizable 3-dB item. Note that the layout, not to mention drawing the diagram, is made considerably more convenient if the direct and isolated port connections are "crossed"; this is usually the case with most implemented couplers, so that the two outputs appear on the same side of the structure. This took up even more space (couplers are always space hungry) and had more loss than a single coupling structure, but is perhaps one of those rare items of "old ways" that may conceivably be of some use in a modern context.

But, essentially, the challenge is to find a way of increasing the coupling between the two lines, and Figure 4 illustrates several ways of doing this. Probably the most familiar solution, and the basis for most commercial connectorized components, is the multilayer "broadside" structure shown in Figure 4(a). The use of a thin central dielectric enables the odd mode impedance to be made suitably low, while much thicker outer dielectric spacings implement the much higher even mode impedance. But this structure is inconvenient for direct integration into the planar microstrip microwave environment that is universal practice in active gigahertz components and sub-assemblies. The major breakthrough was the interdigital coupler, originally

published by Lange [5], whereby the effective coupling length was multiplied up by splitting the two microstrip lines into strips and "mixing them up" [Figure 4(b)]. This enabled much tighter coupling factors to be achieved using a planar structure, although the requirements on the fabrication tolerances, along with some quite challenging bondwire placements, created a constant, if not widely admitted, headache for fabrication facilities. I well remember that the accepted formula for a 3:1 bandwidth coupler required gaps of little more than 10 microns, which required some special processing techniques, not to mention post-processing hours spent fusing out metal bridges across the tiny gaps. In fact, such tolerances are no big deal at all in semiconductor fabrication, a dichotomy that I never fully fathomed out. The standard excuse was the superior surface finish on a semiconductor wafer: if alumina was polished, the metal ceased to stick, I recall being told at the time.

Two more strategies, shown in Figure 4(c) and (d), seem to have had little attention outside of the patent office: both would appear to be useful for discrete PC board layouts; maybe they have been eclipsed by the more recent availability of surface-mount "drop-in" couplers for telecom bands. A simple inverted microstrip overlay on the basic coupled microstrip lines [Figure 4(c)] works well and can show improved directivity in comparison to planar configurations, where the velocity ratios of even and odd

modes diverge due to the differing air and board dielectrics. This is also an issue in the simple structure shown in Figure 4(d), which would appear to be quite easy to implement on a circuit board and a good deal cheaper than buying drop-in couplers. I should note that, in the case of Figure 4(c), I am not including the case of a simple dielectric overlay, which can improve directivity but has only a small effect on coupling.

The beneficial properties of a balanced amplifier (Figure 5) are possibly less frequently touted these days, for a number of reasons. It was always primarily aimed at broadband applications, where the device input (especially) and output are difficult to match over the wide bandwidth, and in any case some form of mismatch is required in order to result in a flat gain response. The couplers cancel

the reflections from the mismatched devices, and this results in nicely cascadable gain "modules" that gave the manufacturing and sales operations more flexibility on the range of products that could be "cobbled" together

with minimal development time. As such, we never really had to tackle the problems of designing interstage matching networks. When in the early 2000s I emerged from the broadband military amplifier scene and stumbled into the burgeoning telecom sector, I was surprised to find almost no balanced amplifier designs anywhere. "Never saw the point of it," a rather younger designer ("RYD") than I asserted: "Why do your interstage matching through 50 ohms? Plus you need twice the component count and twice the board space." Well, of course, the bandwidth requirements were pretty narrow by comparison, but as I got involved in solving things like stability problems, out-of-band gain, not to mention memory effects (really!), I could not help feeling a bit nostalgic for some balanced stages.

The major breakthrough was the interdigital coupler.

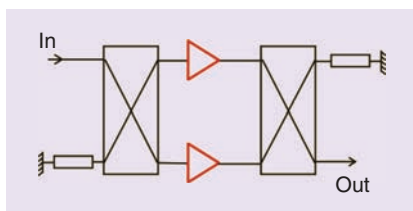


Figure 5. A balanced amplifier.

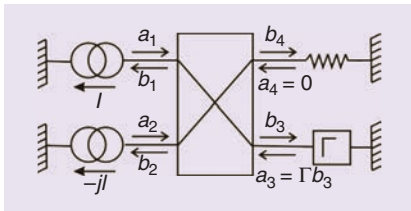


Figure 6. Analysis of a balanced amplifier with mismatched output termination.

Even in the broadband sector, the traditional cascaded-balanced approach went into a decline, mainly due to the availability of broadband MMICs, usually based on distributed circuit topologies, that could span multi-octave bandwidths. But recently I have been involved in, perhaps I could even say I initiated, something of a “balanced renaissance” when I discovered, somewhat by accident, a remarkable property of the balanced configuration that we all appeared to miss in its heyday. Basically, if the output isolated port termination is replaced by a current source, which is coupled from the input signal, the load presented to the balanced devices can be “modulated” over a substantial range. As such, the “load modulated balanced amplifier,” or LMBA, has received quite a lot of attention in the literature over the last couple of years [6]. I will be addressing this topic in due course in this column, but for the present I will highlight something that has emerged during this recent revisit of the balanced amplifier.

It turns out that the balanced amplifier *does* have an Achilles heel, and looking into this problem more recently I have explained some of the effects that were ever-present irritations when trying to ship high-gain broadband amplifiers with several cascaded balanced modules. In a nutshell, a mismatched load on the output coupler can cause some serious skewing of the load presented to the balanced devices. The situation is summarized for analysis in Figure 6; the output coupler has its isolated port terminated with a “perfect” on-board load, but the output termination has an “imperfect” voltage standing

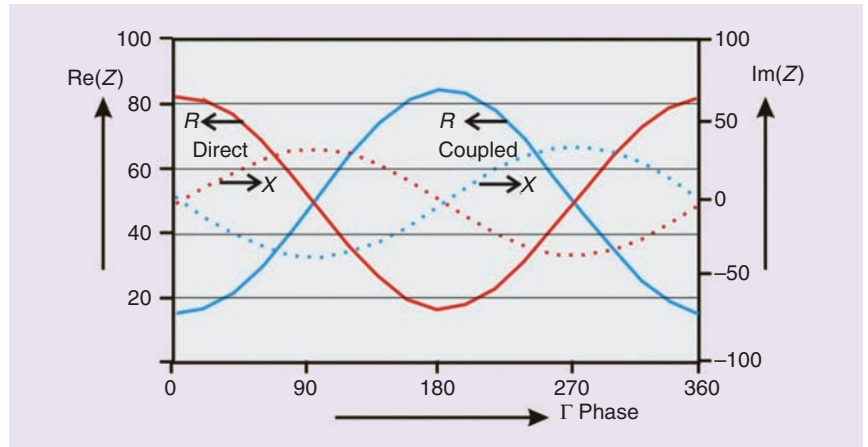


Figure 7. Mismatch at the balanced device planes, 2:1 VSWR termination.

wave ratio (VSWR), having a reflection coefficient Γ with any phase over the operating bandwidth. The two transistors are represented by current sinks having equal amplitudes and appropriate 90° phasing. So we can apply the four-port s-parameter matrix to relate the forward and reverse voltage waves at each port.

At this stage of my life, I don’t greatly savour the algebraic task and defer to the admirable equation solver in Mathematica; the results of interest, which are the device plane reflection coefficients, are somewhat complicated but simplify for the 3-dB balanced case where $\alpha = \gamma = 1/\sqrt{2}$:

$$\rho_1 = \frac{b_1}{a_1} = \frac{\Gamma}{\Gamma + 1},$$

$$\rho_2 = \frac{b_2}{a_2} = \frac{\Gamma}{\Gamma - 1},$$

the bold fonts now instigated to remind us that these are complex variables that are being swept over a full range of phase angles.

Depending on how good your recollections of complex variable geometry are, it may (or may not!) be clear that if Γ traces a circle on the Smith chart, centered on the origin, the ρ trajectories also map out a circle. For very small deviations of Γ from zero, the two device impedances remain approximately

equal and track Γ itself. But, although the two ρ trajectories each map the same circle, the corresponding points at the same Γ phase are diametrically opposite, as indicated in the corresponding impedance plots shown

in Figure 7. This was quite a shock to me, as a nearly life-long protagonist of the balanced amplifier, especially for a PA application where the resistive load at each device essentially defines the saturated power. RYD

would, no doubt, savor this result; the “magic” of a balanced amplifier does not extend to isolation from the output termination and, as such, does not replicate the function of an output isolator. However, the proximity of the circles to the Γ circle shows that the impact would be very similar for an equivalent single-ended design; in fact, the diametric opposition of the reflection coefficients at the two balanced ports gives some significant mitigation inasmuch as the “worst case” of mismatch would occur only on one side at a time.

I have to admit, this for me is a relatively recent discovery, as measured on a timescale based on decade units. Back in the era of shipping production quantities of broadband amplifiers for military ECM systems, much valuable

(continued on page 87)



From the Guest Editors' Desk

Advancing Ultrahigh-Frequency RFID Through Digital Signal Processing

■ Thomas Ussmueller and Christian Carlowitz

Digital signal processing (DSP) is a key technology for a vast number of different applications, including RF functions. This issue of *IEEE Microwave Magazine* focuses on using DSP techniques for RF identification (RFID) systems. As the name implies, RFID is a technology for wireless object recognition. Typical RFID systems consist of at least one reading device and multiple mobile nodes, often referred to as *tags*. The most common related standards apply to low-frequency (LF), high-frequency (HF), and ultrahigh-frequency (UHF) RFID.

LF RFID works in the band between 125 and 135 kHz and is mainly used for animal tracking. HF RFID



©SHUTTERSTOCK.COM/ANDREY SUSLOV

is the most common standard and is used for many applications. HF RFID tags are widely employed for access control in electronic passports and for secure payment solutions. Most modern smartphones also utilize near-field communication, which is based on HF RFID technology. Both LF and HF RFID operate in the electromagnetic near field. The reading device and tags are coupled inductively and form a loosely coupled transformer. With the help of this link, the reader and the tags can communicate with one another by means of load modulation.

In addition, power for the tag operation can be transmitted from the reader. Since the energy is wirelessly conducted in the near field, the achievable communication distance for LF and HF RFID is shorter than 1 m.

In contrast to the first two standards, UHF RFID works in the electromagnetic far field. It operates at much higher frequencies, either from 865 to 868 MHz or from 902 to 928 MHz. Instead of load modulation, the communication from the tag to the reader

employs backscatter modulation. This principle dates to the 1940s, when Harry Stockman published an article about communication by means of reflected power [1]. In general, wireless data transmission requires altering the amplitude, phase, and frequency of an electromagnetic wave. Classic wireless systems directly create this type of signal. For backscatter communication, however, the reader transmits a continuous wave signal to the tag. A part of this signal is reflected back to the reader and modulated by changing the tag's reflection coefficient

Thomas Ussmueller (thomas.ussmueller@uibk.ac.at) is with the University of Innsbruck, Innsbruck, Austria. Christian Carlowitz (christian.carlowitz@fau.de) is with the University of Erlangen–Nuremberg, Erlangen, Germany.

Digital Object Identifier 10.1109/MMM.2020.3042033
Date of current version: 3 February 2021

according to the data stream. The big advantage of backscatter communication is that it does not need any complicated transmission circuitry. Where typical RF systems require a mixer, a phase-locked loop, a power amplifier, and various other components in the transmit path, a backscatter system in its simplest form can be realized with a switch. That way, RF systems can be orders of magnitude more power efficient.

This issue is a joint effort by two technical committees: IEEE Microwave Theory and Techniques Society (MTT-S) MTT-15 (the RF/Mixed-Signal Integrated Circuits and Signal Processing Committee) and MTT-26 (the RFID, Wireless Sensor, and Internet of Things Committee). In 2019, the committees organized a workshop during the IEEE MTT-S International Microwave Symposium in Boston, "Digital Signal Processing for Radio Frequency Identification." The talks presented during that event form the foundation of this issue. The goal is to disseminate recent results that were made possible by the involved scientists' interdisciplinary research.

The four articles in this issue cover UHF RFID technology advancements achieved via DSP techniques. They target different RFID system layers, starting, in the first two articles, with analog front-end aspects [all-digital data conversion and software-defined radio (SDR) hardware platforms], followed by SDR-based RFID protocols and algorithm testbeds in the third article and localization enhancements on the application layer in the fourth article. In general, DSP-enabled RFID systems are the key technology for novel features such as data encryption [2], sensing capabilities [3], and advanced localization [4], [5].

The first feature, by Arnaldo Oliveira, Nuno Borges Carvalho, João Santos, Alírio Boaventura, Rui Fiel Cordeiro, André Prata, and Daniel Costa Dinis, poses the exciting question: How can flexible UHF RFID readers be

integrated into ubiquitous mobile and small devices? The authors propose and review low-complexity, all-digital transmission and reception methods, which require only a minimal RF front end for amplification and filtering. Generic digital interfaces perform an elegant, very-low-complexity but reconfigurable conversion between the analog and digital domains. Software-defined digital logic implements all RFID signal generation and reception functionality and thus enables a small-size, low-cost development toward novel application scenarios.

The second article, by Edward A. Keehr and Gregor Lasser, discusses all major aspects of a software-defined RFID platform that is sufficiently inexpensive for widespread application in the Internet of Things. The authors' goal is to substantially lower the entry threshold for RFID-enabled applications through a well-documented open source hardware and software project that is accessible to a wide range of engineers, tinkerers, and students. The article covers low-cost leakage cancellation, high-isolation antennas, system architecture and design, and fundamental limitations.

Third, Georg Saxl, Lukas Görtzschacher, Thomas Ussmueller, and Jasmin Grosinger explore how software-defined RFID readers enable enhancements for UHF RFID system functionality in terms of localization and tracking as well as transmission security. They review wireless testbeds and their hardware and scope and propose a secure testbed that facilitates the rapid development and verification of low-power data encryption algorithms in conjunction with crypto-enabled tags. The second part covers a flexible localization testbed for showcasing positioning techniques. Its capabilities are demonstrated in a phase-based localization experiment with outstanding accuracy results.

Finally, the feature article by Matthias Gareis, Andreas Parr, Johannes Trabert, Tom Mehner, Martin Vossiek,

and Christian Carlowitz covers signal processing methods for modern RFID localization based on synthetic aperture radar (SAR). The authors enable an unprecedented 3D position accuracy on the order of a few centimeters that complies with the EPCglobal class 1, generation 2 (Gen2) UHF RFID standard [6] and that uses commercial off-the-shelf tags. Large quantities of tags are localized in complex scenarios, such as a smart warehouse, where a fully automatic stocktaking robot travels along the shelves and establishes synthetic apertures for its antennas. To substantially reduce the computational burden of SAR processing, variable-grid and particle-based search techniques are employed to accelerate the tag positioning by a factor of 1,000 while retaining high accuracy.

We would like to thank *IEEE Microwave Magazine's* editorial board for its encouragement while we planned this issue. Also, we greatly appreciate the support of our MTT-15 and MTT-26 colleagues during the completion of this project. Finally, we thank the authors for their hard work and excellent job communicating DSP methods for enhancing RFID systems to the MTT-S community.

References

- [1] H. Stockman, "Communication by means of reflected power," *Proc. IRE*, vol. 36, no. 10, pp. 1196–1204, Oct. 1948. doi: 10.1109/JRPROC.1948.226245.
- [2] *Information Technology—Automatic Identification and Data Capture Techniques*, ISO/IEC 29167, Jan. 2014.
- [3] T. Ussmueller, D. Brenk, J. Esse, J. Heidrich, G. Fischer, and R. Weigel, "A multistandard HF/UHF-RFID-tag with integrated sensor interface and localization capability," in *Proc. IEEE Int. Conf. RFID (RFID)*, 2012, pp. 66–73. doi: 10.1109/RFID.2012.6193058.
- [4] R. Miesen et al., "Where is the tag?" *IEEE Microw. Mag.*, vol. 12, no. 7, pp. S49–S63, Dec. 2011. doi: 10.1109/MMM.2011.942730.
- [5] A. Costanzo, D. Masotti, T. Ussmueller, and R. Weigel, "Tag, you're it: Ranging and finding via RFID technology," *IEEE Microw. Mag.*, vol. 14, no. 5, pp. 36–46, July–Aug. 2013. doi: 10.1109/MMM.2013.2259392.
- [6] *Class-1, Generation-2 UHF RFID Protocol for Communications at 860 MHz–960 MHz Version 1.2.0*, EPCglobal Inc. (Oct. 23, 2008).



All-Digital RFID Readers

*Arnaldo S. R. Oliveira,
Nuno Borges Carvalho,
João Santos,
Alírio Boaventura,
Rui Fiel Cordeiro,
André Prata, and
Daniel Costa Dinis*



Radio-frequency identification (RFID) readers are the main bottleneck when building an RFID system. The cost of the readers can be high, and these devices can be bulky. Moreover, when these RFID readers have to be included in a small mobile device, the cost increases, or the system becomes more complex to put together.

One solution to this problem is to include the RFID reader right on the system processor and make it completely digital and software based. In this case, the approach is to use a complete solution based on all-digital RF transceivers, with signal processing and software to implement the system fully in the digital domain. This would allow the reader to be updated like a traditional software application and

be agile enough to cope with past, present, and future RFID standards.

In this article, we present an RFID reader that is implemented entirely on a field programmable gate array (FPGA) chip and/or embedded processor, and we discuss approaches to move the research field in this direction. Readers who are interesting in specific implementation strategies are directed to the technical report [1] where all of the details of this implementation are described.

The All-Digital Concept for RF Systems

The increased movement toward the digitalization of conventional analog front ends has opened the door to the concept of software-defined radio (SDR). This concept aims at having one agile radio transceiver front

Arnaldo S. R. Oliveira (arnaldo.oliveira@ua.pt), Nuno Borges Carvalho (nbc Carvalho@ua.pt), João Santos (joaoricardobsantos@gmail.com), Alírio Boaventura (alirio Boaventura@gmail.com), Rui Fiel Cordeiro (rfielcord@gmail.com), André Prata (prata.22@gmail.com), and Daniel Costa Dinis (danielcostadinis@gmail.com) are with the Instituto de Telecomunicações and Departamento de Electrónica, Telecomunicações e Informática, Universidade de Aveiro, Campus Universitário de Santiago, Aveiro, 3810-193, Portugal.

Digital Object Identifier 10.1109/MMM.2020.3042045

Date of current version: 3 February 2021



©SHUTTERSTOCK.COM/ANDREYNIKOLAEV.COM

end that is completely independent of any specific standard and is able to deal with different frequency bands. The relevant state of the art is pointing toward all-digital transmitters (ADTs) as the ultimate target for this technology due to their inherent fully digital behavior from end to end. The research on this class of transmitters is focused on the development of reconfigurable, agile, multiband, multistandard, and highly efficient solutions [2], [3]. Recent advances in the architectures of these transmitters have undoubtedly contributed to their ascendancy, largely by enabling the transmission of radio signals using a fully digital data path. This section summarizes the main foundations of this concept.

All-digital RF transmitters are a particular subset of SDRs that has attracted much attention and renewed interest

from both industry and academia. The underlying idea is the encoding of an n -bit digital signal into a representation with a lower number of bits, enabling the removal of external digital-to-analog converters and upconversion stages. Most of the reported transmitters explore the use of reconfigurable and on-chip 1-bit topologies to transmit signals [3]–[5]. The use of single-bit transmitters leads to signals with constant envelopes that can be amplified by highly efficient and nonlinear amplifiers, such as switched-mode power amplifiers (SMPAs). With such an approach, the analog front end is reduced to amplification, filtering, and radiation. The first attempts to achieve single-bit and efficient power amplification through the utilization of delta-sigma modulators (DSMs) or pulsewidth modulators (PWMs) were applied to low-frequency applications [6].

These implementations have shown that highly efficient and nonlinear amplifiers are feasible, and this has motivated several academic researchers to explore the RF scenario. The need to achieve the gigahertz frequency range has triggered vigorous research in this area. In [7], pulse encoding techniques were applied to the signal magnitude to change the PA bias. Others have designed a pulse shaping stage that is added to the in-phase (I) and quadrature (Q) components of the signal followed by analog wideband mixers through the multiplication of the signal with a binary waveform representation of the carrier frequency [8] or with bulky and high-cost external high-speed multiplexers [2], [9], [10].

While some have opted for the implementation of these types of modulators in integrated circuits [11], [12], others have emphasized the FPGA's inherent flexibility and reprogrammability. Among the latter, the idea of discarding the external components required for the upconversion stage (either analog wideband mixers or high-speed multiplexers) unleashed

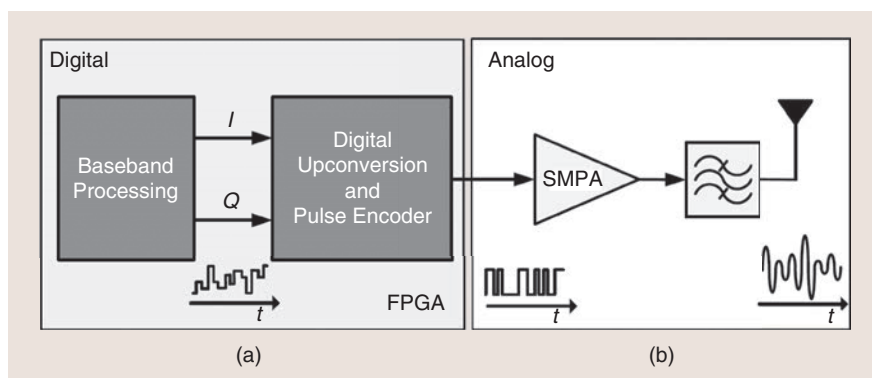


Figure 1. An illustration of the general ADT architecture. For convenience, the mixed-domain serializer that converts (a) the digital signal into (b) an analog pulsed waveform was omitted.

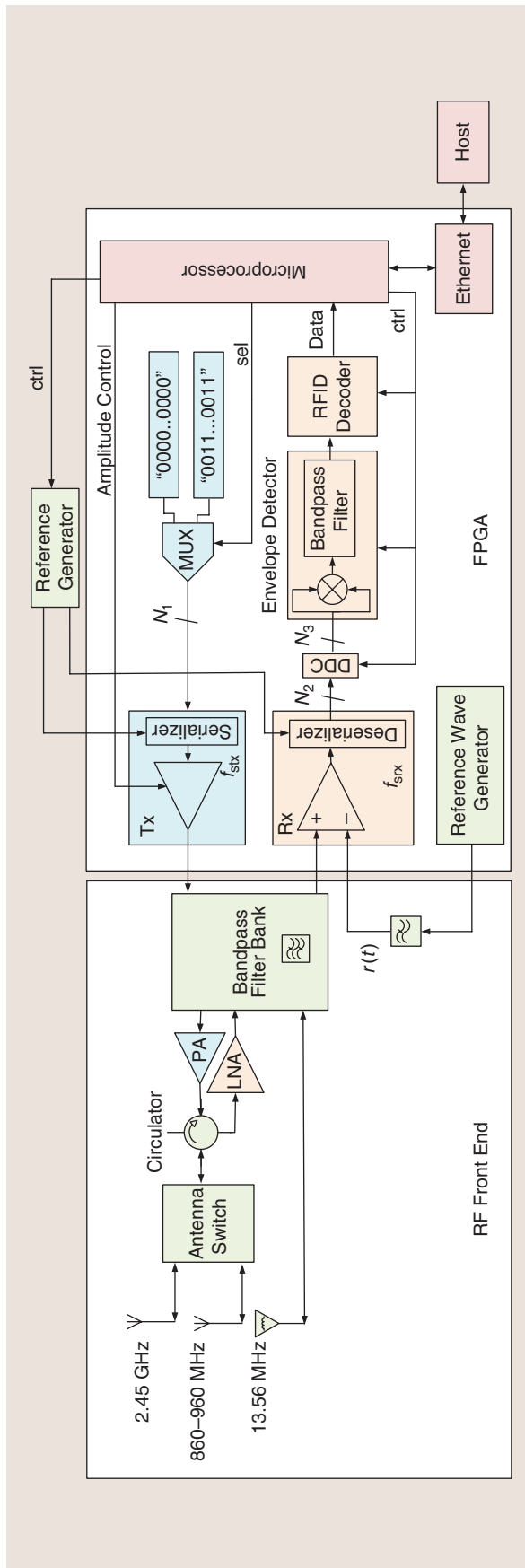


Figure 2. The proposed FPGA-based multiprotocol all-digital RFID reader. LNA: low-noise amplifier; DDC: digital downconversion; Tx: transmitter; Rx: receiver; MUX: multiplexer; sel: select; ctrl: control.

intense investigation in the sense of going further and inserting the design of a digital upconverter (DUC) stage within a single FPGA. This idea was achieved through the utilization of multigigabit transceivers (MGTs) that are present in medium/high-end FPGAs [13], [14]. These MGTs are power-efficient transceivers with embedded serializers; they are highly configurable and tightly integrated with the FPGA's programmable logic resources. As an example, line rates from 500 Mb/s up to 32.75 Gb/s are available in the GTY transceivers from Xilinx Ultrascale+ FPGAs [15]. This small step was of paramount importance for getting closer to the goal of having completely flexible and integrated transmitters.

The general block diagram of an FPGA-based ADT is depicted in Figure 1. The baseband complex input signal is divided into the I/Q data components before being converted into a two-level representation. This conversion is done with an oversampled DSM or PWM pulse encoder. The DUC can be placed either before or after the pulse encoder. In short, the output from the ADT is a pulsed waveform that contains the digitally modulated signal at a given RF carrier frequency together with the out-of-band noise. After amplification, a bandpass filter is required to reconstruct the desired modulated signal before radiation.

Applying All-Digital to RFID

This section describes the proposed all-digital RFID reader architecture (depicted in Figure 2), focusing separately on the transmitter and the receiver paths. The proposed implementation is based on FPGA technology, endowing the system with high configurability and flexibility, both of which are important for building a multiband and multistandard reader.

Transmitter Path

An RFID reader starts its reading task by exciting a tag that implements a particular RFID protocol. The protocols are handled by the embedded microprocessor (μP) implemented on the FPGA. After baseband protocol processing, there is an upconversion component responsible for translating the baseband signal to its RF representation. Traditional RF transmitters perform this upconversion in the analog domain after the digital-to-analog conversion. In an ADT, the data path is entirely digital (from the baseband up to the RF stage), providing high agility and allowing it to profit from accurate digital signal processing techniques. Current ADT architectures are suitable for quadrature complex modulation schemes; however, to deal

with modulation schemes such as on-off keying, amplitude shift keying (ASK), frequency shift keying, and phase shift keying, all of which are commonly used in low bit-rate data transfer, the architecture can be simplified to the one presented in this article (see Figure 2).

The majority of RFID protocols are based on ASK modulation schemes, which can be easily implemented by controlling the amplitude of the carrier wave or even turning it on and off depending on the symbol to transmit. Thus, focusing on Figure 2, depending on the symbol to transmit, the μP will select a parallel word of N_1 bits to serialize, which can be one of two options ("0101...01" or "0000...00") that, respectively, correspond to the presence and absence of the carrier wave.

The serializer works at a frequency of f_{stx} that is related to a given reference clock frequency (f_{refclk}) by a factor F_1 due to its internal phase locked loop (PLL). This equation can be represented as

$$f_{stx} = f_{refclk} \times F_1. \quad (1)$$

Consequently, the carrier wave frequency (f_c) for this case is defined by

$$f_c = \frac{f_{stx}}{2}. \quad (2)$$

Therefore, simply by changing the serializer clock frequency, it is possible to change its sampling rate and thus the carrier placement. Since there is interest in fine tuning the carrier, the periodicity of the digital word "010...01" can be changed, which increases the system's agility. Then, a second factor k is added that defines the periodicity of the sequence "01" in the previous word (e.g., if $k = 2$, the sequence will be "0101...01," and if $k = 4$, the sequence will be "00110011...0011"). At this point, the carrier frequency assumes a new expression defined by

$$f_c = \frac{f_{stx}}{k}. \quad (3)$$

Combining (1) and (3), we obtain a more general equation defined by

$$f_{refclk} = \frac{(f_c \times k)}{F_1}. \quad (4)$$

Table 1 presents the parameter values used in the transmitter path of the all-digital RFID reader.

On the other hand, it is necessary to shape the transmitted signal to fit the imposed transmission power mask, as described in [16]. Since it was not possible to implement a digital filter in the serializer, it is necessary to control the carrier amplitude. This amplitude is also managed by the μP that dynamically changes the peak-to-peak voltage of the serialized waveform

depending on the symbol to transmit. After the serialization, a square wave is generated that carries the signal's information at its fundamental frequency. This signal needs to be amplified and filtered before feeding the RFID antenna.

In the amplification stage, a wideband amplifier is connected to a switch that is capable of driving the signal to the proper low-pass filter (LPF) bank and antenna depending on the carrier frequency. To implement the proper analog LPF bank, the filters' cutoff frequencies (f_{cutoff}) must fall into the frequency range presented by

$$f_c < f_{cutoff} < 2f_c. \quad (5)$$

Receiver Path

Depending on the RFID protocol, the RF receiver front end selects the signal from the correct antenna, which is then followed by a filter bank and an LNA similar to the transmitter case (see Figure 2). Then, the amplified and filtered analog signal is converted to the digital domain.

The digital conversion is based on PWM first presented in [17] and in [18], where a wide analog input bandwidth architecture was implemented in a single FPGA chip. As presented in Figures 2 and 3, to perform the analog-to-digital conversion, a single comparator is required, using as inputs the RF filtered signal $x(t)$ and a 40-MHz reference signal $r(t)$.

TABLE 1. The parameters used in the transmitter path.

Parameter Name	Meaning	Value
Parallel word number of bits	N_1	64
PLL multiplication factor	F_1	32
Serializer frequency	f_{stx}	5 GHz
Period of the sequence (number of bits)	$k(f_c = 13.56 \text{ MHz})$	400
	$k(850 \text{ MHz} < f_c < \text{MHz})$	4
	$k(f_c = 2.45 \text{ GHz})$	2

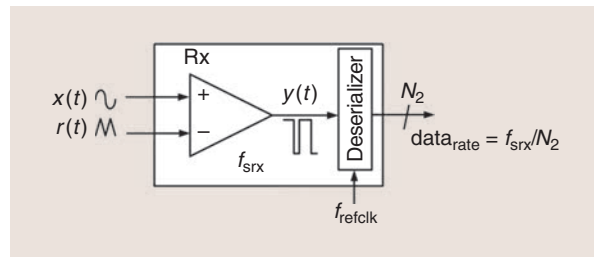


Figure 3. A block diagram of the RFID receiver PWM converter.

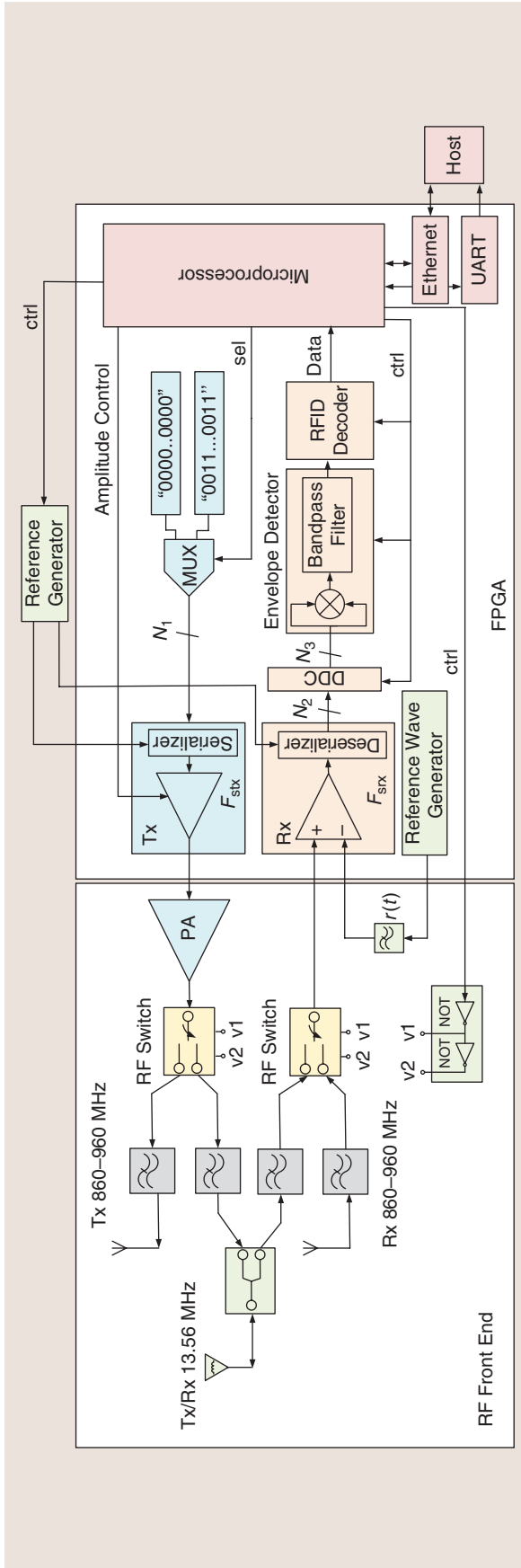


Figure 4. The experimental measurement setup. NOT: inverter logic gate; UART: universal asynchronous receiver/transmitter.

The reference signal should present an amplitude that is greater than or equal to the RF signal, which is achieved by the variable gain amplifier. Ideally, the reference signal should be a triangular wave since it presents a uniform amplitude distribution that allows the RF signal to be equally quantized [19]. Nevertheless, if a slight decrease in the receiver's dynamic range is tolerable, a sinusoidal waveform can be used.

This is the approach used in this article by generating a square wave in the digital domain; then, using an LPF filter, a sinusoidal waveform is obtained to feed the comparator (Figure 4). On the other hand, the frequency of the reference signal imposes the maximum bandwidth of the signal to be acquired, which in the RFID case is a few hundred kilohertz. Consequently, following the diagram in Figure 4, at the comparator output there is a two-level PWM representation of the analog signal $y(t)$ that is expressed by

$$y(t) = \text{sign}(x(t) - r(t)). \quad (6)$$

The PWM representation will be sampled at a rate of f_{srx} . In this case, the high-speed differential input buffers of the FPGA are used to build the comparator and the sampler, which enables the design of a single-chip integrated RFID reader system. The sampling process works at 10 Gb/s, after which the digital PWM signal is converted to a parallel word of N_2 bits by the deserializer, allowing the data to be processed at a lower sampling rate (datarate), given by

$$\text{datarate} = \frac{f_{\text{srx}}}{N_2}. \quad (7)$$

Therefore, after sampling, the RF digital signal must be downconverted to the baseband, filtered to remove the PWM distortion, and decimated by a factor of R to a suitable sampling rate for baseband processing and decoding. This task is performed at the digital down-converter (DDC) block, which comprises a polyphase digital direct synthesis and a polyphase filter with N_2 parallel paths.

After the DDC, the carrier signal is an N_3 bits parallel word, centered at an intermediate frequency (IF) of 2 MHz, although it can be modified to be centered between the values described by (8), where f_{sDDC} is the DDC output sample rate presented in (9):

$$0 < IF < f_{\text{sDDC}}/2, \quad (8)$$

$$f_{\text{sDDC}} = \frac{\text{datarate}}{R}. \quad (9)$$

Table 2 details the parameter values used in the receiver path.

The received RFID signal is ASK modulated; one of the most common approaches to demodulating ASK signals is an envelope detector [20]. As one can see in Figure 3, the implemented envelope detector is

composed of two stages. In the first stage, the RFID signal is multiplied by itself (squared) to translate one of its intermodulator products to dc. In the second stage, a reconfigurable bandpass finite impulse response (FIR) filter attenuates the dc and isolates the RFID signal of interest. For each protocol, a set of filter coefficients that are suitable for obtaining the RFID baseband signal was implemented. Those coefficients were generated using the MATLAB Filter Design and Analysis Tool. The obtained baseband signal is generated by a matching RFID decoder algorithm specific for each protocol and controlled by the μP .

Self-Jamming

At the receiver, the input RFID signal is multiplied by itself (squared) to translate one of its intermodulator products to dc, which causes an unwanted self-jamming effect. Therefore, as stated in [22], a “dc offset removal in the digital domain” is implemented (no need for an analog self-jamming cancellation). A reconfigurable bandpass Kaiser window FIR filter is used, where a set of different coefficients is generated for each RFID protocol.

FPGA Implementation and Measurements

This section presents the implemented all-digital FPGA-based RFID reader’s performance at the ultra-high frequency (UHF) band based on a set of experiments conducted to measure the reader’s power and compare it with the protocol specifications. The maximum reading range and identifier error rate for different reading distances were also measured.

As described in [21], in a UHF RFID system (reader and tag), there are some characteristics that are important for the forward link (reader-to-tag) and others that are important for the return link (tag-to-reader). Some of these system characteristics are inherent only to the tag, such as tag sensitivity and backscatter efficiency. Others, such as read range and backscatter range, also depend on the reader capabilities and the environment.

The implemented experimental setup block diagram is described in Figure 4, and its key elements are illustrated in Figure 5. This setup is composed of a host computer that can handle an RFID user application; an Xilinx Kintex-7 FPGA KC705 evaluation board, where the all-digital RFID reader is implemented; two 1-GHz LPFs; two 20-MHz LPFs; two wideband (300-kHz–2.5-GHz) RF switches; an RF wideband (10–4,200-MHz) PA; one 20-MHz Wilkinson power divider/combiner; one HF antenna; and finally, two UHF commercial antennas. One particularity of this FPGA is its gigabit transceivers. These transceivers, available in medium-end FPGAs, are of great interest because they can be used as serializers/deserializers capable of a maximum bit rate of 12 Gb/s.

RFID readers at UHF must meet two transmission power masks: multiple-interrogator and dense-interrogator.

Performance Tests at the UHF Band

This section features the RFID reader’s performance at the UHF band (915.25 MHz). The tag was programmed to respond with a 200-Kb/s data rate and an FM0 codification. The architecture presented in Figure 4, together with a UHF RFID tag with a theoretical sensitivity of -20 dBm, was used to obtain the presented results.

As stated in [16], RFID readers at UHF must meet two transmission power masks: multiple-interrogator and dense-interrogator. Figure 6 illustrates these two masks and the implemented all-digital RFID reader transmitted power mask. Table 3 gives the measured results.

Conclusions

In this article, an implementation of an all-digital RFID reader was presented and discussed, and it was

TABLE 2 . The parameters used in the receiver path.

Parameter Name	Meaning	Value
Number of parallel paths before the DDC	N_2	64
Number of parallel paths after the DDC	N_3	16
Decimation factor	R	15
PWM sample rate	f_{srx}	10 GHz
Reference clock frequency	f_{refclk}	156.25 MHz

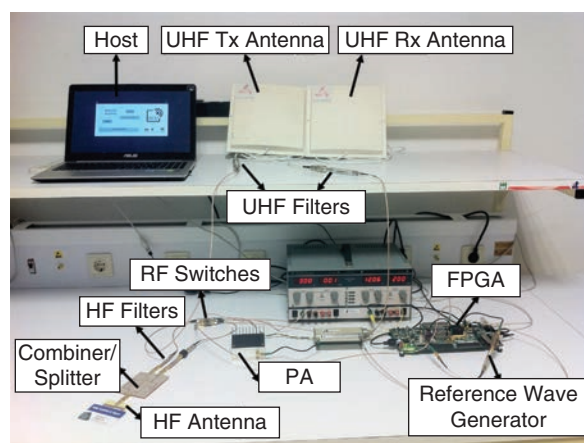


Figure 5. A photo of the implemented all-digital, multiprotocol FPGA-based RFID reader.

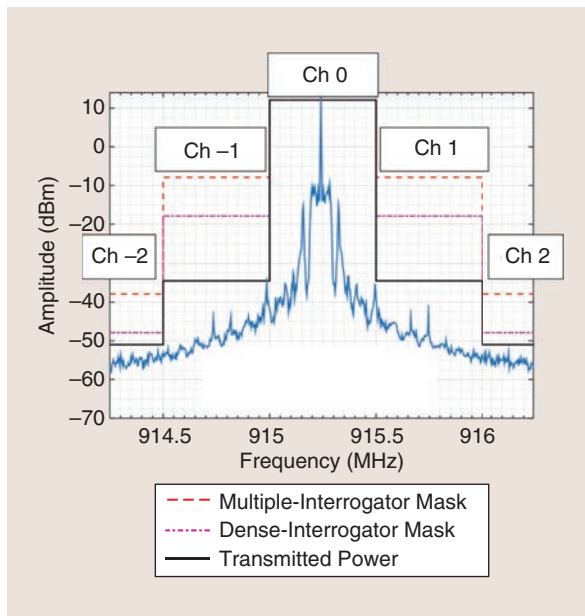


Figure 6. The implemented RFID reader UHF power mask. Ch: channel.

TABLE 3. The transmission mask measured at UHF.

Channel Number	Multiple-Interrogator Mask (dBch)	Dense-Interrogator Mask (dBch)	Transmitted Power (dBch)
0	0	0	0
1	-20	-30	-46.6
2	-50	-60	-63.1
-1	-20	-30	-46.6
-2	-50	-60	-63.1

dBch: decibel-channel.

demonstrated that the approach is feasible for the future of RFID readers. Thus, someday, this technology may be included in all gadgets like mobile phones, laptops, and tablets.

References

- [1] J. B. dos Santos, A. S. R. Oliveira, and N. B. de Carvalho, "FPGA based all-digital multi-protocol RFID reader," 2016. [Online]. Available: <https://www.it.pt/Publications/NonRefereedPublication/46>
- [2] M. Helaoui, S. Hatami, R. Negra, and F. M. Ghannouchi, "A novel architecture of delta-sigma modulator enabling all-digital multiband multistandard RF transmitters design," *IEEE Trans. Circuits Syst. II, Exp. Briefs*, vol. 55, no. 11, pp. 1129–1133, 2008. doi: 10.1109/TCSII.2008.2003345.
- [3] N. V. Silva, A. S. R. Oliveira, and N. B. Carvalho, "Novel fine tunable multichannel all-digital transmitter," in *Proc. IEEE MTT-S Int. Microw. Symp. Dig.*, 2013, pp. 1–3.
- [4] J. Chen, L. Rong, F. Jonsson, and L. R. Zheng, "All-digital transmitter based on ADPLL and phase synchronized delta sigma modulator," in *Proc. IEEE RFIC Symp. Dig.*, June 2011, pp. 1–4.
- [5] N. V. Silva, A. S. R. Oliveira, and N. B. Carvalho, "Evaluation of pulse modulators for all-digital agile transmitters," in *Proc. IEEE MTT-S Int. Microw. Symp. Dig.*, 2012, pp. 1–3.
- [6] R. E. Hiorns and M. B. Sandler, "Power digital to analogue conversion using pulse width modulation and digital signal processing," *IEE Proc. G (Circuits, Devices Syst.)*, vol. 140, no. 5, pp. 329–338, 1993. doi: 10.1049/ip-g-2.1993.0055.
- [7] M. Nielsen and T. Larsen, "A transmitter architecture based on delta-sigma modulation and switch-mode power amplification," *IEEE Trans. Circuits Syst. II, Exp. Briefs*, vol. 54, no. 8, pp. 735–739, 2007. doi: 10.1109/TCSII.2007.899457.
- [8] M. A. Morin, "A 1.6 Gb/s Delta-sigma modulator with integrated wideband mixer for RF applications," in *Proc. Bipolar/BiCMOS Circuits Technol. Meeting*, 1998, pp. 148–151.
- [9] F. M. Ghannouchi, S. Hatami, P. Aaki, M. Helaoui, and R. Negra, "Accurate power efficiency estimation of GHz wireless delta-sigma transmitters for different classes of switching mode power amplifiers," *IEEE Trans. Microw. Theory Techn.*, vol. 58, no. 11, pp. 2812–2819, 2010. doi: 10.1109/TMTT.2010.2077552.
- [10] P. Wagh, P. Midya, P. Rakers, J. Caldwell, and T. Schooler, "An all-digital universal RF transmitter [CMOS RF modulator and PA]," in *Proc. IEEE Custom Integr. Circuits Conf.*, 2004, pp. 549–552.
- [11] K. Muhammad, R. B. Staszewski, and D. Leipold, "Digital RF processing: Toward low-cost reconfigurable radios," *IEEE Commun. Mag.*, vol. 43, no. 8, pp. 105–113, 2005. doi: 10.1109/MCOM.2005.1497564.
- [12] J. Chen, L. Rong, F. Jonsson, G. Yang, and L.-R. Zheng, "The design of all-digital polar transmitter based on ADPLL and phase synchronized DS modulator," *IEEE J. Solid-State Circuits*, vol. 47, no. 5, pp. 1154–1164, 2012. doi: 10.1109/JSSC.2012.2186720.
- [13] N. V. Silva, A. S. R. Oliveira, U. Gustavsson, and N. B. Carvalho, "A dynamically reconfigurable architecture enabling all-digital transmission for cognitive radios," in *Proc. IEEE Radio and Wireless Symposium Dig.*, 2012, pp. 1–4.
- [14] N. V. Silva, A. S. R. Oliveira, U. Gustavsson, and N. B. Carvalho, "A novel all-digital multichannel multimode RF transmitter using delta-sigma modulation," *IEEE Microw. Compon. Lett.*, vol. 22, no. 3, pp. 156–158, 2012. doi: 10.1109/LMWC.2012.2184744.
- [15] *UltraScale Architecture GTY Transceivers*, User Guide UG578, Xilinx, 2017. [Online]. Available: https://www.xilinx.com/support/documentation/user_guides/ug578-ultrascale-gty-transceivers.pdf
- [16] "EPC radio-frequency identity protocols generation-2 UHF RFID: Specification for RFID air interface protocol for communications at 860 MHz and 960 MHz version 2.0.1," GS1, Apr. 2015. [Online]. Available: <http://www.gs1.org/epcrfid/epc-rfid-uhf-air-interface-protocol/2-0-1>
- [17] S. Maier, Y. Xin, H. Heimpel, and A. Pascht, "Wideband base station receiver with analog-digital conversion based on RF pulse width modulation," in *Proc. IEEE MTT-S Int. Microw. Symp. Dig. (IMS)*, June 2–7, 2013, pp. 1–3.
- [18] A. Prata, A. Oliveira, and N. Carvalho, "An agile and wideband all-digital SDR receiver for 5G wireless communications," in *Proc. 18th Euromicro Conf. Digital Syst. Des. (DSD)*, Aug. 2015, pp. 399–406.
- [19] B. Widrow, I. Kollar, and L. Ming-Chang, "Statistical theory of quantization," *IEEE Trans. Instrum. Meas.*, vol. 45, no. 2, pp. 353–361, Apr. 1996. doi: 10.1109/19.492748.
- [20] D. Dobkin, *Communications Engineering Series: The RF in RFID Passive UHF RFID in Practice*. Amsterdam, The Netherlands: Elsevier Inc, 2007.
- [21] P. V. Nikitin and K. V. S. Rao, "LabVIEW-based UHF RFID tag test and measurement system," *IEEE Trans. Ind. Electron.*, vol. 56, no. 7, pp. 2374–2381, July 2009. doi: 10.1109/TIE.2009.2018434.
- [22] A. Boaventura, J. Santos, A. Oliveira, and N. B. Carvalho, "Perfect isolation: Dealing with self-jamming in passive RFID systems," *IEEE Microw. Mag.*, vol. 17, no. 11, pp. 20–39, Nov. 2016. doi: 10.1109/MMM.2016.2600942.





©SHUTTERSTOCK.COM/VECTORPOUCH

Making a Low-Cost Software-Defined UHF RFID Reader

Edward A. Keehr and Gregor Lasser

In this article, we discuss how one can make, with modern and low-cost tools, a software-defined ultra high-frequency (UHF) RF identification (RFID) reader. Since we have chosen to leave the discussion of the top-level reader implementation until

the very end, an introductory outline is warranted to help guide our audience. We first provide the uninitiated with some background context by answering four questions: What is UHF RFID? How does it work? What happened with UHF RFID? And, finally, what's next? That

*Edward A. Keehr (keehr@super-semi.com) is with Superlative Semiconductor, Carlsbad, California, 92009, USA.
Gregor Lasser (gregor.lasser@colorado.edu) is with the University of Colorado, Boulder, Colorado, 80309, USA.*

Digital Object Identifier 10.1109/MMM.2020.3042046

Date of current version: 3 February 2021

is, how do we envision the technology evolving in the future with the support of a broad community? Second, we describe the fundamental metrics and performance budgeting of RFID readers. Following this, we provide an overview on how to design, make, and automatically tune two critical components of UHF RFID readers: the antenna and transmit leakage canceller. Third, we delve even further into details of the transmit leakage canceller. Finally, we describe the complete high-level architecture of a proposed low-cost reader.

What Is UHF RFID?

To put it briefly, UHF RFID is a technology in which one can affix a tag, often with adhesive backing, to an object and obtain information from the tag at a distance using a reader device with an integrated radio. The tag contains an embedded antenna and a very small microchip that conducts a simple communications protocol with the reader, as depicted in Figure 1. Tags often also harvest RF energy to power themselves, usually from the reader's radio transmission, and are commonly about as big as a medium-size adhesive bandage. The maximum range between the reader and the tag in free space depends on the reader antenna directivity, reader quality, and tag quality but typically varies from roughly 2 to 20 m. As per the dominant EPC Gen 2 specification [1], the most common information to be found on the UHF RFID tag is the electronic product code (EPC). The EPC functions as a wireless bar code that can, in principle, be used to uniquely identify the object to which the tag is attached. In addition to reporting the EPC, special tags have been developed that can sense the temperature [2] of the object to which they are affixed, the moisture level [3] in a given area, and other environmental parameters and relay that information back to the reader.

How UHF RFID Works: Backscatter

Of greatest interest are batteryless passive UHF RFID tags, due to their minimal cost (\approx US\$0.05–US\$0.10 in bulk) and lack of maintenance requirements. Such tags communicate with the reader using a low-power technique known as *backscatter*. Backscatter eschews the power and complexity of a full radio transmit (TX) chain to send data. Rather, a device communicating through backscatter sends data back to a radio receiver by changing the termination on an antenna when incident RF power is present, usually with a switch that shorts out the antenna terminals, as depicted in Figure 2. As the antenna termination changes, so does its scattering coefficient. The portion of the incident signal reflecting off the antenna is now modulated along with the changes in the antenna termination. A reader can then receive this modulated signal and decode the encapsulated information.

In EPC Gen 2, the modulation frequency is known as the *backscatter link frequency* (BLF), and it ranges from 40 to 640 kHz on top of a carrier frequency between 860 and 960 MHz. For backscatter to work, there must be a transmitter sending out a (usually 0.5–2-W) signal for the backscatter device to reflect. This transmitter may or may not be co-located with a receiving terminal. Typically, the tag powers itself from energy harvested during the switching intervals when the switch is open and the antenna is loaded by an impedance-matched internal RF-to-dc power conversion circuit. One can think of backscatter as similar to communicating with a mirror or a shiny object to send Morse code by reflecting the sun or a searchlight while camping or hiking. You might have forgotten a radio or run out of batteries during your excursion, but with a simple mirror you can leverage power generated elsewhere to effect a meaningful long-distance communication scheme.

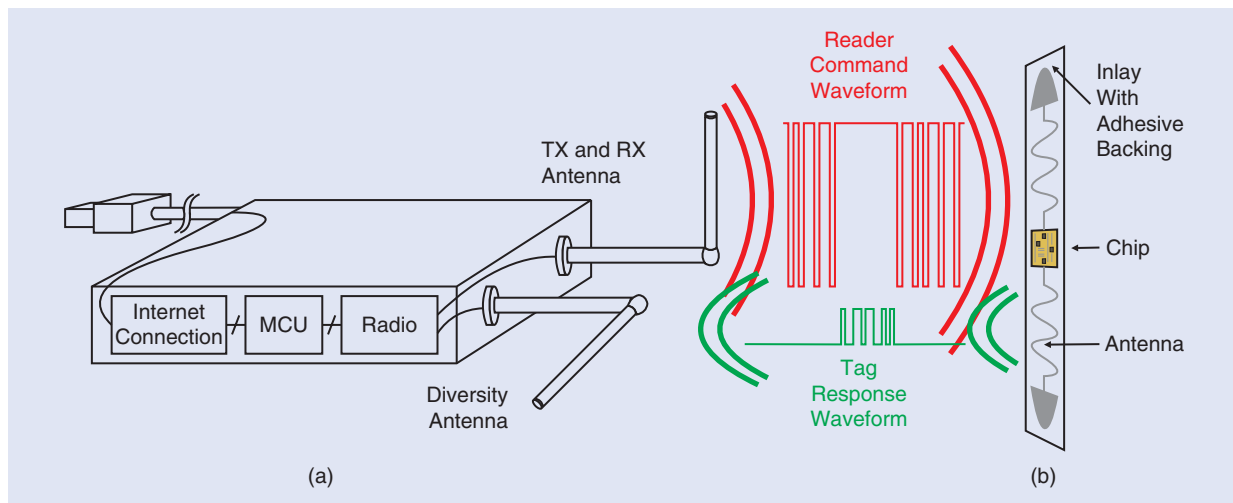


Figure 1. The RFID physical layer concept. (a) The UHF RFID reader. (b) The UHF RFID tag. MCU: microcontroller unit; RX: receive.

Backscatter communications have garnered increasing attention during the 21st century, due to the extremely low onboard power requirements of their nodes. In fact, one could conceivably attach a batteryless, passively powered backscatter radio to everything and connect it to the Internet. At that point, one would have what one could term an Internet of Things. In all seriousness, however, the ubiquity of the phrase “Internet of Things” underscores the myriad applications lying latent and untapped in the public’s imagination that could be realized by backscatter radios. And UHF RFID is a remarkably lightweight implementation of a backscatter radio system. So why don’t we see it everywhere?

The Promise of UHF RFID: What Happened?

When UHF RFID hit the scene around the year 2000, people did expect to see the technology everywhere. The Internet had just succeeded in connecting pretty much every human being living in the developed world, and the next logical step was to connect every object to the Internet. Major publications expected UHF RFID to be ubiquitous in the coming years [4]–[6]. Notably, Wal-Mart issued an edict that its top suppliers were to use RFID technology to track and inventory their shipments [7]. Tech pundits were so concerned about the impact that RFID would have on our everyday lives that some called for an RFID bill of rights [8] and saw in RFID a harbinger of the end times [9].

But That’s Not What Happened

Wal-Mart eventually bailed on its UHF RFID initiative, due to supplier unhappiness with the added costs and technical problems with the then-new technology [7]. Competing technologies made inroads to markets

thought suitable to RFID. In the past, major grocery store chains had studied UHF RFID but concluded that the overall cost of the required infrastructure was too expensive [10]. Today, Amazon is pioneering computer vision for retail grocery, and it appears to be the correct solution for that market [11]. Bluetooth, especially Bluetooth Low Energy (BTLE), has become a consumer market “good enough” Internet of Things enabler because it comes installed on all smartphones. Due to its relatively high minimum peripheral cost, on the order of US\$10, BTLE isn’t the Internet of Everything, but it still covers a fair amount of stuff. Sure, UHF RFID has found niche applications in automotive tolling and high-end apparel retail [12], but it’s not, in general, something that one commonly sees when going about one’s daily life.

What’s Next?

So it should be clear that UHF RFID, or some similar lightweight backscatter technology, is valuable for truly realizing the Internet of Things. But UHF RFID technology hasn’t found its killer app yet. That’s OK. Even the bar code took 20 years from its original patent filing to be used and another 20 years after that to become ubiquitous [13]. Twenty to 40 years is a long time to wait, however. It seems archaic to sit back and wait for someone in a large corporation to come up with a novel and workable vision for RFID, convince management to spend lots of money on it, and then successfully bring it to market. What if, instead, we could all hunt for the killer UHF RFID app together—on the cheap? This is not so easy; dreaming up such an app is only a small fraction of the battle. Building a custom prototype that is best suited to capitalizing on that app is the first major step to proving the idea and attracting outside investment.

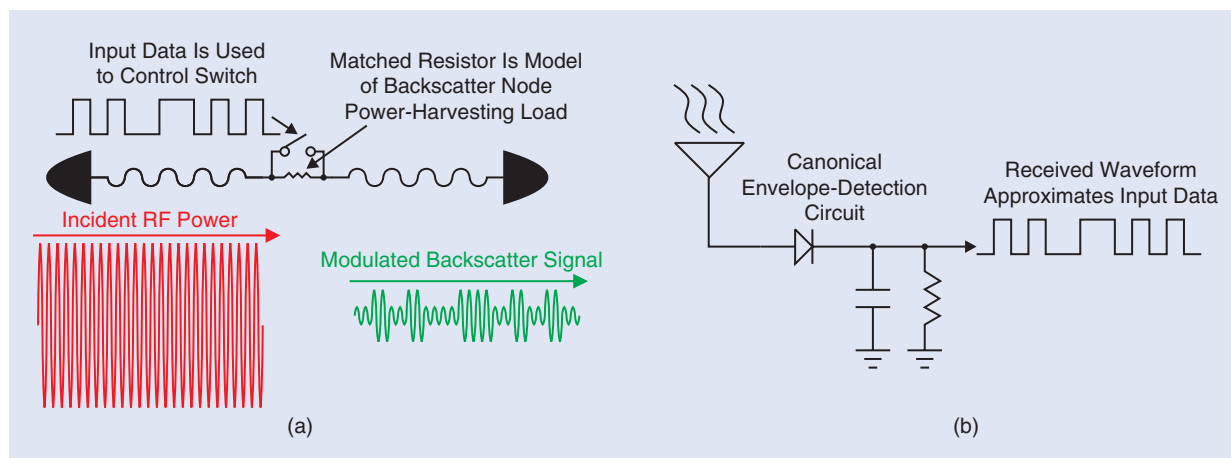


Figure 2. The backscatter concept, with on–off keying as an exemplary modulation scheme. (a) A backscatter node, depicted as an RFID tag, reflects incident RF power differently based on whether a switch across the antenna load is closed or open. (b) A backscatter receiver, depicted as a canonical diode-based envelope-detection circuit, rectifies the incoming RF signal and filters out the high-frequency components, leaving a representation of the original input data to be recovered.

It turns out that the tools of the maker movement enable us to do this, namely, to build hardware prototypes for a nominal price [14], including those of UHF RFID readers and tags. Cheap design software, such as Kicad, Eclipse, and light versions of field-programmable gate array (FPGA) development software, empower anyone with a computer and access to the Internet to design feature-rich customer electronics for free. Printed circuit board (PCB) fabrication can

be accomplished for a few hundred dollars or less by using any one of a number of push-button services. PCB assembly can be done with a US\$40 toaster oven and a US\$150 Reflowster, itself a product of the maker movement. Access to cheap metalworking tools at Maker Spaces facilitates the low-cost manufacture of complex metal geometries [15], potentially including those of novel UHF RFID antennas. Finally, digital sharing and modification of open

TABLE 1. A summary of prior art related to SDR/FPGA-based UHF RFID readers [20].

Reference	Key Components	SDR Bill of Materials Cost	Number of FPGA Logic Elements	Range	Output Power	Comments
[21]	Assorted Linear Technology components, Xilinx Virtex 4 FPGA	> US\$235	> 13,824	Not reported	Not reported	No measured results reported
[22]	Stratix II EP2S60 FPGA, big MCU PCB, big radio PCBs	> US\$874	60,440	6 m	Not reported	Only RX digital described; antenna type unclear
[23], [24], [25]	Various RF parts, Xilinx Virtex II FPGA, Texas Instruments TMS320C6416 digital signal processor	> US\$500	Up to 93,184	11 m (in hall)	35 dBm	Modular, mono-, and bistatic; 5-dBi antenna
[26]–[28]	USRPI radio platform, EP1C12Q240C8 FPGA, RFX900 x1/x2 card	> US\$970	12,060	Up to 6–7 m [26], [27]	27 dBm [26]	Bistatic; 8-dBi antennas [26]
[29], [30]	Various RF parts, Virtex 4 LX100 FPGA, S3C2410 MCU	> US\$2,500	> 110,592	8–9 m	30 dBm	Antenna gain and type not reported
[31]	TH72035 transmitter, MAX931 comparator, MSP430F5510 MCU	> US\$9	N/A (MCU)	0.15 m	9 dBm	Monostatic. dipole antenna (1–2 dBi); not fully tested
[32]	AS3992 RF front end, XC3S500 FPGA	US\$73.55	10,476	3.5 m	N/A	Receiver only; “loop antenna”
[33]	USRP N200 radio platform, Spartan-3A 1800 FPGA, wideband radio (SBX) card	> US\$2,203	> 37,440	Not reported	17.8 dBm	Bistatic; 7-dBi antennas
[34], [35]	USRP-2922 radio platform, Spartan-3A 3400 FPGA, wideband radio (SBX) card	> US\$3,092	> 53,714	“Same as AS3992 evaluation board”	Not reported	Monostatic
[36]	USRP-2942 radio platform, Kintex 7 410 T FPGA	> US\$7,373	> 406,000	> 2.35 m	Not reported	Bistatic
[37]	F28377D MCU, ADF4360-3 phase-locked loop, LT5516 demodulator	> US\$40	N/A (MCU)	Not reported	Not reported	Physically large; manual leakage cancellation; implements only query = 0 transaction
[20] and in this article	SX1257 SDR, MAX 10M02 FPGA, 2 × PE64102, 2 × PE64906, NRF51822QFAA MCU	US\$11.71	2,304	2.6 m (dipole), 15.2 m (patch)	26 dBm	Monostatic; dipole (1.2-dBi)-and patch (12.5-dBi)-antennas measured; 64-cm ² PCB area

dBm: decibels referenced to 1 mW; dBi: decibels relative to an isotropic radiator.

source design files enables us all to go on the hunt for the killer app together.

Open source projects already exist for UHF RFID. The Wireless Identification Sensing Platform project is an implementation of a software-defined UHF RFID tag [16] made up of discrete components, and it is only a bit larger than a typical UHF RFID tag. A somewhat bigger, but easier to assemble, software-defined tag was also recently described [17]. Note that the software-defined aspect of the project is important. When most of the complex design functionality is present in software, in either the microcontroller unit (MCU), FPGA, or both, it becomes much easier for someone holding the hardware to implement and test major changes to the design. It can be done instantaneously, without reinventing the entire project, and for free. There are implementations of software-defined UHF RFID readers, too, but to our knowledge, the ones that are open sourced and publicly available have a high cost, being implemented on US\$1,000-plus Ettus Universal Software Radio Peripheral (USRP) platforms, such as [18] and [19]. Table 1 presents an extensive list of UHF RFID readers based around software-defined radios (SDRs) that have appeared in the academic literature and provided enough information to compute approximate costs.

Therefore, there exists a need for the final tools of the hunt for the killer UHF RFID app: a low-cost software-defined UHF RFID reader and a matching inexpensive, high-performance antenna suitable for a variety of application scenarios. These tools will be the topic of the remainder of this article.

RFID Reader Fundamentals and Hardware Challenges

Passive RFID poses several challenges for the reader architecture since it is a highly asymmetrical communication scheme with the “intelligence” of the system concentrated in the reader to enable simple and cheap tags. In particular, it is different from conventional radio systems in two ways: 1) it uses backscatter communication, and 2) the tag power is provided by the reader. Both points greatly affect the front-end hardware of a reader. Backscatter communication necessitates that the reader TX and receive (RX) paths are simultaneously active, and the TX signal must be strong enough to power the tag. RFID readers therefore face challenges similar to those of full-duplex and simultaneous TX and RX (STAR) systems [38].

To separate the TX and RX paths, one of the antenna access topologies in Figure 3 can be used. Each of these three topologies suffers from some TX-to-RX leakage. Even if one or more of the antenna access topologies

could be made perfect, scattering from nearby objects creates unavoidable leakage. A monostatic reader topology employs a single antenna for transmitting and receiving. A circulator or directional coupler is employed to separate the TX and RX paths. Here, the intrinsic TX-to-RX isolation IS (i.e., how much power leaks from the transmitter into the receiver) is determined by the antenna return loss and the isolation or directivity of the circulator or directional coupler. A bistatic reader topology [Figure 3(b)] uses two separate antennas to achieve isolation. The leakage is primarily determined by the antenna patterns and spacing. The third topology incorporates a single dual-port antenna, where the antenna itself provides isolation. It is true for all scenarios that the intrinsic isolation provided by the antennas and the circulator typically is too small. Some form of analog TX leakage cancellation is required [39]

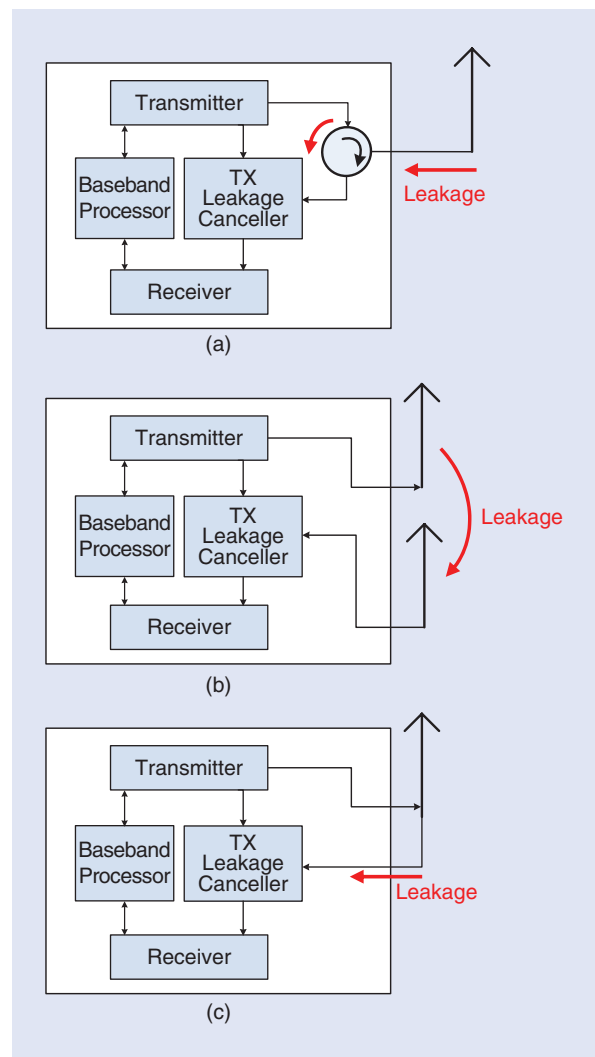


Figure 3. RFID reader access topologies and leakage: (a) monostatic, (b) bistatic, and (c) monostatic with a dual-port antenna.

to avoid blocking in the receiver low-noise amplifier (LNA) or analog-to-digital converter (ADC).

The fact that the tags do not have their own power supply, instead harvesting the radiation produced by the readers, sets a limit on the read range. This is typically called the *forward read limit*, and it is determined by the ability of the readers' TX signal to "wake up" the tags [40]–[43]. Therefore, TX powers on the order of 0.5–2 W are common; 1 W is allowed in the United States, using an antenna with up to 6 dB relative to an isotropic radiator (dBi) [44].

Receiver Noise

Successful communication with a tag requires two things: the power needs to be sufficient to wake up the

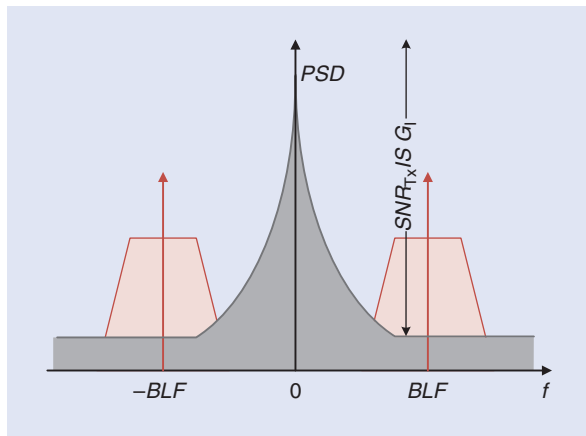


Figure 4. The power spectral density (PSD) of RFID reader-received baseband signals. The dominating leaking transmitter noise components are in gray, and the backscatter signal is drawn in red. Modified from [47, Fig. 3].

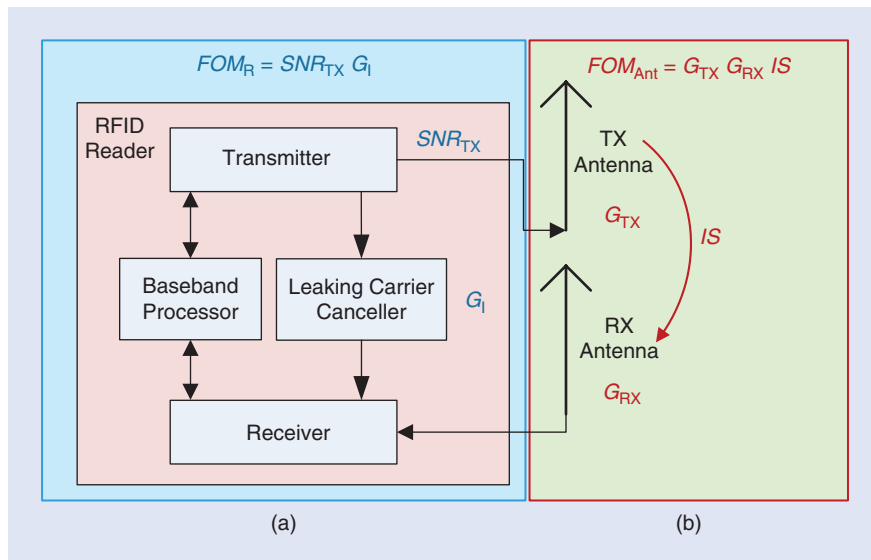


Figure 5. The definition of the FOMs for the example of a bistatic reader. (a) The reader FOM. (b) The antenna FOM.

tag, and the signal-to-noise ratio (SNR) of the backscattered signal must be adequate for the reader to decode the data stream. The second condition, often called *back link limitation*, is mainly determined by the noise present in the reader. While some of it is thermal noise, there is an additional component related to the carrier signal leaking from the transmitter [45]–[47]. Any noise or phase noise of the leaking TX signal will directly end up in the receiver; additionally, the phase noise of the receiver's local oscillator (LO) also contributes to noise in the RX band, due to reciprocal mixing with the leaking carrier [48], [49].

In both cases, the received spectrum at the receiver baseband looks similar to Figure 4. In the center, we note the strong leakage signal, with noise sidebands and a flat noise floor, which adds to the backscattered signal from the tag centered around the BLF. The total noise introduced into the receiver $P_{N,TX}$ due to thermal TX noise, phase noise of the TX signal, and reciprocally mixed LO noise with the transmit carrier can be modeled as a TX SNR SNR_{TX} of the reader's transmitter. Since the effective TX noise spectrum is not flat, SNR_{TX} will depend on the BLF. The noise power in the reader's receiver can then be expressed as

$$P_N = N_{th}F + \frac{P_{N,TX}(BLF)}{IS \cdot G_I} = N_{th}F + \frac{P_{TX}}{SNR_{TX}(BLF)IS \cdot G_I} \\ = N_{th}F + \frac{P_{TX}}{FOM_R(BLF)IS}, \quad (1)$$

where N_{th} is the thermal noise power, F is the noise figure of the receiver, P_{TX} is the TX power of the reader, IS is the intrinsic isolation between the transmitter and receiver, and G_I is the isolation gain of the leakage cancellation circuit, i.e., the ratio of the initial leakage power to the leakage power when using the leakage canceller.

The product of the TX SNR and the isolation gain is a reader quality parameter summarized as FOM_R . The achieved isolation gain will, in practice, depend on the leakage amplitude and phase, but here, for simplicity, it is considered constant. For brevity, we further omit the dependency on the BLF from further equations. The first term in (1) is the thermal noise; the second term is the noise due to the leaking carrier. When this latter term dominates, the SNR at the receiver is given by [47]

$$SNR_{RX_{SI}} = \frac{FOM_R FOM_{Ant} G_{Tag}^2 \eta_{Mod}}{FSPL^2}, \quad (2)$$

where G_{Tag} is the gain of the tag antenna, η_{Mod} is the modulation efficiency of the tag, and $FSPL$ is the free-space loss. The two figures of merit (FOMs) FOM_R and FOM_{Ant} are explained in Figure 5 and motivated by a bistatic or dual-port antenna reader scenario where the intrinsic isolation IS is determined by the antennas and their placement. For high-performance monostatic readers with a good circulator, the intrinsic isolation remains antenna dominated when the antenna return loss is lower than the circulator isolation (see Figure 3).

To demonstrate that the self-interference noise often dominates and that (2) sets the reader SNR, we investigate the monostatic low-cost reader discussed in the final section of this article, “Low-Cost Software-Defined UHF RFID Readers”; the relevant parameters of this reader and the assumed Monza 5-based tag [50] are summarized in Table 2. Using the Friis transmission equation for forward and backward links and the receiver noise from (1), we compute the maximum possible read range:

$$d_{max,rv} = \frac{\lambda}{4\pi} \sqrt[4]{\frac{EIRPG_{RX} FOM_R FOM_{Ant} G_{Tag}^2 \eta_{Mod}}{SNR_{RX_{min}} (EIRPG_{RX} + N_{th} F FOM_R FOM_{Ant})}}, \quad (3)$$

where λ is the free-space wavelength, $SNR_{RX_{min}}$ is the minimum SNR required by the reader to decode the backscattered signal, and $EIRP$ is the equivalent isotropically radiated power from the reader’s transmitter. From the power received at the tag [47, eq. (1)], the forward link limitation, i.e., the maximum distance across which the tag responds, is found:

$$d_{max,fw} = \frac{\lambda}{4\pi} \sqrt{\frac{EIRPG_{Tag}}{P_{Tag_{min}}}}. \quad (4)$$

These limits are plotted in Figure 6 for two different reader antennas. Additionally, we plot the self-interference link limit [47, eq. (10)], which can be computed from (2)

$$d_{max_{SI}} = \frac{\lambda}{4\pi} \sqrt[4]{\frac{FOM_R FOM_{Ant} G_{Tag}^2 \eta_{Mod}}{SNR_{RX_{min}}}}. \quad (5)$$

Assuming fixed-gain antennas, the remaining free parameter for adjusting FOM_{Ant} is the isolation IS between the antennas. We see that, up to a value of $FOM_{Ant} = 20$ dB, both antennas behave in the same way and would result in a read range of 8.6 m. For higher FOMs and a low-gain dipole antenna, the relatively low $EIRP = 27.2$ dB referenced to 1 mW causes the read range to flatten out at 16.3 m, due to thermal noise. However, the forward link limitation (powering the tag) for this case is 5.2 m, so the thermal-noise-limited case cannot be reached. Similarly, for a high-gain patch antenna, the

theoretical forward read range limit is 19.1 m, requiring an antenna FOM of $FOM_{Ant} = 33.6$ dB. This point is still dominated by the self-interference limit $d_{max_{SI}}$. From the gain of the patch antenna, 12.5 dBi, we can compute the required return loss for this FOM to be 8.6 dB, which is easily achieved by a high-quality antenna.

To be forward link limited, the dipole antenna needs to have a return loss of 8.6 dB, which is not always

TABLE 2. Tag and reader parameters.

Sensitivity $P_{Tag_{min}}$	−17.8	dBm
Antenna gain G_{Tag}	1	dB
Modulation efficiency η_{Mod}	−10	dB
Frequency f	915	MHz
Bandwidth B	90	kHz
Noise figure F	26	dB
TX power P_{Tx}	26	dBm
Reader FOM FOM_R	96	dB
Required SNR $SNR_{RX_{min}}$	7	dB

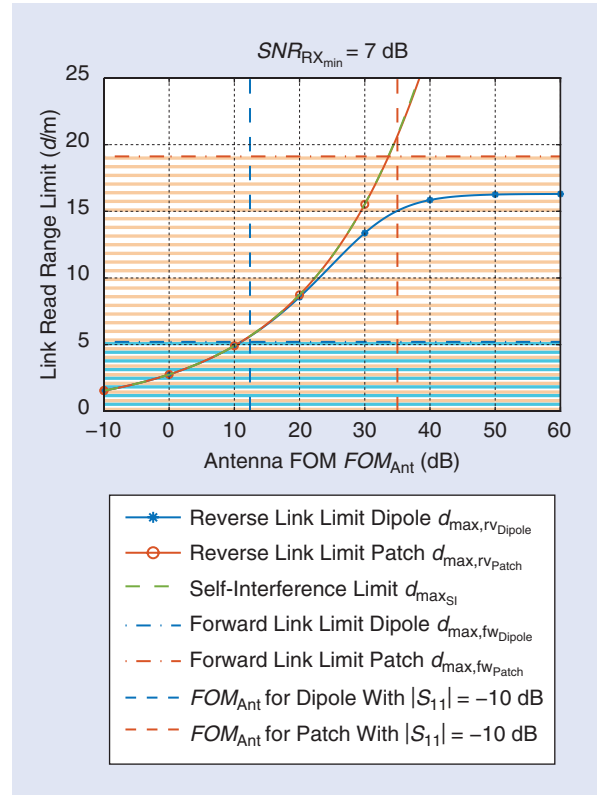


Figure 6. The read range limit d for the presented reader (Table 2) for a dipole and a patch reader antenna. The dipole has a gain of 1.2 dBi, and the patch antenna has 12.5 dBi. The antenna FOMs $FOM_{Ant} = G_{TX}^2 IS$ for a return loss of 10 dB are indicated by vertical lines for the dipole and the patch antennas. The hatched areas show the feasible operation due to forward link limits $d_{max,fw}$ based on a TX power of $P_{TX} = 26$ dBm.

achieved in a realistic scenario where the dipole antenna is directly connected to the reader and influenced by nearby objects. In a practical environment, multipath propagation will also cause fading and range correlation effects of the noise [49], [51]. Assuming a return loss of 10 dB for both antennas, we see that this scenario is forward link limited. Using a tag with a higher sensitivity (e.g., NXP's Ucode7 [52]) raises the forward link limit lines in Figure 6 and results in a reverse-link limited scenario. We conclude that, to achieve forward link limitation, a reader setup must have high reader and antenna FOMs. Those conditions boil down to the following stipulations:

- The reader must have a low TX (phase) noise and a clean receiver LO.
- There must be a leakage canceller with an isolation gain of at least 50 dB.
- There must be well-matched high-gain reader antennas.
- The reader antenna vicinity needs to be free of scattering objects.

Reader Antennas

Depending on the reader access topology (Figure 3), different antenna solutions are feasible. The monostatic configuration, in principle, sets a single requirement for the reader antenna: providing a high return loss ensures a large TX-to-RX isolation IS and therefore a large FOM_{Ant} , assuming a perfect circulator, even for moderate antenna gains. This, in principle, allows for simple dipole-based antennas; however, circular polarization (CP) is preferred in a typical scenario,

where the tag orientation is unknown. Another way to mitigate this problem is to use two cross-polarized antennas and switch between them to be able to read randomly positioned, linearly-polarized tags. CP has another big benefit for RFID readers: the scattering from large metallic objects will be flipped in polarization. An object illuminated by a right-hand CP (RHCP) antenna will scatter left-hand CP (LHCP) fields, which are not received by the RHCP antenna. This reduces the total leakage signal and can mitigate range correlation effects and increased receiver noise.

Most tags use linearly polarized antennas, so their backscattered signals are linearly polarized, as well, causing a 6-dB penalty for CP reader antennas on the reverse link that is independent of the tag orientation. Further, any reader antenna gain improves the antenna FOM (Figure 5) and therefore the reverse-link read range. For bistatic readers, the antenna return loss is less of an issue because the isolation is now defined by the antenna patterns and orientation. This makes the performance of this configuration highly dependent on the exact geometry and the antennas that are used [51], which is a drawback in many applications where the end user is not skilled in radio propagation.

Dual-Port Antennas

The use of monostatic configurations with dual-port antennas in RFID is still very rare, but it offers the substantial benefit of reliably reaching very high antenna FOMs. Table 3 lists several dual-port reader antennas that exceed $FOM_{ANT} > 30$ dB, in chronological order. Many solutions are based on polarization to isolate

TABLE 3. A comparison of dual-port reader antennas.

Description	Patch	Patch Array	Inverted-F Antenna	Patch Array	Concentric Inverted-F Array	Patch With Tuned 3-dB Hybrid	Patch	Patch With 3-dB Hybrid	Four-Arm Spiral
Reference	A [57]	B [58]	C [59]	D [60]	E [55]	F [53]	G [56]	H [61]	I [54]
Frequency	5,400–6,000	2,400–2,500	429–437	860–960	860–960	852–876	900–930	846–929	800–3,500
Bandwidth	10.5%	5%	2%	11%	11%	2.8%	3.3%	7.3%	126%
Isolation	Polar	Polar	Polar	Spacing and polar	Symmetrical beamformer	Polar and tuned hybrid	Symmetrical beamformer	Polar	Symmetrical phase
TX polarity	Horizontal	Horizontal	Horizontal	LHCP	RHCP	RHCP	RHCP	RHCP	RHCP
RX polarity	Vertical	Vertical	Vertical	RHCP	RHCP	LHCP	RHCP	LHCP	RHCP
TX gain	7.8 dBi	14.5 dBi	3.7 dBi	7 dBi	1 dBi	9.5 dBi	8.1 dBi	6 dBi	4 dBi
RX gain	7.6 dBi	14.5 dBi	3.4 dBi	7 dBi	0.7 dBi	9.5 dBi	8.1 dBi	6 dBi	4 dBi
Isolation	28 dB	35 dB	25 dB	36 dB	35 dB	52 dB	45 dB	25 dB	37 dB
FOM_{Ant}	43.4 dB	64 dB	32.1 dB	50 dB	37.7 dB	71 dB	61.2 dB	37 dB	45 dB
Size x	$15.2 \lambda_0$	—	$4.6 \lambda_0$	$6.1 \lambda_0$	$3.9 \lambda_0$	$8.6 \lambda_0$	$4.0 \lambda_0$	$7.5 \lambda_0$	$11 \lambda_0$
Size y	$15.2 \lambda_0$	—	$4.6 \lambda_0$	$13.7 \lambda_0$	$3.9 \lambda_0$	$8.6 \lambda_0$	$4.0 \lambda_0$	$7.5 \lambda_0$	$11 \lambda_0$

All frequency data are in megahertz.

the TX and RX paths (A–D, F, and H) using either dual linear antennas or dual CP. A dual linear antenna configuration in RFID has the significant drawback that tags need to be oriented in a slanted fashion with respect to the TX and RX polarizations to receive enough signal from the reader to wake up but also to scatter back effectively into the reader antenna. Having dual circular polarized antennas avoids this problem with a fixed 3-dB penalty in both the TX and RX paths, but it suffers from the aforementioned problem of increased leakage due to the polarization flip of scattering objects.

The antenna with the highest FOM of 71 dB in Table 3 (F) uses polarization decoupling based on a dual-port patch antenna fed with a 3-dB hybrid coupler. This coupler, as shown in Figure 7, is loaded with varactor diodes and a power detector. It is directly mounted to the ground plane of the patch antenna, and the ports on the right of Figure 7 directly feed the vertical and horizontal ports of a dual, linear-polarized patch antenna, creating CP. A microcontroller running a gradient algorithm (explained in the next section) uses the power detector to continuously adjust the varactor bias voltages and maintain high isolation [53].

Antennas E, G, and I in Table 3 use RHCP to TX and RX in a truly monostatic configuration, and all three achieve isolations greater than 35 dB. This isolation is based on symmetry in the antennas and the beamformers that are used, making the TX currents cancel in the RX path [54]–[56]. Figure 8 explains this principle: a four-arm spiral can be decomposed into two

two-arm spirals shifted by 90°. When the TX arms are fed by a perfectly balanced 180° hybrid, the coupling to the neighboring RX arms is completely cancelled due to the symmetry in the antenna [54]. The resulting TX and RX radiation patterns are identical, except for the 90° rotation. Figure 9(b) shows a practical implementation of this concept using an infinite microstrip balun on a two-layer PCB. The metallic traces are conceptually shown in Figure 9(a). This concept avoids the costly external beamformer and provides 37 dB of isolation while maintaining a gain exceeding 4 dBi across a 126% bandwidth. Since antennas G and I [54], [56] are PCB based, they should lend themselves well to cheap mass production and provide excellent performance.

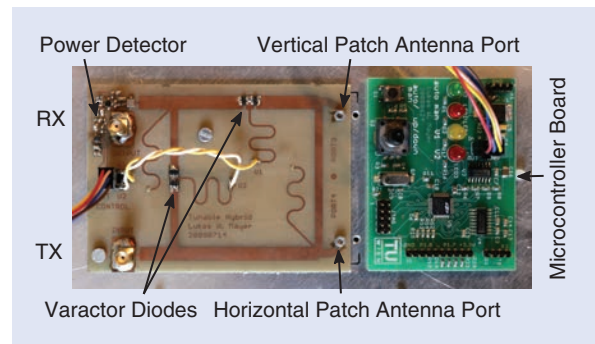


Figure 7. A tunable 3-dB hybrid with an integrated power detector to provide two decoupled ports and feed a dual linear patch antenna to create dual CP. Compare with [53, Fig. 1].

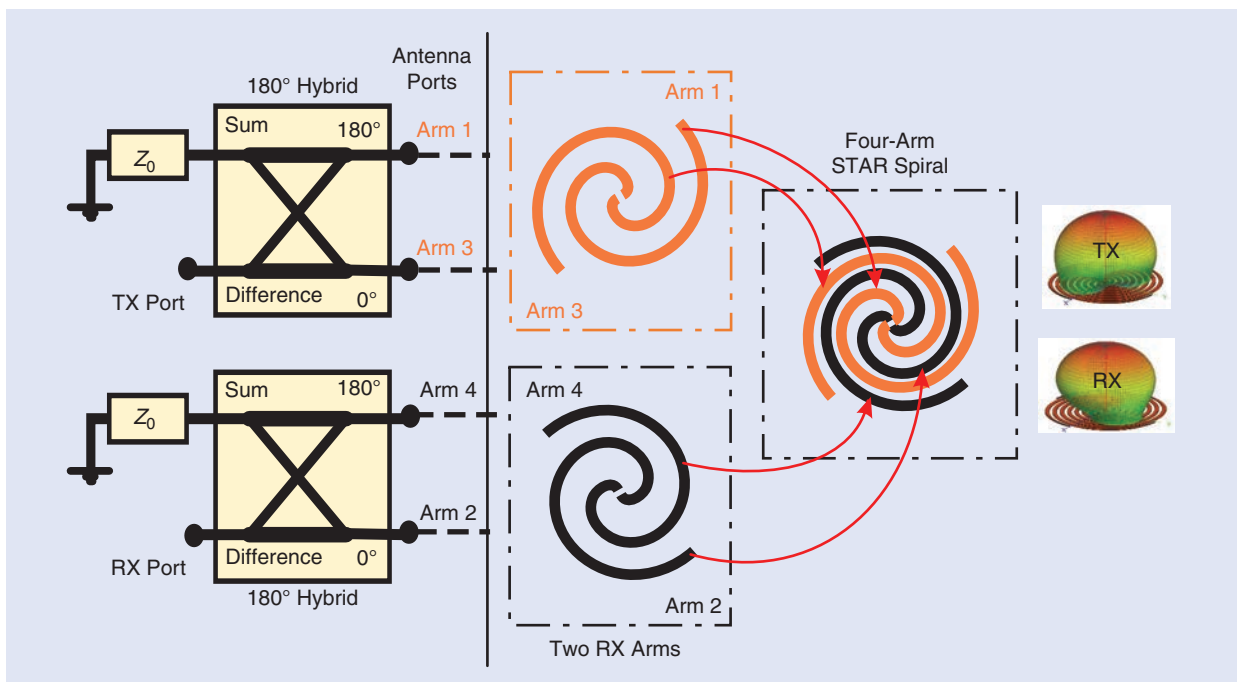


Figure 8. The principle of a four-arm STAR spiral: two two-arm spirals are fed by 180° hybrids. Modified from [54, Fig. 1].

Leakage Cancellers

Leakage cancellers are employed in practically all RFID readers for two reasons: first, they prevent receiver circuit blocking and overloading, and, second, they reduce the effect of TX noise leaking into the receiver, as discussed in the “Receiver Noise” section. To fulfill both goals, they have to provide a second path that takes part of the TX signal and injects it, with the appropriate amplitude and phase, into the receiver so that it cancels the leaking signal [38]. The bandwidth of this cancellation depends on the length difference between the leakage path and the cancellation path [62], which can be a challenge for readers that enable arbitrary cable lengths to be connected between the antennas and the reader.

Another challenge is how to effectively adjust a cancelling circuit, especially since a misadjusted cancelling circuit degrades the system performance. A block diagram of a generic superheterodyne reader receiver appears in Figure 10. The received signal passes a directional

coupler, where the cancellation signal is injected, and a bandpass filter (BPF). The signal is then amplified in an LNA, mixed down to an intermediate frequency, again filtered and amplified by a variable-gain amplifier, and finally digitized in an ADC. Additionally, this block diagram shows provisions for extra power detectors, labeled A–C. Detectors A and B require extra hardware (a detector diode), while detector C is implemented in software. The benefit of the dedicated hardware detectors lies in the fact that they provide meaningful data, even if the receiver is overloaded by a strong leakage signal and a misadjusted or deactivated leakage canceller. This is especially true for detector A since it is situated before the first amplifier and can therefore be designed to be linear up to high power levels. Detector B has the benefit of adding gain to the previous receiver chain but is more susceptible to overloading. The biggest benefit of detector C is the fact that, for many reader architectures, it can provide amplitude and phase information about the leaking signal and

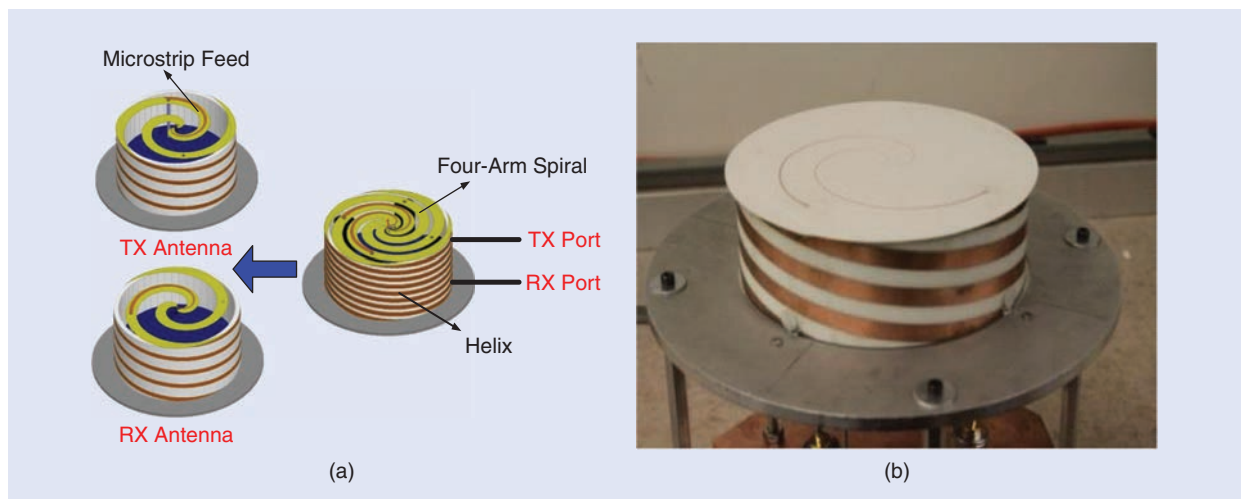


Figure 9. The wideband four-arm spiral antenna I in Table 3 [54]. (a) The decomposition in a separate TX-and-RX two-arm spiral. (b) The manufactured antenna. Modified from [54, Fig. 11].

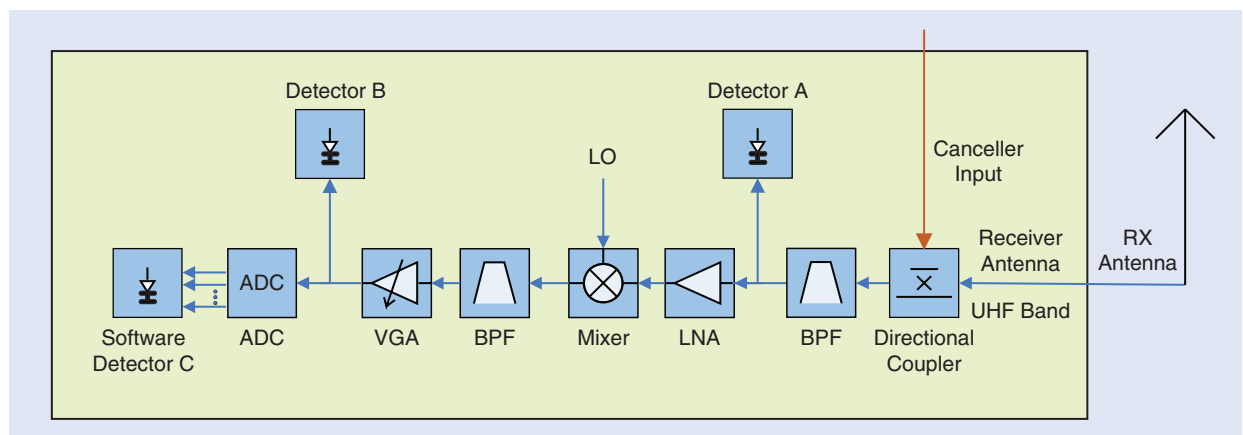


Figure 10. An RFID reader receiver with detector options. It is composed of a directional coupler, a BPF, an LNA, a variable-gain amplifier (VGA), an ADC, and a software detector in the baseband.

therefore can be used to directly adjust a leakage canceler if it is calibrated in amplitude and phase.

A summary of popular adjustment algorithms for leakage cancellers is given in Table 4, sorted from slowest to fastest. We see that the slowest full-search algorithm,

which steps through all possible settings of the canceler circuit, has no calibration requirements and detector linearity constraints. The very commonly used gradient algorithm simply requires a detector that is not fully saturated and a monotonously reacting canceler control. The

TABLE 4. A comparison of canceler adjustment techniques.					
Algorithm	Reference	Detector Type	Detector Linearity Constraint	Speed	Canceler Calibration
Full search	[63]	Power	None	Slow	No
Gradient search	[38], [64], [65]	Power	Low	Medium	Minimal
Fast algorithm	[66], [67]	Power	High	Fast	Yes
Direct I/Q	[68], [69]	Amplitude and phase	High	Fast	Yes

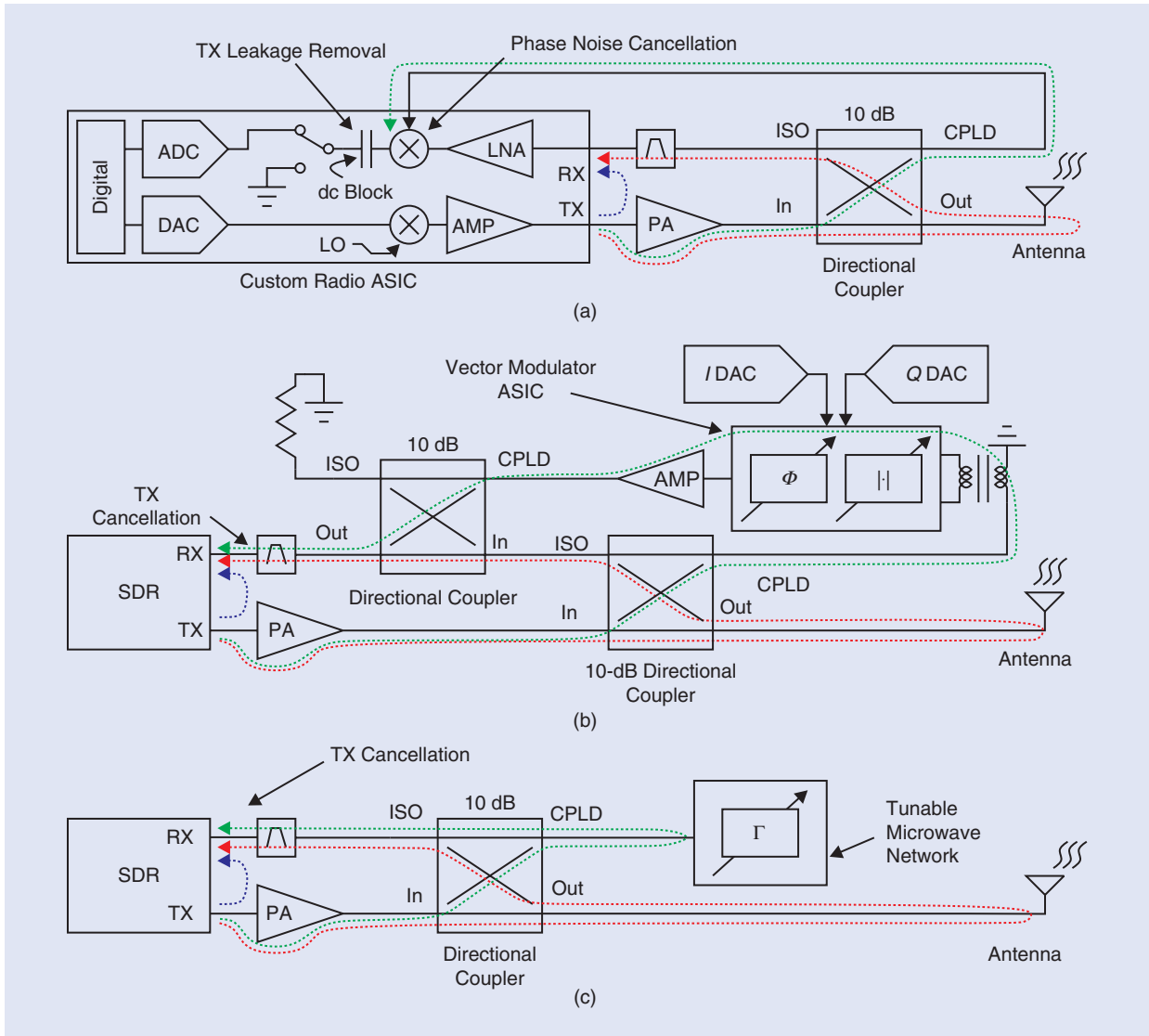


Figure 11. TX leakage cancellation circuit concepts in the UHF RFID literature that are applied to a monostatic reader with directional coupler-based antenna duplexing: (a) an on-chip design, (b) a vector modulator, and (c) a reflected-power canceller. AMP: amplifier; CPLD: coupled port; ISO: isolated port; PA: power amplifier.

Backscatter communications have garnered increasing attention during the 21st century, due to the extremely low onboard power requirements of their nodes.

fast algorithm needs a calibrated canceller and derives the necessary canceller setting from three successive amplitude measurements [66]. Finally, the direct in-phase (I)/quadrature (Q) algorithm requires an amplitude and phase detector and a calibrated canceller. Both referenced implementations [68], [69] achieve this in a pure analog way with a separate analog I/Q detector at location A in Figure 10, but a digital implementation using the software detector C is possible. Many readers also employ two or more algorithms to find the best cancellation setting. For example, it is beneficial to first find a coarse canceller setting that reduces the power levels in the receiver using a “full-search” algorithm and then apply a smarter algorithm to fine-tune that result, utilizing the detectors that were previously overloaded by the strong leakage signal.

Low-Cost Leakage Cancellation Circuits

As described previously, maintaining a large TX-to-RX isolation in a UHF RFID reader is critical to achieving a meaningful tag read range. This proves to be doubly true when using low-cost radio hardware, which will have higher TX and RX phase noise than otherwise. Thousand-dollar reader systems can afford bulky circulators and elaborate cancellation mechanisms to ensure that a pristine tag backscatter signal appears at the radio receiver input. But what if the leakage cancellation circuit needs to cost on the order of US\$3, in bulk? How does one go about

choosing an architecture and improving it, if necessary, to meet the isolation requirements of the system?

Classes of Leakage Cancellation Circuits

In the UHF RFID literature, these authors consider three main classes of leakage cancellation circuit, shown in Figure 11. Each of these circuits can be used in a monostatic or bistatic reader antenna arrangement with some modification. For the purposes of this article, the monostatic arrangement, with TX and RX paths accessing the antenna with a directional coupler, will be discussed and depicted, in keeping with the theme of having a low cost.

On-Chip

As described in [70] and shown in Figure 11(a), to significantly reduce the phase noise resulting from the TX leakage, the mixers in the radio receiver can be driven by a coupled and attenuated version of the transmitter output in place of a receiver LO. This works for UHF RFID because the TX signal is strictly sinusoidal while the reader is receiving the tag’s response. Since the phase noise of the transmitter output and, by design, of the RX LO is naturally highly correlated with that of the TX leakage, when these two signals multiply in the receiver mixer, very little of the phase noise appears at the baseband. The downconverted TX leakage still exists as a low-noise dc signal that can be removed by using resettable ac coupling capacitors or dc-cancelling servo circuits [70]. The advantages of such circuits are that they can be had for a very low incremental cost and that they occupy a very small amount of PCB space. The downside is that the application-specific integrated circuit (ASIC) described in [70] does not appear to be publicly available on major distributor websites, and the fixed cost of

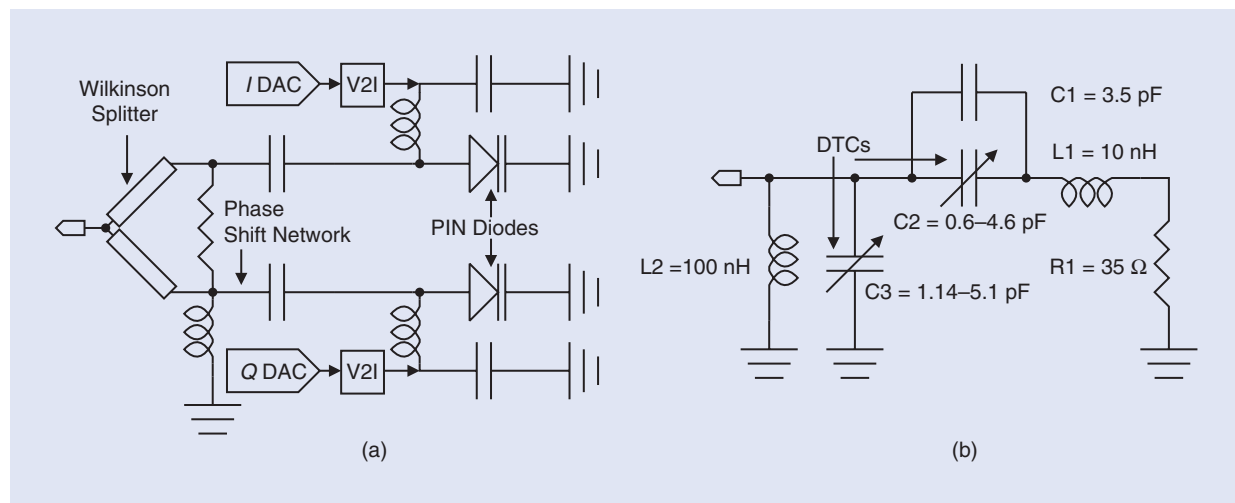


Figure 12. Prior art in UHF RFID reader RPC TMNs: (a) PIN diode-based design [37], [76] and (b) a DTC-based design [77]. V2I: voltage-to-current converter.

developing and sourcing a new ASIC for this purpose can easily run higher than US\$1 million.

Vector Modulator

Perhaps the most obvious approach to improving TX leakage cancellation is to couple off a portion of the transmit signal, explicitly adjust the amplitude and phase of this signal, and then couple the resulting signal back into the RX path. This approach is known as *vector modulation* [Figure 11(b)], and it has been utilized in numerous UHF RFID reader studies [62], [64], [71]–[73]. While vector modulation can be effectively deployed with publicly available ASICs, such alternatives are few (AD8340 and HMC630LP3E) and expensive (US\$10.19 and US\$16.29, respectively, in bulk). In addition, the leakage cancellation path typically requires a balun, two external digital-to-analog converters (DACs), an amplifier to recover from the path losses, and an extra directional coupler. While these supporting devices may be had for US\$1–US\$2 each, in bulk, the cost adds up quickly.

Reflected-Power Canceller

Instead of explicitly processing the coupled transmitter leakage signal through a vector modulator, imagine just bouncing it back into the receiver by using a termination with a reflection coefficient (Γ) equal to the negative of the antenna's (Γ_{ANT}), plus any phase adjustments related to routing mismatches on the PCB. Then, the two reflected signals cancel at the isolated port of the directional coupler. This is the concept

One could conceivably attach a batteryless, passively powered backscatter radio to everything and connect it to the Internet.

behind the reflected-power canceller (RPC) depicted in Figure 11(c). This idea originated in the radar technical literature [74] and was subsequently applied to UHF RFID in [75]. To account for a changing antenna reflection coefficient, RPC architectures with tunable microwave networks (TMNs) used to adaptively generate these arbitrary reflection coefficients (Γ_{TMN}) were reported in the UHF RFID literature [37], [76], [77].

TMNs described for UHF RFID RPCs roughly fall into two categories: those consisting of tunable P-insulator-N (PIN) diodes [37], [76] and those defined by the use of digitally tunable capacitors (DTCs) [77]. PIN diodes can be modeled as current-controlled resistors at radio frequencies, and two of them accessed with a Q-splitting network, shown in Figure 12(a), can realize a wide range of complex reflection coefficients. In addition to the cost of the two DACs required to set the currents, this architecture has the issue of noise current generated by the PIN diode resistance modulating the resistance itself, thereby modulating the incident coupled TX signal [76] such that significant noise can occur at the tag BLF. To avoid this problem, a relatively new class of component, the DTC, was used to implement the TMN in the circuit shown in Figure 12(b)

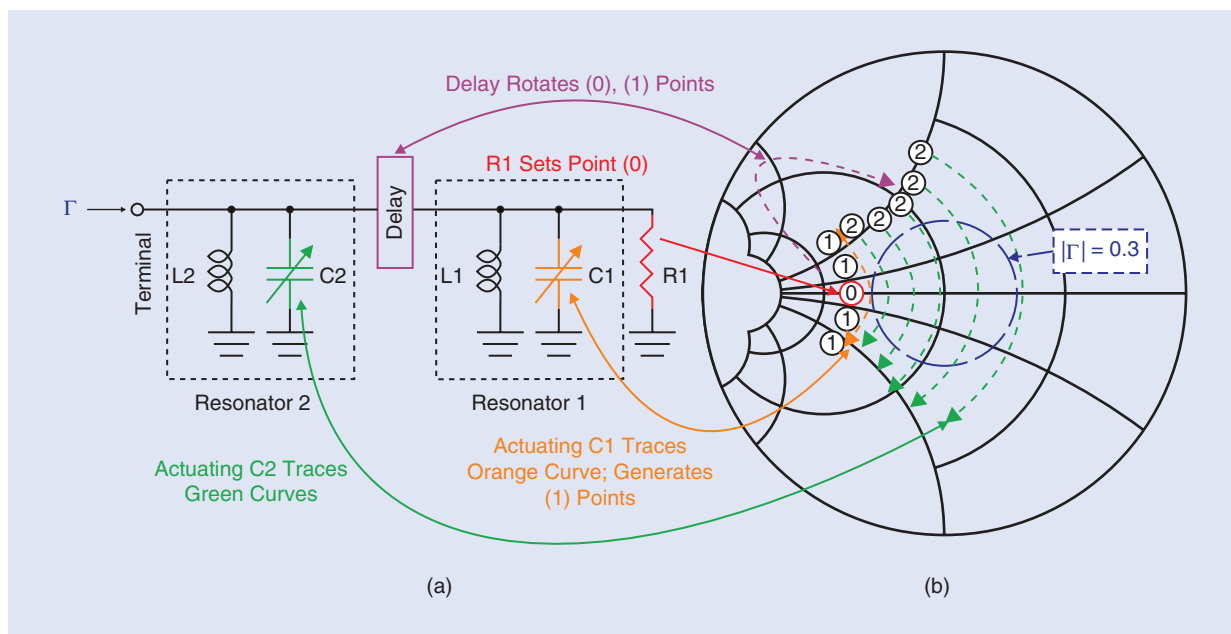


Figure 13. (a) A shunt-shunt coupled resonator network. (b) The coverage of the TMN specification area. Modified from [65, Figs. 2 and 3].

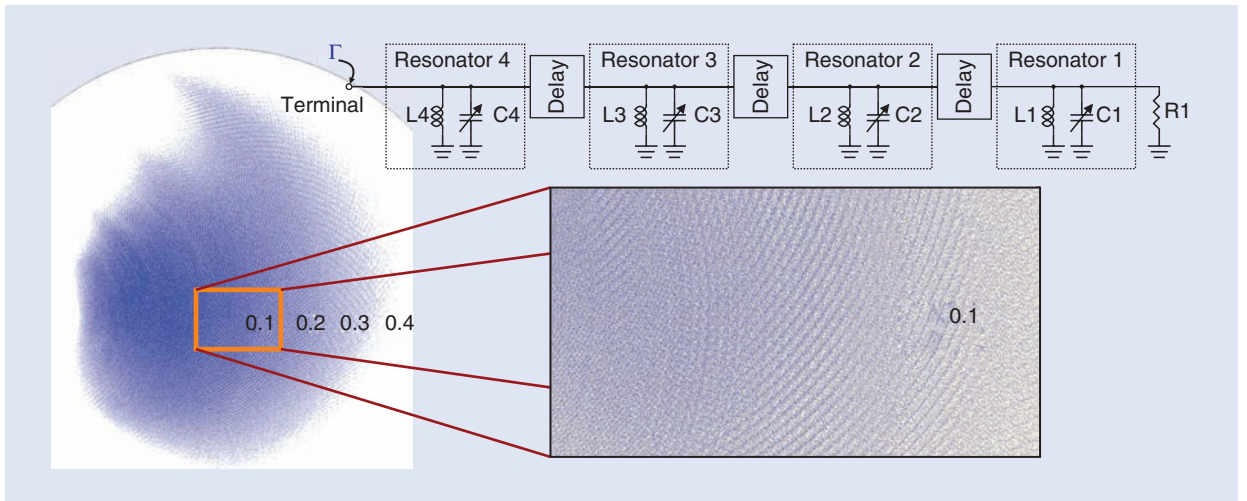


Figure 14. An initial attempt at increasing the TMN resolution: four cascaded resonator stages and the simulated coverage results. Modified from [65, Fig. 4].

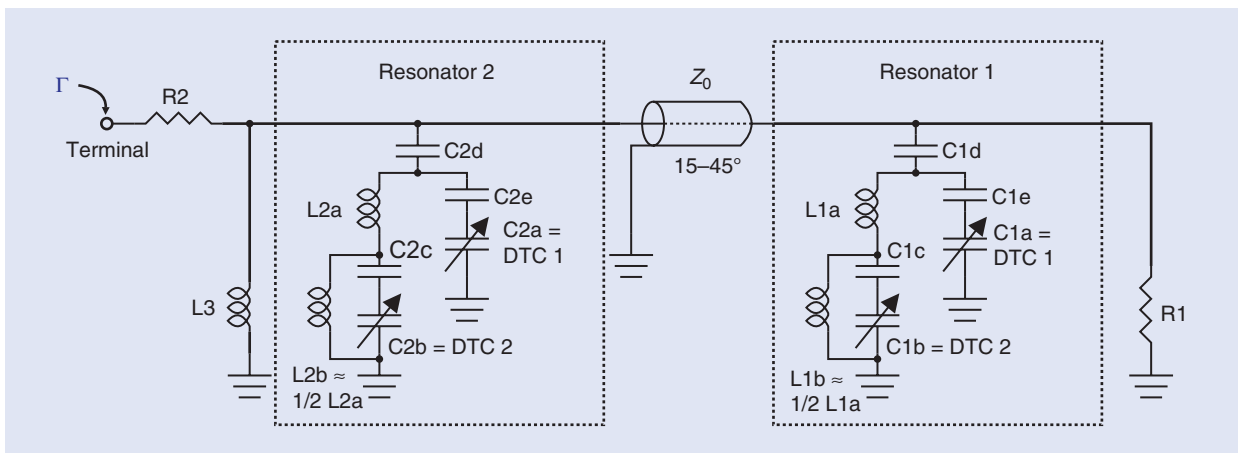


Figure 15. The proposed subbranching DTC-based TMN. Modified from [65, Fig. 5].

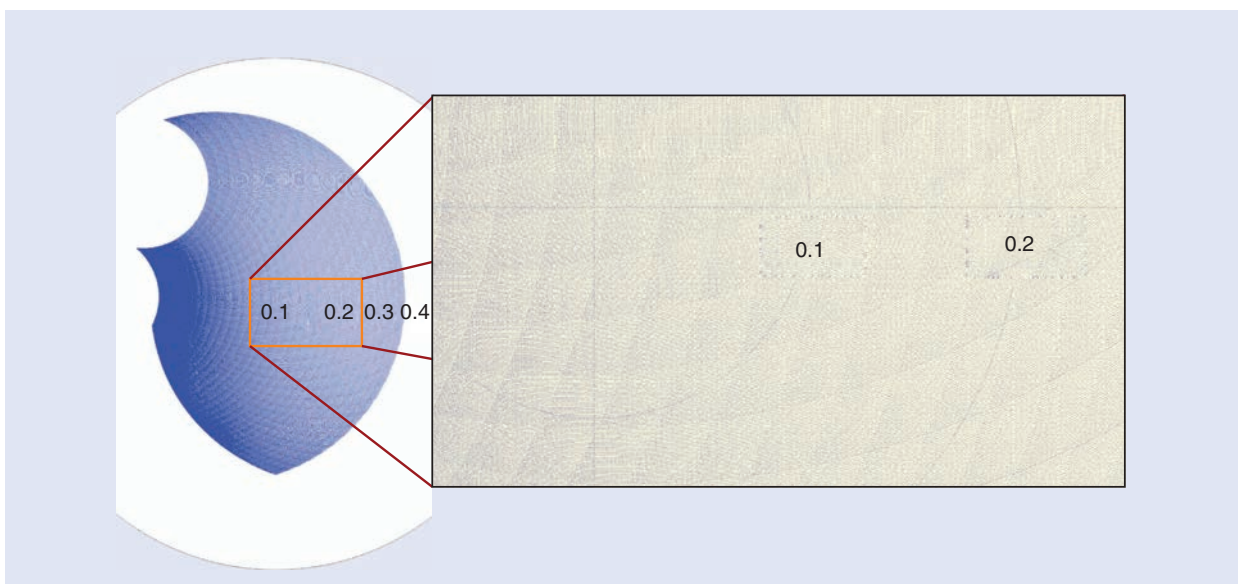


Figure 16. The simulation results for the proposed subbranching TMN reflection coefficient coverage. Modified from [65, Fig. 7].

[77]. DTCs are largely noiseless, they handle watt-level power, and, most importantly for our purposes, they are publicly available on the cheap, currently selling for less than US\$0.60 in quantities of 6,000 or more. The downside of currently available DTCs is that they have limited resolution. At about 5 bits apiece, a two-DTC network, such as the one in [77], is only enough to practically achieve only about 20 dB of added TX-to-RX leakage isolation.

Designing a TMN

For any RPC-based TX leakage cancellation circuit, the rough objective is to design a TMN that can minimize the distance of any possible $-\Gamma_{ANT}$ to a realizable reflection coefficient Γ_{TMN} . For the standard case in which a low-cost antenna's reflection coefficient is constrained to be less than -10 dB across the range of frequency operation, the specification area to be covered is a circle with a radius approximately equal to 0.3, centered at the middle of a Smith chart, as in Figure 13(b). A coupled resonator network, illustrated in Figure 13(a) [78], was originally proposed for matching a mobile phone's power amplifier (PA) to its antenna. With correctly chosen component values, such a network with a 25- Ω seed impedance R1 covers the target area of the Smith chart, as depicted in Figure 13(b). Although a successful blanketing of the target area was achieved, the problem of limited TMN resolution still remains.

Clearly, more 5-bit DTCs must be added to the network to realize more Γ_{TMN} in the target circle since doing so permits greater TX-to-RX isolation. One conceptually simple way to do this would be to couple

more resonators into the network. This can be made to work from a coverage standpoint, as detailed in Figure 14; however, manipulating the four resulting state variables will be computationally expensive for the tuning algorithm. Also, the point coverage of the target area is uneven, leading to wide-open areas that result in larger than necessary maximum cancellation errors. A preferable approach is introduced in [65] and shown in Figure 15, in which the inductors of the shunt resonators in the original two-resonator network are modified to act as tapped impedance dividers to yet another set of DTCs. If the inductive division is appropriately chosen, a Zobel transformation [79] can be applied to the network to show that the newly added DTCs serve as subranging programmable capacitors. Now, not only is the number of states increased to 1,048,576, but this

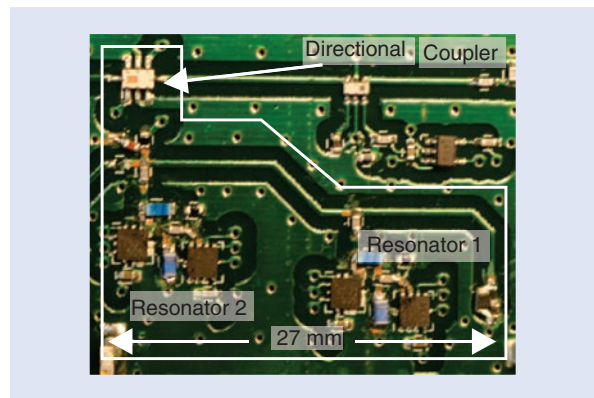


Figure 17. The implemented and tested RPC. Modified from [65, Fig. 11].

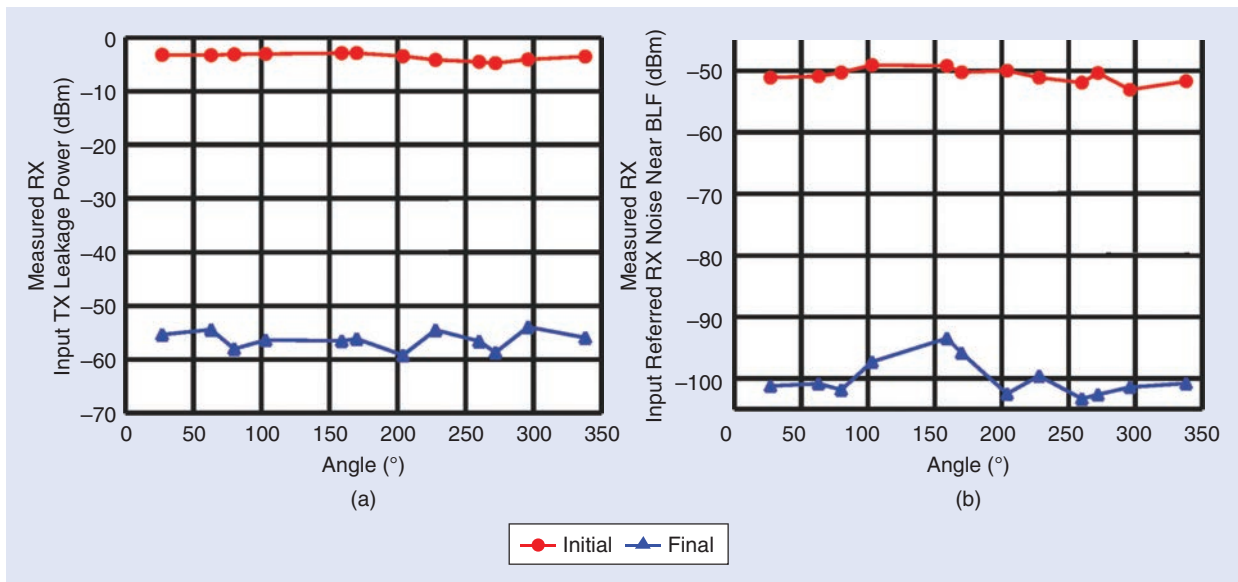


Figure 18. The measurement results for the TX leakage cancellation network described in [65]. (a) The measured TX leakage referred to the SDR ASIC RX input. (b) The measured noise at the data recovery circuit referred to the SDR ASIC RX input. Modified from [65, Figs. 9 and 13].

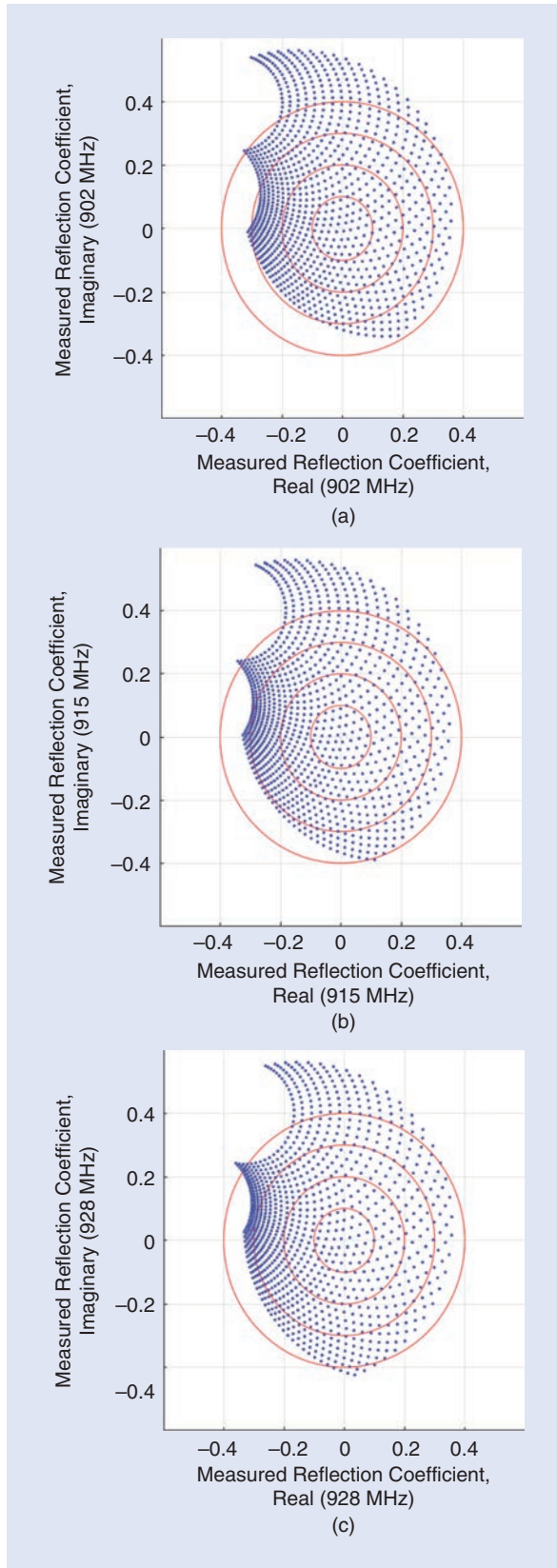


Figure 19. The measured Smith chart coverage results across the U.S. 900-MHz license-free band. (a) 902 MHz. (b) 915 MHz. (c) 928 MHz. Modified from [65, Fig. 12].

is done without increasing the number of state variables. The worst-case cancellation ratio was, indeed, confirmed to rise from 20 to 50 dB via computational analysis, while the coverage characteristics can be seen to be quite uniform locally in Figure 16.

Tuning Algorithm and Measured Results

The final RPC circuit implemented for the reader described in [20] and [65] is displayed in Figure 17. The cost of the four DTCs is US\$2.30 in quantities of 15,000. The directional coupler cost US\$0.46 but would have been needed anyway. High-quality inductors (the blue components in Figure 17) were used for first-pass success, at a bulk cost of US\$0.67 for all four. Since it is clear that the network can be quite lossy, much cheaper low-quality inductors can be used in future iterations. The TMN is driven by a gradient-descent algorithm in the reader FPGA, which uses as its cost-minimization function an estimate of the TX leakage RF magnitude derived from complex baseband data. This algorithm addresses a number of practical considerations in the SDR ASIC and TMN design and is described in more detail in [65].

The canceller circuit and algorithm were tested using a set of dummy loads at the antenna port, with $|S_{11}| \approx -11$ dB and 12 random $\angle(S_{11})$ with a TX output power of +26 dBm. While the suppression of the transmitter leakage, given in Figure 18(a), is roughly as expected, at more than 49 dB for all angles, what really matters is the suppression of input-referred phase noise since this is the signal that actually corrupts the back-scattered tag response. As shown in Figure 18(b), this is improved by more than 48 dB for all but two points, for which it is improved by more than 44 dB. From this latter plot, after adding 19 dB to refer SDR ASIC-input-referred noise quantities back to the antenna, we can compute for the more typical angle results:

$$\begin{aligned} FOM_R &= P_{TX,ANT}(\text{dB}) - P_{N,ANT}(\text{dB}) - IS_{ANT}(\text{dB}) \\ &= 26 \text{ dBm} - (-81 \text{ dBm}) - 11 \text{ dB} = 96 \text{ dB}. \end{aligned} \quad (6)$$

Coarse TMN coverage measurement results appear in Figure 19. The Smith chart coverage pattern is consistent with simulation and varies little across the U.S. 900-MHz license-free band. More measurement results and test details for this circuit are provided in [65].

Low-Cost Software-Defined UHF RFID Readers

Top-Level Architecture

In keeping with our goal of developing a tool for many people to use to explore UHF RFID, we endeavor to design a UHF RFID reader by selecting components that are as cheap as possible, integrate as much

programmable functionality as possible, and come with data sheets and other application information that are as comprehensive as possible. Flowing from all these considerations is the reader architecture in Figure 20 [20], which also shows the pricing of key components.

The SDR chip is the Semtech SX1257. At the time this project was initiated, this was the lowest-cost publicly accessible SDR ASIC that allowed access to its raw base-band (I/Q) data and permitted full duplex radio operation. Ideally, the SDR ASIC would include features such as those described in [70] to promote TX leakage cancellation, but sadly this one does not. The FPGA is the Altera (now Intel) 10M02 with 2,304 logic elements. One of the primary challenges of this project was fitting an

entire UHF RFID digital back end and TMN controller into such a small FPGA resource count. The TX leakage cancellation is accomplished by the reflective power canceller featuring the subranging DTC-based TMN described previously.

Together, these three subsystems, at US\$9.04, replace one of the publicly accessible reader ASICs available on major distributor websites. The cheapest of these, the ST25RU3980, currently sells for US\$21.60, in bulk; does not have a publicly accessible full data sheet (only a “datashort”); can execute a single tag read only every 500 ms [80]; is currently scheduled for obsolescence; and still requires an external structure to provide TX leakage cancellation for a reader output power of +26 dBm and

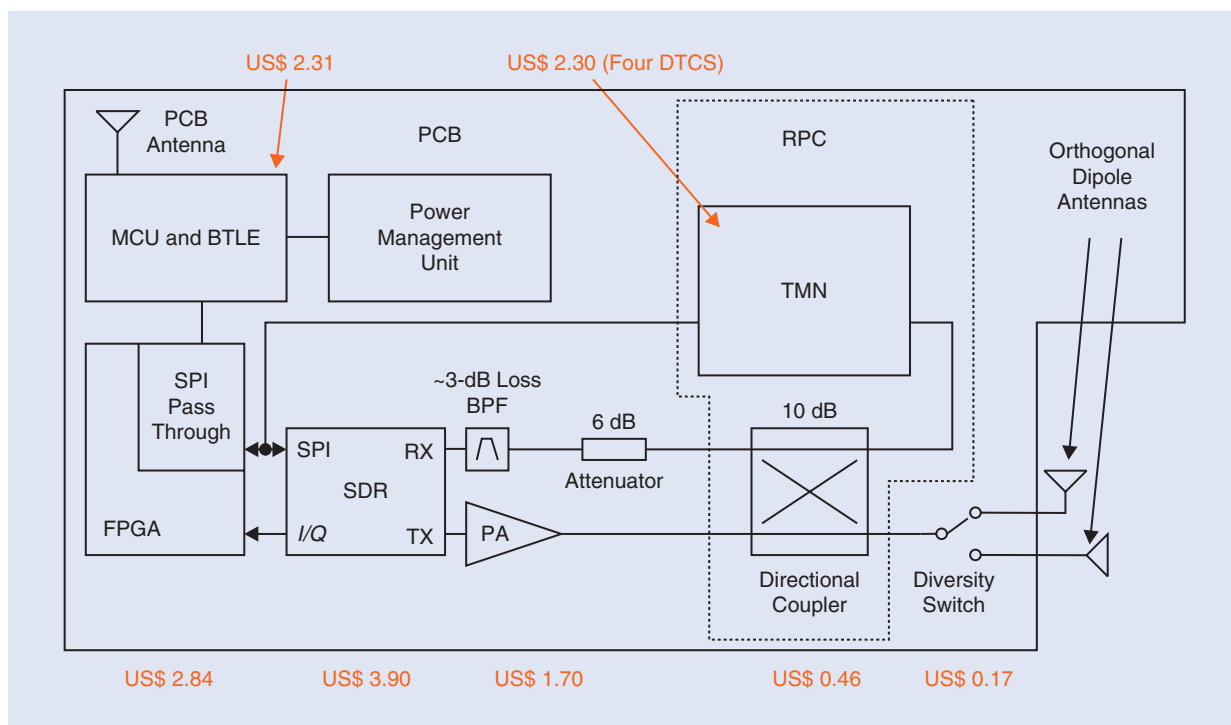


Figure 20. The proposed UHF RFID reader's top-level block diagram, including current publicly available bulk-pricing information. Modified from [20, Fig. 1].

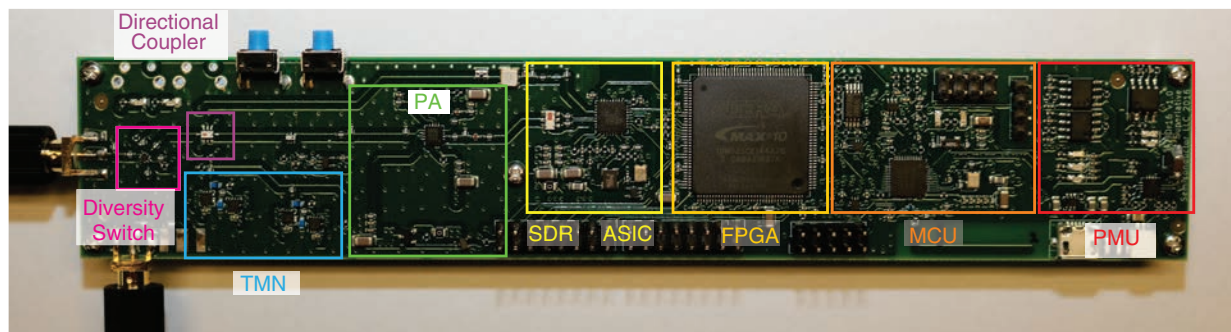


Figure 21. The implemented reader, with key subsections highlighted. PMU: power management unit. Modified from [20, Fig. 8].

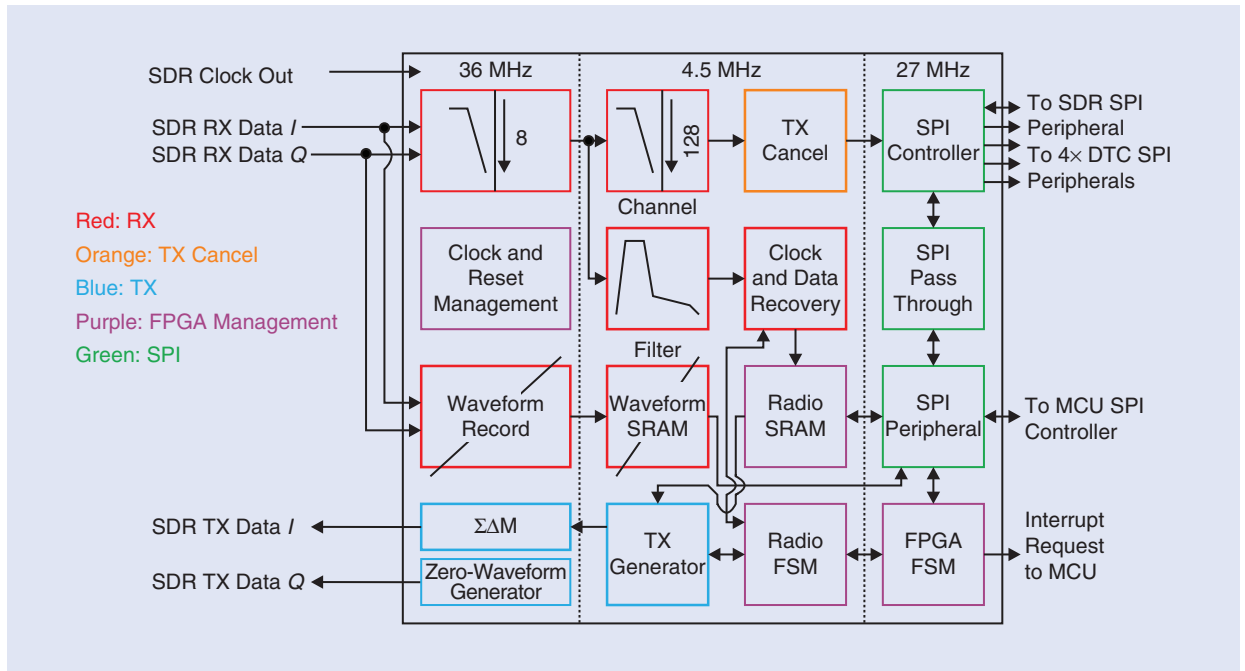


Figure 22. The top-level architecture of the reader FPGA digital design. Crossed-out blocks are those currently disabled to permit fitting the design in the FPGA. FSM: finite-state machine; $\Sigma\Delta$ M: sigma-delta modulator; SRAM: static random-access memory. Modified from [20, Fig. 3].

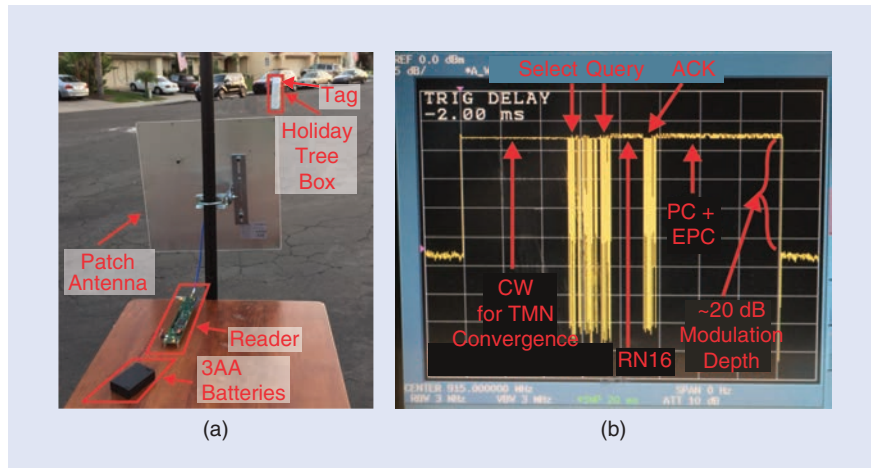


Figure 23. The reader range test setup and over-the-air RFID traffic capture. (a) The reader range measurement setup. (b) The measured reader TX waveform showing a ≈ 20 -dB modulation depth and backscatter response. From left to right, a continuous wave (CW) signal is transmitted for TMN convergence; Select and Query EPC Gen 2 commands are transmitted by the reader; the tag backscatters a 16-b random number EPC Gen 2 response; the reader transmits an ACK command; and the tag backscatters its protocol control (PC) and EPC bits. Modified from [20, Fig. 9].

an antenna $|S_{11}| \approx -10$ dB, given a 1 dB-compression point of +7 dBm [81].

Intelligence is implemented on the proposed reader in a Nordic Semiconductor NRF51822 combined MCU + BTLE ASIC. In addition to extensive publicly accessible documentation and software development kits for its

ASIC, Nordic will even tell you how to use the free Eclipse firm-ware integrated development environment with its chips and tool kit [82]. The MCU controls the FPGA and sets control registers on the SDR ASIC through a serial peripheral interface (SPI) bridge on the FPGA. The FPGA accepts and provides 1-b baseband I/Q data to and from the SDR ASIC, which converts said bitstreams to and from the over-the-air radio wave-forms within the 900-MHz U.S. license-free band. The PA amplifies the SDR output up to roughly 1 W, and the RX BPF removes any interfer-ers from outside the 900-MHz band, while the 6-dB attenua-tor ensures that the maximum TX leakage does not damage

the SDR ASIC RX input. Diversity antenna ports and a switch to commutate between them provide access to RFID tags of different polarizations in the local environment. The implemented reader, shown in Fig-ure 21, is assembled on a four-layer PCB that measures 7.4×1.3 in.

FPGA

The SDR aspect of the reader consists of two devices: the FPGA and the MCU. While the FPGA is often thought of as “hardware,” it is programmed with code and can, in principle, be reflashed over the air through the MCU and hence can accurately be claimed as “software defined.” Given the current state of low-cost ASIC technology, the software-defined UHF RFID reader cannot be implemented using an MCU alone. Most affordable MCUs with a moderate power dissipation feature a maximum clock rate of a few hundred megahertz. While a few operations may be parallelized on some MCUs, the UHF RFID digital back end requires dozens of arithmetic operations running at the frequency of the SDR ASIC (in this case, 36 MHz), not to mention the hundreds running at somewhat lower rates. A power- and cost-competitive MCU capable of handling this task on its own does not currently exist, but this sort of signal processing burden is easily handled by an FPGA.

The top level of the FPGA internal logic design is described in Figure 22. Connections to the SDR signal path are on the left, while input and output control connections are on the right of Figure 22. The FPGA unburdens the MCU by enabling the MCU to load the FPGA's static random-access memories with various commands and TX waveform data prior to an RFID radio operation and to extract RX waveform data when the operation is done. During radio operations, which require low latency, the MCU hands off control of the system to the FPGA's finite-state machines. Clock domain partitioning was critical to meet the data rate requirements of the SDR ASIC (36 MHz), the requirement to interface across SPI buses as quickly as possible (27 MHz), and the need to keep the bulk of the signal processing circuitry operating at a data rate as low as possible (4.5 MHz) to ease the timing closure and maximize the utilization of the FPGA resources.

Why not set the minimum clock rate even lower? In general, most of the blocks in this clock domain have some implicit requirement to be running at approximately 4.5 MHz. For example, the minimum clock rate dictates the time resolution of the waveforms that the TX baseband waveform generator can create. Too slow, and the generated waveforms don't meet the EPC Gen 2 TX timing requirements. Another example is the clock recovery circuit. For it to provide a meaningful approximation to its continuous-time inspiration, it needs to be running at an oversampling ratio of at least 10. With the tag BLF at 187.5 kHz, the “data” rate handled by the clock recovery circuit is 375 kHz, requiring a clock rate of greater than about 3.75 MHz. More details of the various subblocks used in the FPGA can be found in [20].

With such a reader, we expect the barrier to entry for experimenting with UHF RFID at long ranges to fall considerably.

Measured Results

The line-of-sight outdoor range of the reader was measured in a street setting, shown in Figure 23(a), and found to be 2.6 m for a half-wave dipole antenna and 15.2 m for a 12.5-dBi patch antenna before the tag read rate dropped below 50%. The read range was less than the ideal number predicted in Figure 6, due to an increase in the receiver noise floor during operation when an antenna was attached to the reader. Tones in the measured phase noise spectrum suggest that this increase is due to coupling from the antenna into the SDR ASIC, but the noise may also be due to delayed TX reflections from objects in the environment. More results and testing details regarding the reader are covered in [20].

Conclusions

In this article, we've shown how to analyze and tackle many of the challenges associated with building a low-cost software-defined UHF RFID reader. We've discussed the essential requirements in terms of leakage cancellation and its impact on receiver noise and shown the benefit of high gain, well-isolated reader antennas along with a survey of the same in the context of an antenna FOM. Following this, we presented a survey of low-cost leakage canceller circuits and delved into some of the details of building the reader hardware, supporting the discussion with measured results of an implemented low-cost reader and its integrated RPC circuit.

With such a reader, we expect the barrier to entry for experimenting with UHF RFID at long ranges to fall considerably, making it easier for the community at large to hunt for the killer UHF RFID app. Of course, we don't expect the readers of this article to develop all the hardware described herein from scratch. That is why, in conjunction with the publication of this article, we are open-sourcing the reader project, with the source and licensing materials located at www.openrfidreader.net. It is our hope that the community of electrical engineers, hobbyists, tinkerers, and students finds this to be an exciting, educational, and perhaps even profitable project through which it can computationally interact with the objects in the surrounding world.

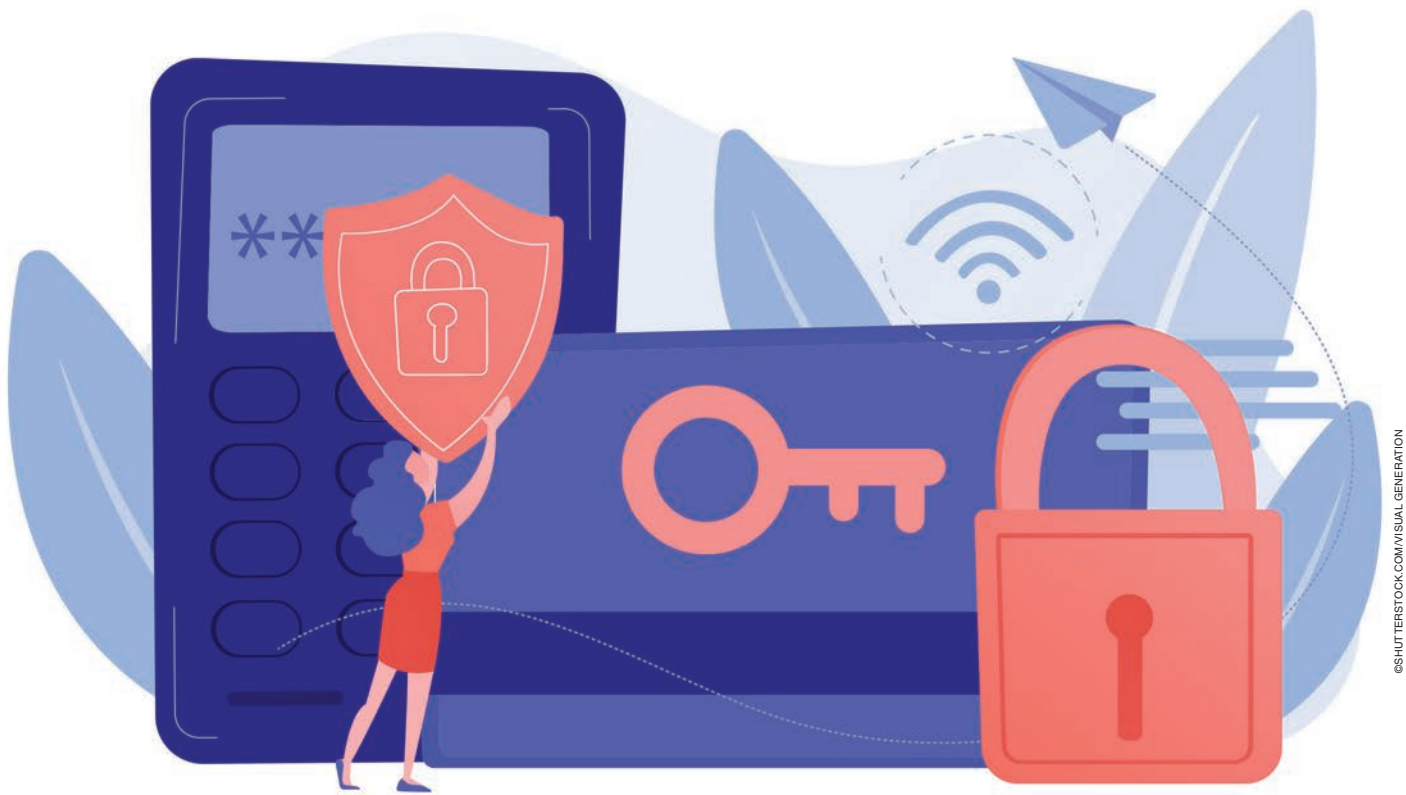
References

- [1] “EPC radio-frequency identity protocols generation-2 UHF RFID: Specification for air interface protocol for communications at 860MHz - 960MHz version 2.0.1 ratified,” 2015. [Online].

- Available: https://www.gs1.org/sites/default/files/docs/epc/Gen2_Protocol_Standard.pdf
- [2] R. Bhattacharyya, C. Floerkemeier, and S. Sarma, "Low-cost, ubiquitous RFID-tag-antenna-based sensing," *Proc. IEEE*, vol. 98, no. 9, pp. 1593–1600, Sept. 2010. doi: 10.1109/PROC.2010.2051790.
 - [3] J. Melià-Seguí and X. Vilajosana, "Ubiquitous moisture sensing in automaker industry based on standard UHF RFID tags," in *Proc. IEEE Int. Conf. RFID*, Apr. 2019, pp. 1–4. doi: 10.1109/RFID.2019.8719092.
 - [4] C. R. Schoenberger. "The Internet of Things." *Forbes*. Mar. 2002. <https://www.forbes.com/global/2002/0318/092.html>.
 - [5] A. Bednarz. "RFID everywhere: From amusement parks to blood supplies." *Network World*. May 2004. <https://www.networkworld.com/article/2333045/rfid-everywhere--from-amusement-parks-to-blood-supplies.html>
 - [6] R. Want, "RFID: A key to automate everything," *Sci. Amer.*, vol. 290, no. 1, pp. 56–65, Jan. 2004. doi: 10.1038/scientificamerican0104-56.
 - [7] M. Malone. "Did Wal-Mart love RFID to death?" *ZDNet*. Feb. 2012. <https://www.zdnet.com/article/did-wal-mart-love-rfid-to-death/>
 - [8] S. Garfinkel, "An RFID bill of rights," *MIT Tech. Rev.*, vol. 105, p. 35, Oct. 2002.
 - [9] Wired Staff, "RFID: Sign of the (end) times?" *Wired*, vol. 105, pp. 1593–1600, Mar. 2006.
 - [10] D. Friedlos. "Australia's Woolworths supermarket chain studies RFID." *RFID Journal*. Oct. 2008. <https://www.rfidjournal.com/australias-woolworths-supermarket-chain-studies-rfid> (accessed Sept. 17, 2020).
 - [11] X. He. "Will Amazon Go win the war between computer vision and RFID in retail?" *IDTechEx Research*. Jan. 2017. <https://www.idtechex.com/en/research-article/will-amazon-go-win-the-war-between-computer-vision-and-rfid-in-retail/10463>
 - [12] D. A. Kaplan. "The rise, fall, and return of RFID." *Supply Chain Dive*. Aug. 2018. <https://www.supplychaindive.com/news/RFID-rise-fall-and-return-retail/530608/>
 - [13] The Build Network Staff. "6 lessons on innovation from the history of the barcode." *Inc*. Jan. 2014. <https://www.inc.com/the-build-network/6-lessons-on-innovation-from-the-history-of-the-barcode.html>
 - [14] C. Anderson, *Makers: The New Industrial Revolution*, 1st ed. New York: Crown Business, 2012.
 - [15] M. Hatch, *The Maker Movement Manifesto*, 1st ed. New York: McGraw Hill, 2014.
 - [16] A. Sample, D. Yeager, P. Powledge, A. Mamishev, and J. Smith, "Design of an RFID-based battery-free programmable sensing platform," *IEEE Trans. Instrum. Meas.*, vol. 57, no. 11, pp. 2608–2615, Nov. 2008. doi: 10.1109/TIM.2008.925019.
 - [17] S. Thomas, "RFID for everyone: Design of an easily-accessible, experimental, UHF RFID platform," in *Proc. IEEE Int. Conf. RFID*, Apr. 2019, pp. 1–4. doi: 10.1109/RFID.2019.8719280.
 - [18] J. Kimionis et al., "Design and implementation of RFID systems with software defined radio," in *Proc. 6th Euro. Conf. Antennas Propag.*, Mar. 2012, pp. 3464–3468. doi: 10.1109/EuCAP.2012.6206487.
 - [19] A. Briand et al., "Complete software defined RFID system using GNU radio," in *Proc. IEEE Int. Conf. RFID-TA*, Nov. 2012, pp. 287–291. doi: 10.1109/RFID-TA.2012.6404531.
 - [20] E. A. Keehr, "A low-cost software-defined UHF RFID reader with active transmit leakage cancellation," in *Proc. IEEE Int. Conf. RFID*, Apr. 2018, pp. 1–8. doi: 10.1109/RFID.2018.8376193.
 - [21] N. Roy et al., "Designing an FPGA-based RFID reader," *Xcell J.*, vol. 2, no. 26, pp. 26–29, 2006.
 - [22] C. Huang et al., "A new architecture of UHF RFID digital receiver for SoC implementation," in *Proc. IEEE Wireless Commun. Netw. Conf.*, Mar. 2007, pp. 1659–1663. doi: 10.1109/WCNC.2007.312.
 - [23] C. Angerer et al., "A flexible dual frequency testbed for RFID," in *Proc. 4th Int. Conf. Testbeds Res. Infrastructures Dev. Communities*, Mar. 2008, pp. 3:1–3:6.
 - [24] C. Angerer et al., "Advanced synchronization and decoding in RFID reader receivers," in *Proc. IEEE Radio Wireless Symp.*, Jan. 2009, pp. 59–62. doi: 10.1109/RWS.2009.4957284.
 - [25] R. Langwieser et al., "A modular UHF reader frontend for a flexible RFID testbed," in *Proc. 2nd Int. EURASIP Workshop RFID Tech.*, July 2008, pp. 1–12.
 - [26] M. Buettner and D. Wetherall, "A flexible software radio transceiver for UHF RFID experimentation," *Univ. of Washington, Tech. Rep. UW-CSE-09-10-02*, Oct. 2009.
 - [27] G. Smietanka et al., "Implementation and extension of a GNU-Radio RFID reader," *Adv. Radio Sci.*, vol. 11, pp. 107–111, July 2013. doi: 10.5194/ars-11-107-2013.
 - [28] L. Catarinucci et al., "A cost-effective SDR platform for performance characterization of RFID tags," *IEEE Trans. Inst. Meas.*, vol. 61, no. 4, pp. 903–910, Apr. 2012. doi: 10.1109/TIM.2011.2174899.
 - [29] C. S. Yoon et al., "A design of UHF-band RFID reader using FPGA," *ResearchGate*, pp. 1–4, Nov. 2014. [Online]. Available: https://www.researchgate.net/publication/267709838_A_Design_of_UHF-band_RFID_reader_using_FPGA
 - [30] C. Jin et al., "A robust baseband demodulator for ISO 18000-6C RFID reader systems," *Int. J. Dist. Sens. Netw.*, vol. 2012, pp. 1–12, July 2012.
 - [31] P. Nikitin et al., "Simple low cost UHF RFID reader," in *Proc. IEEE Int. Conf. RFID*, Apr. 2013, pp. 126–127.
 - [32] A. Borisenko, M. Bolic, and M. Rostamian, "Intercepting UHF RFID signals through synchronous detection," *EURASIP J. Wireless Commun. Netw.*, vol. 2013, pp. 1–10, Aug. 2013. Art. no. 216.
 - [33] N. Kargas et al., "Fully-coherent reader with commodity SDR for Gen2 FM0 and computational RFID," *IEEE Wireless Comp. Lett.*, vol. 4, no. 6, pp. 617–620, Dec. 2015. doi: 10.1109/LWC.2015.2475749.
 - [34] F. Galler, T. Faseth, and H. Arthaber, "SDR based EPC UHF RFID reader DS-SS localization testbed," in *Proc. IEEE Wireless Microw. Technol. Conf. (WAMICON)*, Apr. 2015, pp. 1–4. doi: 10.1109/WAMICON.2015.7120382.
 - [35] F. Galler, T. Faseth, and H. Arthaber, "Implementation aspects of an SDR based EPC RFID reader testbed," in *Proc. Int. EURASIP Workshop RFID Tech.*, Oct. 2015, pp. 94–97. doi: 10.1109/EURFID.2015.7332391.
 - [36] L. Gortschacher et al., "SDR based RFID reader for passive tag localization using phase difference of arrival techniques," in *Proc. IEEE MTT-S Int. Mic. Symp.*, May 2016, pp. 1–4. doi: 10.1109/MWSYM.2016.7538227.
 - [37] A. J. S. Boaventura et al., "The design of a high-performance multisine RFID reader," *IEEE Trans. Microw. Theory Tech.*, vol. 65, no. 9, pp. 3389–3400, Sept. 2017. doi: 10.1109/TMTT.2017.2663405.
 - [38] A. Boaventura, J. Santos, A. Oliveira, and N. B. Carvalho, "Perfect isolation: Dealing with self-jamming in passive RFID systems," *IEEE Microw. Mag.*, vol. 17, no. 11, pp. 20–39, 2016. doi: 10.1109/MMM.2016.2600942.
 - [39] M. Jain et al., "Practical, real-time, full duplex wireless," in *Proc. 17th Annu. Int. Conf. Mobile Comput. Netw.*, 2011, pp. 301–312. doi: 10.1145/2030613.2030647.
 - [40] P. V. Nikitin and K. Rao, "Performance limitations of passive UHF RFID systems," in *IEEE Antennas and Propagation Society Int. Symp.*, vol. 1011, 2006.
 - [41] J. D. Griffin and G. D. Durgin, "Complete link budgets for backscatter-radio and RFID systems," *IEEE Antennas Propag. Mag.*, vol. 51, no. 2, pp. 11–25, 2009. doi: 10.1109/MAP.2009.5162013.
 - [42] J. Rozman, M. Atanasijevic-Kunc, and V. Kunc, "Noise analysis of the UHF RFID system," *Anal. Integr. Circuits Signal Process.*, vol. 74, no. 3, pp. 591–598, 2013. doi: 10.1007/s10470-012-0015-5.
 - [43] Z. M. Bakir and H. M. AlSabbagh, "Limitations of forward and return links in UHF RFID with passive tags," *Int. J. Eng. Trends Tech.*, vol. 5, no. 5, pp. 238–242, Nov. 2013.
 - [44] "Electronic code of federal regulations, title 47, part 15 §15.247," U.S. Federal Government, Washington DC, Sept. 2019. [Online]. Available: https://www.ecfr.gov/cgi-bin/text-idx?SID=4ff7c519cffed4879d5effc595ee1fb7&mc=true&node=se47.1.15_1247&rgn=div8

- [45] H. Yoon and B.-J. Jang, "Link budget calculation for UHF RFID systems," *Microw. J.*, vol. 51, no. 12, pp. 64–74, Dec. 2008.
- [46] G. D. Durgin, C. R. Valenta, M. B. Akbar, M. M. Morys, B. R. Marshall, and Y. Lu, "Modulation and sensitivity limits for backscatter receivers," in *Proc. IEEE Int. Conf. RFID*, 2013, pp. 124–130. doi: 10.1109/RFID.2013.6548145.
- [47] G. Lasser and C. F. Mecklenbräuker, "Self-interference noise limitations of rfid readers," in *Proc. 2015 IEEE Int. Conf. on RFID (RFID)*, pp. 145–150. doi: 10.1109/RFID.2015.7113085.
- [48] G. De Vita and G. Iannaccone, "Design criteria for the RF section of UHF and microwave passive RFID transponders," *IEEE Trans. Microw. Theory Tech.*, vol. 53, no. 9, pp. 2978–2990, 2005. doi: 10.1109/TMTT.2005.854229.
- [49] J.-H. Bae et al., "Analysis of phase noise requirements on local oscillator for RFID system considering range correlation," in *Proc. 2007 European Radar Conf.* IEEE, pp. 385–388. doi: 10.1109/EURAD.2007.4405018.
- [50] "Monza 5 Tag Chip Datasheet," version 3.0., Impinj Inc., Aug. 2016.
- [51] R. Langwieser, C. Angerer, A. L. Scholtz, and M. Rupp, "Crosstalk and SNR measurements using a multi-antenna RFID reader with active carrier compensation," in *Proc. 3rd Int. EURASIP Workshop RFID Technol.*, 2010, pp. 66–69. [Online]. Available: https://publik.tuwien.ac.at/files/PubDat_187855.pdf.
- [52] NXP Semiconductors. "SL3S1204 UCODE7," rev. 3.3 ed., Dec. 2013.
- [53] L. W. Mayer and A. L. Scholtz, "Circularly polarized patch antenna with high Tx/Rx-separation," in *Proc. IEEE Int. Conf. RFID*, Orlando, Apr. 2009, pp. 213–216. doi: 10.1109/RFID.2009.4911200.
- [54] E. A. Etellisi, M. A. Elmansouri, and D. S. Filipovic, "Wideband monostatic simultaneous transmit and receive (STAR) antenna," *IEEE Trans. Antennas Propag.*, vol. 64, no. 1, pp. 6–15, 2015. doi: 10.1109/TAP.2015.2497356.
- [55] W.-G. Lim, W.-I. Son, K. S. Oh, W.-K. Kim, and J.-W. Yu, "Compact integrated antenna with circulator for UHF RFID system," *IEEE Antennas Wireless Propag. Lett.*, vol. 7, pp. 673–675, 2008. doi: 10.1109/LAWP.2008.921348.
- [56] W.-G. Lim, S.-Y. Park, W.-I. Son, M.-Q. Lee, and J.-W. Yu, "RFID reader front-end having robust Tx leakage canceller for load variation," *IEEE Trans. Microw. Theory Tech.*, vol. 57, no. 5, pp. 1348–1355, 2009. doi: 10.1109/TMTT.2009.2017308.
- [57] S. Padhi, N. Karmakar, C. Law, and S. Aditya, "A dual polarized aperture coupled microstrip patch antenna with high isolation for RFID applications," in *IEEE Antennas Propag. Soc. Int. Symp. 2001 Dig. Held Conjunction, USNC/URSI Nat. Radio Sci. Meeting (Cat. No. 01CH37229)*, vol. 2, pp. 2–5. doi: 10.1109/APS.2001.959607.
- [58] S. Padhi, N. Karmakar, and C. Law, "Dual polarized reader antenna array for RFID application," in *IEEE Antennas Propag. Soc. Int. Symp. Dig. Held Conjunction, USNC/CNC/URSI North Amer. Radio Sci. Meeting (Cat. No. 03CH37450)*, vol. 4, 2003, pp. 265–268. doi: 10.1109/APS.2003.1220171.
- [59] J.-S. Kim, K.-H. Shin, S.-M. Park, W.-K. Choi, and N.-S. Seong, "Polarization and space diversity antenna using inverted-f antennas for RFID reader applications," *IEEE Antennas Wireless Propag. Lett.*, vol. 5, pp. 265–268, June 2006. doi: 10.1109/LAWP.2006.875892.
- [60] H.-W. Son, J.-N. Lee, and G.-Y. Choi, "Design of compact RFID reader antenna with high transmit/receive isolation," *Microw. Opt. Technol. Lett.*, vol. 48, no. 12, pp. 2478–2481, 2006. doi: 10.1002/mop.22017.
- [61] X.-Z. Lai, Z.-M. Xie, Q.-Q. Xie, and X.-L. Cen, "A dual circularly polarized RFID reader antenna with wideband isolation," *IEEE Antennas Wireless Propag. Lett.*, vol. 12, pp. 1630–1633, Dec. 2013. doi: 10.1109/LAWP.2013.2294173.
- [62] G. Lasser, R. Langwieser, and A. L. Scholtz, "Broadband suppression properties of active leaking carrier cancellers," in *Proc. IEEE Int. Conf. RFID*, Orlando, Apr. 2009, pp. 208–212. doi: 10.1109/RFID.2009.4911192.
- [63] "Indy® R2000 Reader Chip (IPJ-R2000)," rev. 1.3 ed., Impinj Inc., July 2012.
- [64] I. Mayordomo et al., "Implementation of an adaptive leakage cancellation control for passive UHF RFID readers," in *Proc. IEEE Int. Conf. RFID*, Apr. 2011, pp. 121–127. doi: 10.1109/RFID.2011.5764611.
- [65] E. A. Keehr, "A low-cost, high-speed, high resolution, adaptively tunable microwave network for an SDR UHF RFID reader reflected power canceller," in *Proc. IEEE Int. Conf. RFID*, Apr. 2018, pp. 1–8. doi: 10.1109/RFID.2018.8376194.
- [66] G. Lasser, R. Langwieser, and C. F. Mecklenbräuker, "Automatic leaking carrier canceller adjustment techniques," *EURASIP J. Embedded Syst.*, vol. 2013, p. 3, May 2013. doi: 10.1186/1687-3963-2013-8.
- [67] S. Maddio, A. Cidronali, and G. Manes, "Real-time adaptive transmitter leakage cancelling in 5.8-ghz full-duplex transceivers," *IEEE Trans. Microw. Theory Tech.*, vol. 63, no. 2, pp. 509–519, 2015. doi: 10.1109/TMTT.2014.2387841.
- [68] P. Pursula, M. Kiviranta, and H. Seppä, "UHF RFID reader with reflected power canceller," *IEEE Microw. Wireless Compon. Lett.*, vol. 19, no. 1, pp. 48–50, Jan. 2009. doi: 10.1109/LMWC.2008.2008607.
- [69] S. Kim, Y. Jeon, G. Noh, Y.-O. Park, I. Kim, and H. Shin, "A 2.59-GHz RF self-interference cancellation circuit with wide dynamic range for in-band full-duplex radio," in *Proc. 2016 IEEE MTT-S Int. Microw. Symp. (IMS)*, pp. 1–4. doi: 10.1109/MWSYM.2016.7540324.
- [70] S. Chiu et al., "A 900 MHz UHF RFID reader transceiver IC," *IEEE J. Solid-State Circuits*, vol. 42, no. 12, pp. 2822–2833, Dec. 2007. doi: 10.1109/JSSC.2007.908755.
- [71] J.-W. Jung et al., "TX leakage cancellation via a micro controller and high TX-to-RX isolations covering a UHF RFID frequency band of 908-914MHz," *IEEE Microw. Wireless Comp. Lett.*, vol. 18, no. 10, pp. 710–712, Oct. 2008. doi: 10.1109/LMWC.2008.2003487.
- [72] D. P. Villame et al., "Carrier suppression locked loop mechanism for UHF RFID readers," in *Proc. IEEE Int. Conf. RFID*, Apr. 2010, pp. 141–145. doi: 10.1109/RFID.2010.5467234.
- [73] K. Kapucu et al., "A fast active leakage cancellation method for UHF RFID readers," in *Proc. IEEE Int. Conf. RFID*, May 2017, pp. 182–186. doi: 10.1109/RFID.2017.7945606.
- [74] P. Beasley, A. Stove, B. J. Reits, and B. As, "Solving the problems of a single antenna frequency modulated CW radar," in *Proc. IEEE Radar Conf.*, 1990, pp. 391–395. doi: 10.1109/RADAR.1990.201197.
- [75] W.-K. Kim et al., "A passive circulator for RFID application with high isolation using a directional coupler," in *Proc. Euro. Microw. Conf.*, Sept. 2006, pp. 196–199. doi: 10.1109/EUMC.2006.281252.
- [76] T. Brauner and X. Zhao, "A novel carrier suppression method for RFID," *IEEE Mic. Wireless Comp. Lett.*, vol. 19, pp. 128–130, Mar. 2009. doi: 10.1109/LMWC.2009.2013676.
- [77] M. Koller and R. Kung, "Adaptive carrier suppression for UHF RFID using digitally tunable capacitors," in *Proc. Euro. Microw. Conf.*, Oct. 2013, pp. 943–946.
- [78] R. Whatley et al., "CMOS based tunable matching networks for cellular handset application," in *Proc. IEEE Intl. Micr. Symp.*, June 2011, pp. 1–4. doi: 10.1109/MWSYM.2011.5972913.
- [79] O. J. Zobel, "Theory and design of uniform and composite electric wave-filters," *Bell Sys. Tech. J.*, vol. 2, no. 1, pp. 1–46, Jan. 1923. doi: 10.1002/j.1538-7305.1923.tb00001.x.
- [80] "Gen2 - Save Power and Cost: AS3980 - Low Cost UHF Reader IC," ams AG, Dec. 2013.
- [81] "UHF RFID Single Chip Reader EPC Class1 Gen2," version 1-00 Short Datasheet, ams AG, July 2015.
- [82] "Development with GCC and eclipse." <https://devzone.nordicsemi.com/nordic/nordic-blog/b/blog/posts/development-with-gcc-and-eclipse> (accessed: Aug. 19, 2019).





©SHUTTERSTOCK.COM/VISUAL GENERATION

Software-Defined RFID Readers

*Georg Saxl, Lukas Görtschacher,
Thomas Ussmueller, and Jasmin Grosinger*

In recent years, RF identification (RFID) technology in the ultrahigh-frequency (UHF) range has become increasingly important in many applications, especially in the context of both the Internet of Things (IoT) and Industry 4.0. RFID is no longer simply a matter of identification; today, it is mainly concerned with recording data from the surrounding environment. As a result, researchers are

working on the integration of sensors (or even small actuators) in passive RFID transponders (tags) for a variety of different applications and also on the localization and tracking of RFID tags attached to various objects and machinery. Another key aspect in UHF RFID technologies is security, as the data transmitted may be confidential and should not be shared with third parties. For the fast verification of novel algorithms

Georg Saxl (georg.saxl@uibk.ac.at) and Thomas Ussmueller (thomas.ussmueller@uibk.ac.at) are with the Microelectronics and Implantable Systems Group, Department of Mechatronics, University of Innsbruck, Innsbruck, 6020, Austria. Lukas Görtschacher (lukas.goertschacher@tugraz.at) and Jasmin Grosinger (jasmin.grosinger@tugraz.at) are with the Institute of Microwave and Photonic Engineering, Graz University of Technology, Graz, 8010, Austria.

Digital Object Identifier 10.1109/MMM.2020.3042408

Date of current version: 3 February 2021

in localization and novel protocols for security, wireless testbeds allow swift verification of these designs under real-world or real-time conditions [1]. Wireless testbeds are widely used in research and require scalability, modularity, and extendibility of the hardware and software. These needs can be achieved by using software-defined radios (SDRs). In the case of UHF RFID, SDR-based RFID readers have been developed and used as wireless testbeds for enhancements in UHF RFID systems.

SDR-Based RFID Readers

The concept of SDRs was first introduced by Mitola in 1995 [2]; he proposed the creation of a radio that, by means of software, is fully adaptable in its operating frequency, bandwidth, and communication standard. As presented in [3], a well-designed architecture for SDRs should share available hardware resources and make use of tunable and software-programmable devices. The baseband signals are generated and upconverted by a dedicated signal processing hardware, converted into analog waveforms by a digital-to-analog converter (DAC), filtered by a bandpass filter

(BPF), and amplified by a power amplifier (PA) before passing through an RF switch to be radiated by the antenna. The signal received by the antenna is routed to a low-noise amplifier through the RF switch and a BPF and then is digitized by an analog-to-digital converter (ADC). Downconversion, demodulation, and decoding are accomplished through dedicated signal processing hardware. Much research effort is currently focused on realizing SDRs. In addition, the testing industry responded to this demand with several commercial products. In this article, we review existing work on SDR-based RFID readers, which are used as wireless testbeds to enhance UHF RFID systems, particularly in the field of secure communication and passive localization of RFID tags.

Table 1 presents a summary of the wireless UHF RFID testbeds used in research that exploit SDR-based RFID readers (listed by the years in which the testbeds were first published). It can be seen from the table that the majority of the testbeds developed thus far are based on commercially available SDRs while one of the testbeds relies on a custom-built software-defined RFID reader [4]. The key advantages of testbeds based

TABLE 1. A summary of wireless UHF RFID testbeds used in research (listed by the years that the testbeds were first published). All publications listed in the Reference column refer to the same testbed, detailing different aspects of it (e.g., testbed scope and antenna configuration).

Year	Reference	Hardware	Protocol	Scope	Antenna Configuration
2007	[4], [7]–[12]	MATLAB-controlled, custom-built rapid prototyping reader: DSP, FPGA, two DACs, two ADCs, high-frequency (HF)/UHF RF front ends	EPC Global HF Ver.2, ISO 15693, ISO 18000-6 C (Gen2)	Multitag recognition (collision avoidance), localization, active carrier compensation	Bistatic MIMO: two transmit (Tx) and two receive (Rx) antennas
2007	[13]	MATLAB-controlled NI PXI SDR platform, PA	ISO 18000-6 C (Gen2)	Tag performance	Bistatic
2009	[5], [14]	LabVIEW-controlled NI PXI SDR platform, PA, circulator	ISO 18000-6 C (Gen2), ISO 18000-6B	Tag performance	Monostatic
2009	[15]–[17]	GNU Radio-controlled NI USRP1 SDR with two RFX900 daughterboards	ISO 18000-6 C (Gen2)	Tag performance analysis	Bistatic
2012	[18]	GNU Radio-controlled NI USRP N-200 SDR, 5.8-GHz RF front end	—	Sensing	Bistatic
2015	[19]–[22]	Two MATLAB-controlled NI USRP-2922 SDRs with RF front-end modifications, custom FPGA firmware	ISO 18000-6 C (Gen2)	Localization	Monostatic, bistatic
2015	[23]	GNU Radio-controlled NI USRP N200 SDR with one RFX900 daughterboard	ISO 18000-6 C (Gen2)	Multitag recognition	Bistatic
2016	[24]–[28]	LabVIEW-controlled NI USRP-2942R SDR, switch matrix, PA		Localization, sensing	Bistatic SIMO/MIMO: 1/2 Tx and 2 Rx antennas
2018	[29]	LabVIEW-controlled NI PXIe SDR platform, circulator	ISO 18000-6 C (Gen2)	Secure protocols	Monostatic

SIMO: single input, multiple output; USRP: Universal Software Radio Peripheral.

on commercially available SDRs are their simplicity and flexibility and the fact that they are based on widely available hardware and software [5]. The key advantages of the testbed that relies on a custom-built RFID reader are its superior performance in terms of hardware and its proven ability to rapidly and automatically convert software into its reconfigurable components [i.e., field-programmable gate arrays (FPGAs) and digital signal processors (DSPs)], thus facilitating rapid prototyping [1]. The wireless UHF RFID testbeds listed in Table 1 focus mostly on the International Organization for Standardization/International Electrotechnical Commission (ISO/IEC) 18000-6 C standard, widely known as the *electronic product code (EPC)* class-1, generation-2 standard [6] (“Gen2” for short). Table 1 lists, in addition, the scope of each testbed as well as the respective antenna configuration used in the individual test setups [i.e., monostatic or bistatic configuration with or without multiple input, multiple output (MIMO) capabilities]. An RFID reader with a monostatic antenna configuration uses a single antenna for transmission and reception while an RFID reader with a bistatic antenna configuration uses two separate antennas for transmission and reception. In the following sections, we provide more insight into the latest two developments outlined in Table 1, which focus on UHF RFID system enhancements with respect to secure communication and localization of passive RFID tags.

Security Enhancements

The security of the air interface in UHF RFID systems is an essential factor due to its range of several meters. The interception or manipulation of private or confidential data by attackers must be prevented. In addition, the reading of a tag and, thus, access to the data should only be possible with valid authentication. This is especially important in the environments of IoT and

Industry 4.0 [30]. In companies as well as in private homes, it should not be possible for unauthorized parties to read information from machines and devices or, in the worst case scenario, to take control of them. To achieve the security standards needed, enhancements are required on both the reader and tag sides.

Secure Testbed

To implement crypto suites in UHF RFID test systems, we use the PXIe-1075, an SDR from National Instruments (NI) [31]. The detailed hardware setup of the UHF RFID reader is presented schematically in Figure 1.

On the basis of the eleven security services currently standardized in the ISO/IEC 19267 family (see “Overview of the ISO/IEC 29167 Crypto Suites”), we decided to implement the Rabin-Montgomery (RAMON) crypto suite. The RAMON algorithm is characterized by the fact that only very low computing power is required for encryption. Higher processing power and power consumption are, however, required for decryption. This algorithm is thus perfectly suited to UHF RFID systems since the encryption on the tag needs minimal power, whereas, on the reader side, sufficient power is available. RAMON is an asymmetric encryption method in which the public key n is used for encryption and two private keys, p and q , for decryption.

The basic sequence of encryption and decryption is displayed in Figure 2. The decryption has been implemented in the reader protocol using LabVIEW [32]. The decryption time, however, is about 28 s, exceeding the specified timings by far. This is due to the fact that LabVIEW is not able to efficiently handle large numbers such as private keys. Thus, a different approach is chosen.

To outsource the operations with the large numbers from LabVIEW, a Java application is programmed to take over all decoding functionalities. This Java application runs in parallel with LabVIEW on the PXIe controller and receives all of the data necessary for the decryption from the LabVIEW program via a TCP/IP socket. This includes the encrypted message c^* , the two private keys q and p , and the challenge interrogator (CHI). CHI is a random number generated by the reader that is, on the one hand, mixed with the message before encryption to reduce traceability and, on the other hand, used to select the

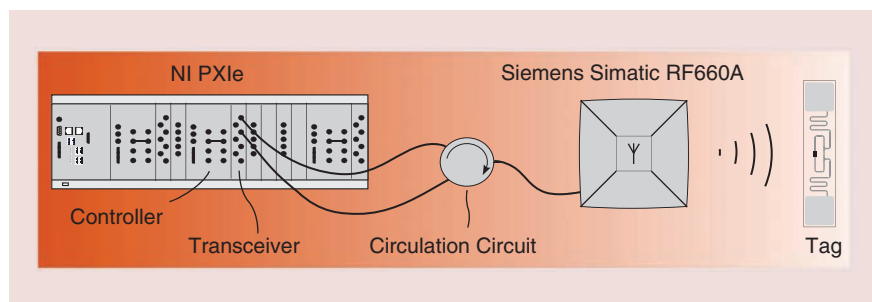


Figure 1. The hardware setup of the UHF RFID test system based on NI’s PXIe-1075 chassis: a PXIe-8135 control module and a PXIe-5644R transceiver module are utilized to implement the Gen2 protocol. For data capture, an antenna (Siemens Simatic RF660A) is connected to the transceiver via a circulation circuit to shield the outgoing signals from the incoming signals. A multitouch display (LG23ET83V) is used for the graphic evaluation of the data and communication with the controller. (Source: [29]; used with permission.)

correct message from the four solutions obtained after decryption. Once the Java application has completed the decryption, the decrypted plaintext message is sent back to the LabVIEW program via the socket for further processing. This entire procedure is visualized in Figure 3. This process drastically reduces the decryption time. In fact, after this process is completed, a decryption requires only about 1.3 ms on average, including the time for data transfers from LabVIEW to Java and back. Thus, it is possible to comply with the specified timings of the Gen2 protocol and obtain a fully functional reader with implemented RAMON decryption.

Secure Tags

This section reviews RFID tags that already provide security features (see Table 2). However, the majority of these tags are nonstandardized implementations or are implementations with standards that have either been withdrawn or are outdated. Only a few implementations deal with the current standard ISO/IEC 29167 [34], which defines the architecture of security services for the ISO/IEC 18000-6 C standard air interfaces in UHF RFID systems [35], [36].

Table 2 presents a selection of tags with implemented crypto suites, listed according to the years when the systems were first published. We compare the presented systems in terms of their basic encryption algorithm and, if applicable, the underlying standards. In addition, we compare the power consumption of the tag or crypto suite, the measurement setup [application-specific integrated circuit (ASIC), FPGA, or simulation], the semiconductor process used, and the required clock frequency. As can be seen, the most popular approach is an implementation of the crypto-engine Advanced Encryption Standard (AES) with a key length of 128 bits. While in [37]–[39] the authors do not follow an official standard, the algorithms in the works

[40]–[42] comply with previous versions of the EPC specification or an ISO/IEC standard. In comparison, implementations without standardization tend to work more slowly since no timing requirements need to be met. This explains the tendency toward lower power consumption as the number of clock cycles required and the clock frequency can be optimized freely.

In [43]–[45], the authors use other crypto engines, namely, the International Data Encryption Algorithm (IDEA), the Feistel cipher, and a self-developed algorithm based on a variable linear-feedback shift register. The very low power consumption of only 3.15 μW of the tag with the Feistel cipher is especially noteworthy. Such low power consumption can enable longer ranges and, thus, open up further applications, particularly when combined with passive UHF RFID tags. However, it is uncertain to what extent the Chinese

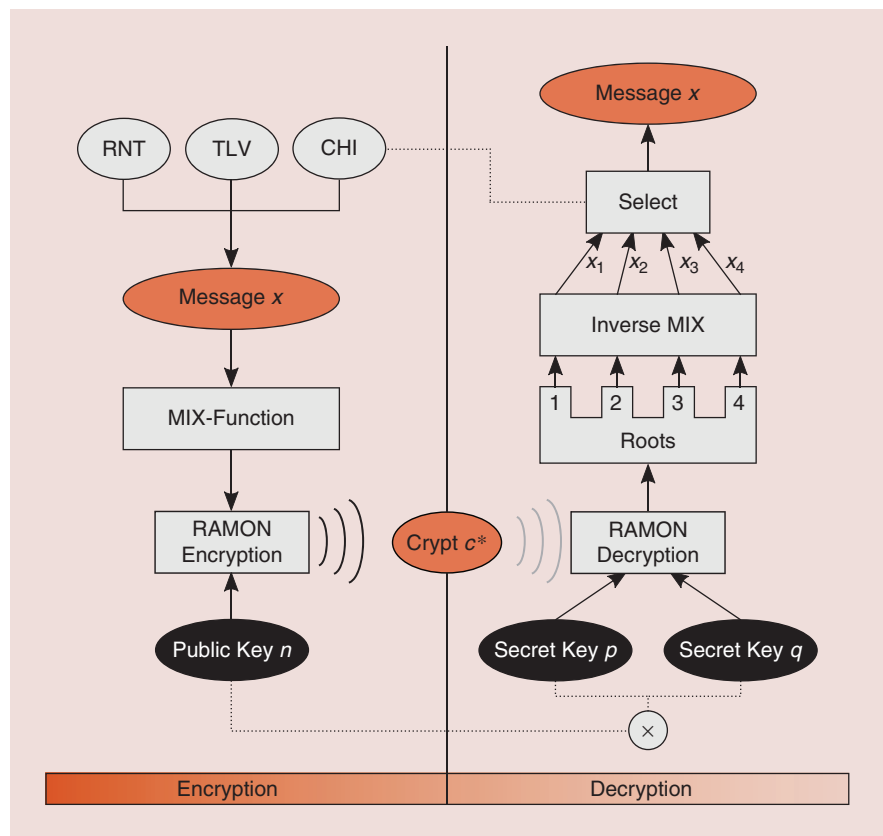


Figure 2. A schematic representation of the RAMON crypto system process: the message x to be encrypted is 128 bytes long and consists of a 16-byte random number (RNT, random number tag), 95 bytes of data (TLV, tag length value), a 16-byte CHI, and 1-byte of zero padding. This message is mixed according to a specific pattern (MIX function) to reduce traceability and thereby increase security. Next, the actual RAMON encryption is performed using the public key n . The result is the encrypted message c^* . For decryption, the two secret keys p and q are utilized. Due to roots in the decryption process, there are four different outputs. All four are inversely mixed according to a specific pattern. Finally, since CHI is known to the reader and the tag, it is possible to select the correct plain text message [32], [33].

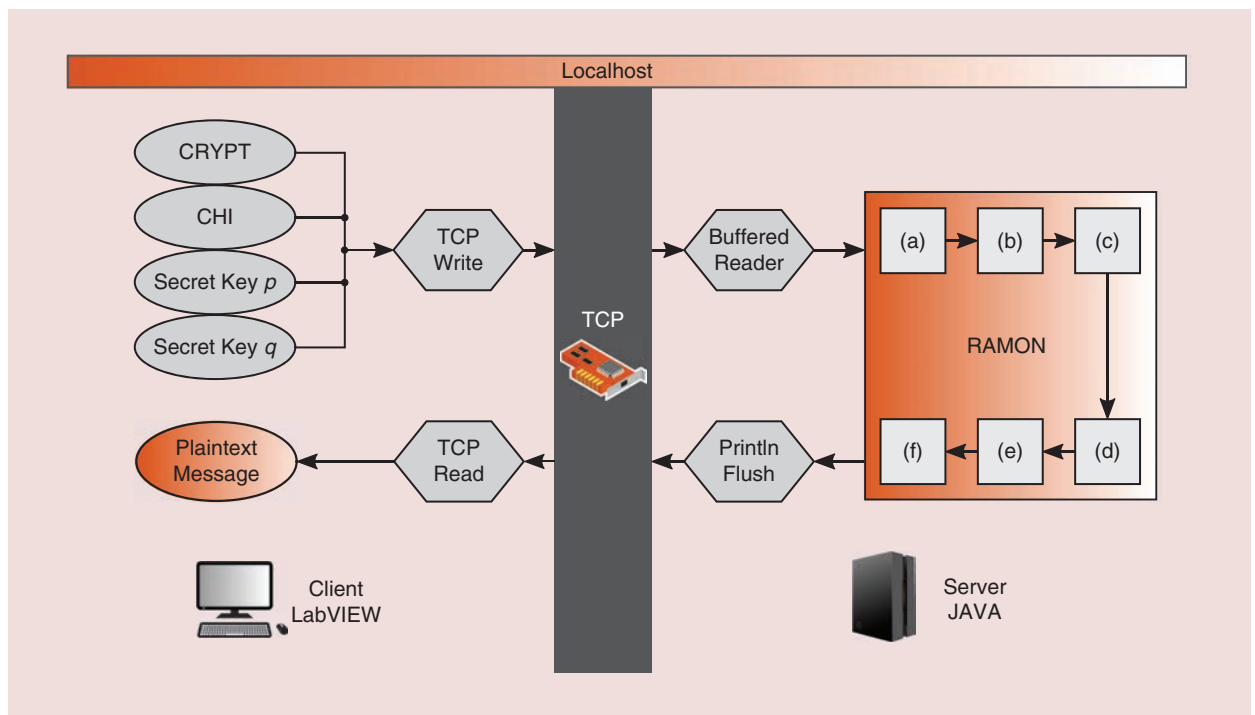


Figure 3. The encrypted message c^* (CRYPT), together with the private keys p and q as well as CHI, is transmitted to the Java application via a TCP/IP socket. There, the decryption is executed, and four solutions are produced. To select the correct plaintext message, the known CHI is compared with all four solutions. The plaintext message where the CHI matches is finally transmitted back to LabVIEW via the socket. (Source: [29]; used with permission.)

TABLE 2. A summary of RFID tags with implemented crypto engines (listed by the year of first publication).

Year	Reference	Crypto Engine	Protocol	Power Consumption	Measurement	Process	Clock Frequency
2005	[37]	AES-128	N/A	AES: 4.5 μ W	Yes (ASIC)	Philips 0.35 μ m	100 kHz
2007	[38]	AES-128	N/A	N/A	No (simulation)	Samsung 0.25 μ m	10 MHz
2007	[39]	AES-128	N/A	4.7 μ W	No (simulation)	TSMC 0.18 μ m	3.55 MHz
2010	[43]	IDEA	Gen2	8.96 μ W (IDEA: 2.21 μ W)	Yes (ASIC)	SMIC 0.18 μ m	1.28 MHz
2013	[40]	AES-128	Gen2	8.84 μ W (AES: 0.7 μ W)	Yes (ASIC)	Tower 0.18 μ m	1.92 MHz
2013	[41]	AES-128	Gen2	5 μ W (AES: 0.8 μ W)	Yes (ASIC)	0.13 μ m	3.5 MHz
2014	[35]	AES-128	ISO/IEC 29167-6	147 μ W (AES: 6 μ W)	Yes (ASIC)	Tower 0.18 μ m	1.25 MHz
2014	[44]	Self-developed	Gen2 V2 compliant	5.5 μ W	No (simulation)	TSMC 0.18 μ m	1.92 MHz
2015	[36]	RAMON	ISO/IEC 29167-19	N/A	Yes (ASIC)	N/A	N/A
2015	[42]	AES-128	ISO/IEC 29167 compliant	8.8 μ W (AES: 5.5 μ W)	Yes (FPGA)	0.18 μ m	1.92 MHz
2017	[45]	Feistel	GB/T29768-2013	3.15 μ W	Yes (ASIC)	SMIC 0.18 μ m	1.92 MHz

TSMC: Taiwan Semiconductor Manufacturing Company; SMIC: Semiconductor Manufacturing International Corporation

standard GB/T29768-2013 can prevail and be widely applied [46].

In addition to the hardware implementations, there are other publications concerning crypto suites on RFID tags. In [47] and [48], the authors deal with the analysis and improvement of security related to Protocol 1, specified by ISO/IEC 29167-6 (working draft), on the one hand, and, on the other hand, with the analysis and evaluation of the specified timings. In contrast, the work in [49] compares some crypto suites of the ISO/IEC 29167 family, namely, the exclusive-OR operation used in cryptography (XOR), AES-128, PRESENT-80, and CryptoGPS, in terms of allocation time as well as collisions. The work also discusses the influence of these results on IoT applications. A completely different approach to encryption in RFID systems is presented in [50]. Here, a preencryption based on AES-128 is proposed at the application level. The data are encrypted at the reader before transmission or decrypted after reception. No changes to the protocol are necessary as a result.

As can be seen from this literature overview, there are very few publications dealing with the current standard for security services in UHF RFID systems, namely, the ISO/IEC 29167. This standard was ratified in 2014 and is continually supplemented with new crypto suites (see “Overview of the ISO/IEC 29167 Crypto Suites”). Thus, our research is currently focused on the development of a wireless passive-sensor ASIC based on UHF RFID. An important part of this research is the tag-side implementation of different encryption methods according to ISO/IEC 29167. Currently, we are focusing on the RAMON and Grain-128A crypto suites, but, in the near future, more algorithms from the ISO/IEC 29167 family will be considered. To test these encryption algorithms, however, adjustments to the protocol must be made quickly, and this is not supported by commercial, off-the-shelf readers. The use of an SDR-based UHF RFID reader is thus indispensable in the development and implementation of crypto suites in UHF RFID systems.

Overview of the ISO/IEC 29167 Crypto Suites

This list is a summary of all of the crypto suites currently published in the International Organization for Standardization/International Electrotechnical Commission (ISO/IEC) 29167 family. It provides a short description of the key facts of each encryption algorithm.

- *ISO/IEC 29167-10:2017* specifies the crypto suite for Advanced Encryption Standard (AES)-128. This is a symmetrical encryption procedure (i.e., the keys for encryption and decryption are identical [65]).
- *ISO/IEC 29167-22:2018* defines the crypto suite for Speck. This is a lightweight block cipher that works based on an add-rotate-exclusive-OR-operation algorithm [66].
- *ISO/IEC 29167-16:2015* describes a crypto suite based on elliptic-curve cryptography (ECC). This is an asymmetric cryptosystem that uses operations on elliptic curves over finite bodies [67].
- *ISO/IEC 29167-12:2015* defines the crypto suite for ECC-Diffie-Hellmann (ECC-DH). This provides a common crypto suite with DH-based authentication using ECC over binary fields [68].
- *ISO/IEC 29167-15:2017* defines a coding suite based on an exclusive-OR operation (XOR). This specifies the use of XOR as a basic way to hide plain data in the identity authentication and secure communication procedures [69].
- *ISO/IEC 29167-21:2018* defines the crypto suite for Simon. This is a lightweight block cipher based on a balanced Feistel cipher and optimized for performance in hardware implementations [70].
- *ISO/IEC 29167-19:2019* defines the Rabin-Montgomery (RAMON) variable linear-feedback shift register (VLFSSR) crypto suite. This is an asymmetric encryption method that combines Rabin encryption with Montgomery multiplication [33].
- *ISO/IEC 29167-11:2014* defines the crypto suite for PRESENT-80. This is a lightweight block cipher designed with hardware optimizations in mind, notable for its compact size [71].
- *ISO/IEC 29167-13:2015* defines the crypto suite for Grain-128A. This is a stream cipher where the throughput can easily be scaled up at the expense of additional hardware [72].
- *ISO/IEC 29167-14:2015* defines the cryptographic suite for AES using output feedback mode (OFB). This is an operating mode in which the block cipher AES-128 is converted into a (synchronous) stream cipher [73].
- *ISO/IEC 29167-17:2015* defines the CryptoGPS cryptographic suite. This is a lightweight mechanism using asymmetric techniques and providing a unilateral authentication mechanism, the security of which is related to the difficulty of taking discrete logarithms on elliptic curves [74].

Localization Enhancements

As previously mentioned, researchers are working intensively on the localization and tracking of RFID tags attached to various objects and machinery. Detailed overviews of localization techniques based on RFID technology can be found in [51] and [52]. Planar, phase-based localization systems show a good tradeoff between localization accuracy and system complexity (narrowband systems) and, thus, are promising for IoT and Industry 4.0 applications. The localization of measurement devices in engine test factories, for example, can considerably increase the average number of engine tests per time unit [24]. For engine testing, several measurement devices must be connected to the engine being tested, with the constraint that special measurement devices are shared by the other testbeds in the testing facility. The time that technicians waste searching for the measurement devices they need can be saved by having information about 1) the engine testbeds in which the measurement devices are located and 2) the exact positions of the measurement devices in the testbeds. The latter information can also be exploited for remotely checking that the engine test setup is complete and correct.

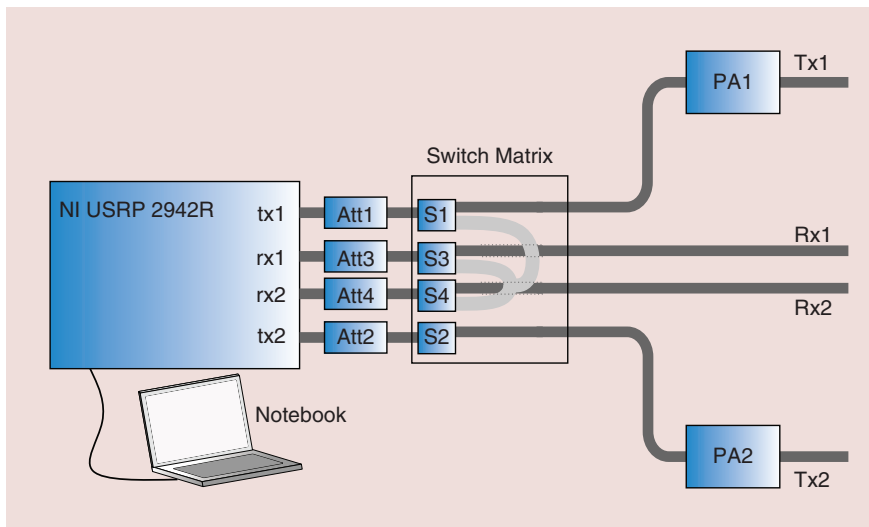


Figure 4. The wireless UHF RFID localization testbed: the NI USRP 2942 R [54] is controlled by a notebook and provides a frequency range between 400 MHz and 4.4 GHz and a measured output power range between 2.5 and 17 dBm. The PAs PA1 and PA2, together with the output power at tx1 and tx2 and the attenuators Att1 and Att2, define the output power level range at the testbed ports Tx1 and Tx2 (i.e., between 18.5 and 33 dBm). The signals received at Rx1 and Rx2 are attenuated by Att3 and Att4, respectively, to account for the maximum allowed receive signal power at rx1 and rx2 of the SDR. Greater attenuation, however, reduces the actual testbed sensitivity. The frequency range of the test system is mainly limited by the PAs (Mini-Circuits ZHL-1000-3W+ [55]) and the antennas (Motorola AN480 [56]) connected to Tx1 and Tx2. The switch matrix can be used to perform a phase offset calibration of the rx chains, by directly connecting tx1 to rx1 and rx2 [26].

Localization Testbed

Figure 4 displays a block diagram of the wireless UHF RFID localization testbed briefly identified in Table 1 (year 2016). The testbed provides two independent transmit (Tx) ports, Tx1 and Tx2, and receive (Rx) chains (ports Rx1 and Rx2), respectively. The actual testbed frequency and power ranges are defined by the SDR and, to a large extent, by the complementary hardware components of the testbed. The testbed can be configured, for example, to provide an adjustable output power between 18.5 and 33 dBm and to provide a frequency range of about 865 to 956 MHz, covering the UHF RFID bands in Europe and the United States. The maximum testbed sensitivity has been estimated to be approximately -80 dBm [53]. This SDR-based RFID reader can easily be used to implement and test a variety of promising localization algorithms using LabVIEW.

Table 3 illustrates a selection of planar (1D or 2D), phase-based tag localization systems that have been presented in the literature. The presented localization systems were optimized specifically for their respective applications, particularly with respect to the specific antenna arrangement used. For example, a single reader antenna is sufficient for the localization of goods on a conveyor belt [57], [58]. However, more reader

antennas are required for a task such as tracking butterflies [59] since arbitrary flight paths can be expected for this. We compare the presented systems with respect to their basic localization approach and their system complexity. The localization systems operate in the time domain (TD), in the spatial domain (SD), or in the time and spatial domains (TD/SD). Furthermore, they either exploit the phase of arrival (PoA) or the phase difference of arrival (PDoA) information of the tag signal. While PoA approaches process the evolution of the recorded signal phases, PDoA approaches process the differences among signal phases recorded with more than one antenna [53]. The comparison of the system complexity includes 1) the reader hardware costs, in particular the number of reader antennas required; 2) the computational costs for a position calculation; 3) the calibration process; and

4) the number of reader/tag communication cycles necessary to calculate or update a tag position.

Buffi et al. [57], [58] present localization systems with only one required reader antenna, whereas Görttschacher et al. [26] present the system with the lowest quantity of fixed antennas for 2D localization. The main difference with respect to computational costs is that the systems rely either on numerical or analytical calculations, which influences the time needed to estimate the tag position. Due to ambiguity in the tag signal phase, all systems require some offset calibration or some other fixed, predefined parameters (e.g., fixed tag [57]/antenna [58] trajectories). The system proposed in [59], for example, exploits a Kalman filter to calibrate the initial position offset and converges to the true tag trajectory after a time lapse. For applications with moving tagged objects, the number of required reader/tag communication cycles for a position calculation must also be considered since this has a strong effect on the time needed for a position calculation. The required communication cycles range from only one [26] to more than eight [60] to several [57], [58]. Table 3 presents the localization accuracy, while Figure 5 gives details about the respective test setups. The systems show similar errors around 10 cm for test setups in

realistic environments. Tests in anechoic chambers obviously show the highest localization accuracy.

Localization Experiment

We tested the performance of the 2D TD/SD-PDoA-based localization system presented in [26], using the localization testbed presented previously, in a student laboratory. The test setup of the localization experiment can be seen in Figure 6, and the test setup top view is sketched in Figure 5(f). An off-the-shelf UHF RFID tag was moved along the trajectory, shown in Figure 7, while the system automatically estimated the tag position coordinates. Figure 7 overlays the estimated (P_{track}) and the actual (P_{act}) tag positions. The evaluation of the measurements gives a mean absolute error of approximately 8 cm. As can be observed in Table 3, this localization system shows outstanding performance with respect to hardware and computational costs and the required reader/tag communication cycles. However, the system requires a prior-position offset calibration at a known tag starting position. For example, for localization of measurement devices in engine testbeds, the tag starting position can be set to the location of the testbed entrance when the device is brought in; thus, the tag can be detected the first time.

TABLE 3. A selection of planar, phase-based tag localization systems presented in the literature (listed by the year that the testbeds were first published). Covered are a representative selection of the basic ideas available in the literature, extracted from the large number of proposed phase-based localization systems.

Year	Reference	Approach	Complexity	Accuracy
2012	[59]	2D TD/SD-PDoA	<ul style="list-style-type: none"> • Four fixed antennas • Pseudo distance (analytic) • Position offset self-calibration (Kalman filter) • Four communication cycles 	1–2 cm (root mean square error)
2014	[60]	2D SD-PoA (TD-PDoA [61])	<ul style="list-style-type: none"> • Eight fixed antennas • Numerical comparison • Phase offset calibration • Eight communication cycles 	10 cm (root mean square error)
2015	[57]	1D TD-PoA (inverse synthetic aperture radar)	<ul style="list-style-type: none"> • One fixed antenna • Numerical comparison • No calibration (known tag trajectory and velocity) • Several communication cycles 	<10 cm (absolute location error)
2016	[62]	2D SD-PDoA	<ul style="list-style-type: none"> • Four fixed antennas • Analytic solution • Phase offset calibration • Four communication cycles 	12.8 cm (mean absolute error)
2017	[58]	2D TD/SD-PoA (synthetic aperture radar)	<ul style="list-style-type: none"> • One movable antenna • Numerical comparison • No calibration (known antenna trajectory and vertical distance) • Several communication cycles 	10–15 cm (mean absolute error)
2017	[26]	2D TD/SD-PDoA	<ul style="list-style-type: none"> • Three fixed antennas • Analytic update • Position offset calibration • One communication cycle 	8 cm (mean absolute error)

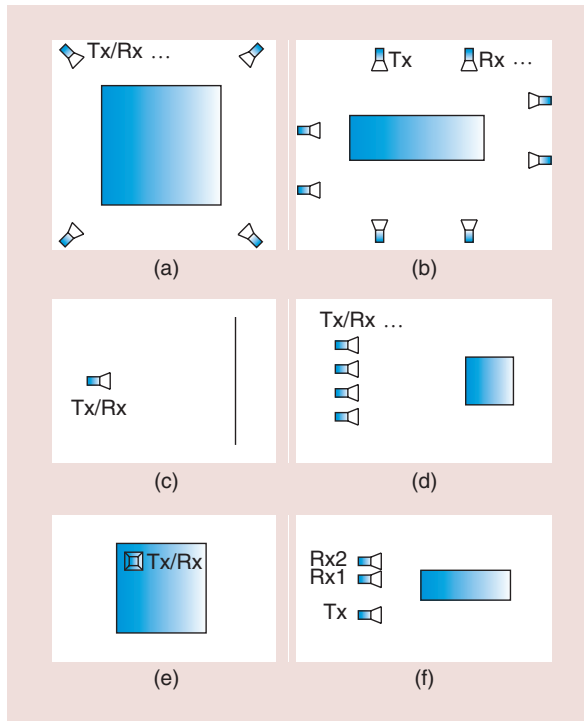


Figure 5. The experimental test setups of planar, phase-based localization systems. (a)–(f) sketch the top views of the test setups of the respective localization systems. The systems use either monostatic antenna setups (Tx/Rx) or bistatic antenna setups (Tx, Rx; antennas consecutively take on the role of Tx in [60]) and are positioned accordingly. The actual test-measurement area is indicated in blue. The dimensions and test environments include (a) Sarkka et al. [59], an anechoic chamber, $2\text{ m} \times 2\text{ m}$; (b) Scherhauf et al. [60], an empty room, $2.25\text{ m} \times 0.75\text{ m}$; (c) Buffi et al. [57], a student restaurant, 2.1 m distance and 0.1 m/s tag velocity; (d) Liu et al. [62], an empty room, $0.8\text{ m} \times 0.8\text{ m}$; (e) Buffi et al. [58], an anechoic chamber, $1.5\text{ m} \times 1.5\text{ m}$; and (f) Görschacher et al. [26], a student laboratory, $1.5\text{ m} \times 0.5\text{ m}$.

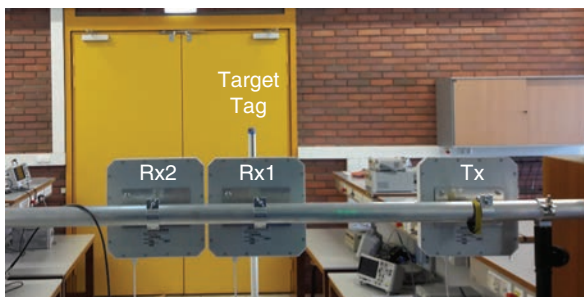


Figure 6. An experimental localization test setup in a student laboratory: the horizontal reader antenna array, composed of Tx, Rx1, and Rx2 antennas, is connected to the Tx1, Rx1, and Rx2 ports of the localization testbed (see Figure 4). The target tag is mounted vertically on a pole and moved along the trajectory presented in Figure 7. The estimated tag position coordinates were recorded every 0.1 m .

Conclusions

This article gives an overview of SDR-based RFID readers, which have been developed and used as wireless testbeds for enhancements in UHF RFID systems. In particular, this work presents enhancements of UHF RFID systems with respect to IoT and Industry 4.0 applications to enable secure communication and wireless localization of passive RFID tags. In both cases, wireless reader testbeds have been individually developed that exploit the advantages of SDRs. The testbeds are based on commercially available SDR products that allow the fast implementation and testing of custom-built tags with dedicated crypto suites and also allow novel localization and tracking algorithms of passive tags.

In the future, researchers can choose from a variety of testbeds, which are presented in the literature and reviewed in this article, to test and verify their proposed enhancements in UHF RFID systems. In particular, UHF RFID systems still lack reliability when operating in real-world application environments. This has prevented UHF RFID technology from truly becoming one of the key enabling technologies for the IoT and Industry 4.0. However, with the use of SDR-based RFID readers, researchers can further improve and enhance the reliability of UHF RFID systems to make them an attractive option for IoT and Industry 4.0 applications.

One prominent research focus with respect to UHF RFID and the IoT/Industry 4.0 is the integration of sensing functionalities in passive UHF RFID tags. Recent research has focused, for example, on the testing and verification of novel and reliable UHF RFID sensor systems using the testbeds highlighted in the “Localization

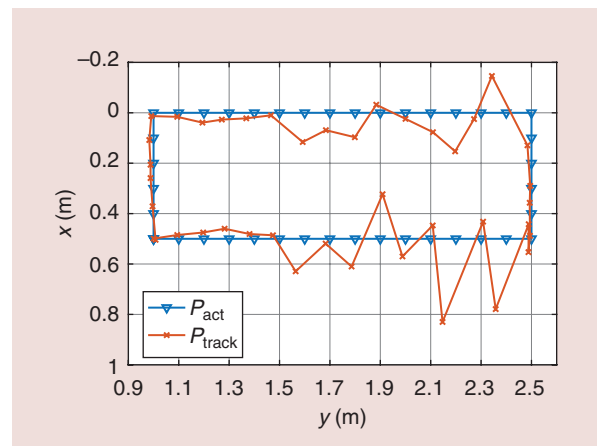


Figure 7. The experimental localization results: the target tag was moved along the trajectory P_{act} in 0.1-m steps while the estimated tag coordinates, P_{track} , were recorded. The system was calibrated at the tag starting position ($x = 0.5\text{ m}$, $y = 1\text{ m}$). The different effects of multipath propagation on the x and y coordinates of the tag position are due to the geometry of the localization system antenna setup. (Source: [53]; used with permission.)

Testbed” section and shown in Figure 4 (e.g., water-filling level sensing [28] and magnetic field sensing [63]). After the first successful verification of these systems, the localization and sensing algorithms have been further implemented in an off-the-shelf RFID reader [64], which is a less expensive and, thus, attractive alternative for IoT and Industry 4.0 applications.

Ultimately, SDR-based readers allow researchers to quickly verify their designs in real-world application environments without the need to search for dedicated reader hardware. As envisioned by Mitola [2], the software radio is a powerful architectural framework that helps us deliver advanced radio services. The research presented in this article shows that this is indeed the case.

References

- [1] M. Rupp, “Rapid prototyping in wireless system design,” in *Proc. 2005 2nd IEEE/EURASIP Conf. DSP-enabled Radio* (Ref. No. 2005/11086), pp. 1–1/15. doi: 10.1049/ic:20050371.
- [2] J. Mitola, “The software radio architecture,” *IEEE Commun. Mag.*, vol. 33, no. 5, pp. 26–38, May 1995. doi: 10.1109/35.393001.
- [3] P. Cruz, N. B. Carvalho, and K. A. Remley, “Designing and testing software-defined radios,” *IEEE Microw. Mag.*, vol. 11, no. 4, pp. 83–94, June 2010. doi: 10.1109/MMM.2010.936493.
- [4] C. Angerer, R. Langwieser, and M. Rupp, “Evaluation and exploration of RFID systems by rapid prototyping,” *Pers. Ubiquitous Comput.*, vol. 16, no. 3, pp. 309–321, Mar. 2012. doi: 10.1007/s00779-011-0391-3.
- [5] P. V. Nikitin and K. V. S. Rao, “LabVIEW-based UHF RFID tag test and measurement system,” *IEEE Trans. Ind. Electron.*, vol. 56, no. 7, pp. 2374–2381, July 2009. doi: 10.1109/TIE.2009.2018434.
- [6] *Information Technology – Radio Frequency Identification for Item Management*, ISO/IEC 18000-6, 2013.
- [7] C. Angerer, B. Knerr, M. Holzer, A. Adalan, and M. Rupp, “Flexible simulation and prototyping for RFID designs,” in *Proc. 1st Int. EURASIP Workshop RFID Technol.*, Sept. 2007, pp. 51–54.
- [8] R. Langwieser, G. Lasser, C. Angerer, and A. Scholtz, “A modular UHF reader frontend for a flexible RFID testbed,” in *Proc. 2nd Int. EURASIP Workshop RFID Technol.*, 2008, pp. 51–54.
- [9] C. Angerer and R. Langwieser, “Flexible evaluation of RFID system parameters using rapid prototyping,” in *Proc. IEEE Int. Conf. RFID*, Apr. 2009, pp. 42–47. doi: 10.1109/RFID.2009.4911188.
- [10] C. Angerer, R. Langwieser, and M. Rupp, “RFID reader receivers for physical layer collision recovery,” *IEEE Trans. Commun.*, vol. 58, no. 12, pp. 3526–3537, Dec. 2010. doi: 10.1109/TCOMM.2010.101910.100004.
- [11] R. Langwieser, C. Angerer, and A. L. Scholtz, “A UHF frontend for MIMO applications in RFID,” in *Proc. IEEE Radio Wireless Symp. (RWS)*, Jan. 2010, pp. 124–127. doi: 10.1109/RWS.2010.5434118.
- [12] R. Langwieser, G. Lasser, C. Angerer, M. Fischer, and A. L. Scholtz, “Active carrier compensation for a multi-antenna RFID reader frontend,” in *Proc. IEEE MTT-S Int. Microw. Symp.*, May 2010, pp. 1532–1535. doi: 10.1109/MWSYM.2010.5518169.
- [13] V. Derbek, C. Steger, R. Weiss, J. Preishuber-Pflugl, and M. Pistauer, “A UHF RFID measurement and evaluation test system,” *Elektrotechnik Inform. Technik*, vol. 124, no. 11, pp. 384–390, Nov. 2007. doi: 10.1007/s00502-007-0482-z.
- [14] P. V. Nikitin and K. V. S. Rao, “Effect of Gen2 protocol parameters on RFID tag performance,” in *Proc. IEEE Int. Conf. RFID*, Apr. 2009, pp. 117–122. doi: 10.1109/RFID.2009.4911178.
- [15] M. Buettner and D. Wetherall, “A flexible software radio transceiver for UHF RFID experimentation,” Univ. of Washington, Seattle, WA, UW TR: UWCSE-09-10-02, Apr. 2011.
- [16] M. Buettner and D. Wetherall, “A software radio-based UHF RFID reader for PHY/MAC experimentation,” in *Proc. IEEE Int. Conf. RFID*, Apr. 2011, pp. 134–141. doi: 10.1109/RFID.2011.5764613.
- [17] L. Catarinucci, D. De Donno, R. Colella, F. Ricciato, and L. Taricone, “A cost-effective SDR platform for performance characterization of RFID tags,” *IEEE Trans. Instrum. Meas.*, vol. 61, no. 4, pp. 903–911, Apr. 2012. doi: 10.1109/TIM.2011.2174899.
- [18] C. R. Valenta and G. D. Durgin, “R.E.S.T. - A flexible, semi-passive platform for developing RFID technologies,” in *Proc. SENSORS*, Oct. 2012, pp. 1–4. doi: 10.1109/ICSENS.2012.6411189.
- [19] F. Galler, T. Faseth, and H. Arthaber, “SDR based EPC UHF RFID reader DS-SS localization testbed,” in *Proc. IEEE 16th Annu. Wireless Microw. Technol. Conf. (WAMICON)*, Apr. 2015, pp. 1–4. doi: 10.1109/WAMICON.2015.7120382.
- [20] F. Galler, T. Faseth, and H. Arthaber, “Implementation aspects of an SDR based EPC RFID reader testbed,” in *Proc. Int. EURASIP Workshop RFID Technol. (EURFID)*, Oct. 2015, pp. 94–97. doi: 10.1109/EURFID.2015.7332391.
- [21] F. Galler et al., “Performance evaluation and verification of spread-spectrum based UHF RFID ranging,” in *Proc. IEEE Int. Conf. RFID*, May 2017, pp. 124–129. doi: 10.1109/RFID.2017.7945597.
- [22] F. Galler, S. Grebien, T. Faseth, K. Witrals, G. Magerl, and H. Arthaber, “Extension of an SDR UHF RFID testbed for MIMO and monostatic time of flight based ranging,” *IEEE J. Radio Freq. Identific.*, vol. 1, no. 1, pp. 32–38, Mar. 2017. doi: 10.1109/JRFID.2017.2749200.
- [23] N. Kargas, F. Mavromatis, and A. Bletsas, “Fully-coherent reader with commodity SDR for Gen2 FM0 and computational RFID,” *IEEE Wireless Commun. Lett.*, vol. 4, no. 6, pp. 617–620, Dec. 2015. doi: 10.1109/LWC.2015.2475749.
- [24] L. Görtschacher et al., “SIMO RFID reader using sensor fusion for tag localization in a selected environment,” *Elektrotechnik Inform. Technik*, vol. 133, no. 3, pp. 183–190, Mar. 2016. doi: 10.1007/s00502-016-0407-9.
- [25] L. Görtschacher et al., “SDR based RFID reader for passive tag localization using phase difference of arrival techniques,” in *Proc. IEEE MTT-S Int. Microw. Symp. (IMS)*, May 2016, pp. 1–4. doi: 10.1109/MWSYM.2016.7538227.
- [26] L. Görtschacher, J. Grosinger, H. N. Khan, and W. Bösch, “Fast two dimensional position update system for UHF RFID tag tracking,” in *Proc. IEEE MTT-S Int. Microw. Symp. (IMS)*, June 2017, pp. 1331–1334. doi: 10.1109/MWSYM.2017.8058857.
- [27] L. Görtschacher, W. Bösch, and J. Grosinger, “UHF RFID sensor tag antenna concept for stable and distance independent remote monitoring,” in *Proc. IEEE Int. Microw. Biomed. Conf. (IMBioC)*, June 2018, pp. 16–18. doi: 10.1109/IMBIOC.2018.8428853.
- [28] L. Görtschacher and J. Grosinger, “UHF RFID sensor system using tag signal patterns: Prototype system,” *IEEE Antennas Wireless Propag. Lett.*, vol. 18, no. 10, pp. 2209–2213, 2019. doi: 10.1109/LAWP.2019.2940336.
- [29] M. Ferdik, M. S. Hesche, L. Rack, G. Saxl, and T. Ussmueller, “NI PXIe based UHF RFID reader,” in *Proc. 11th German Microw. Conf. (GeMiC)*, Mar. 2018, pp. 303–306. doi: 10.23919/GEMIC.2018.8335090.
- [30] M. Ferdik, G. Saxl, and T. Ussmueller, “Battery-less UHF RFID controlled transistor switch for Internet of Things applications—A feasibility study,” in *Proc. IEEE Topical Conf. Wireless Sens. Netw. (WiSNet)*, Jan. 2018, pp. 96–98. doi: 10.1109/WISNET.2018.8311574.
- [31] “PXIe-1075 – PXI-Chassis.” National Instruments Corporation, Sept. 2019. [Online]. Available: <https://www.ni.com/de-at/support/model.pxi-1075.html>
- [32] G. Saxl, M. Ferdik, and T. Ussmueller, “UHF RFID prototyping platform for ISO 29167 decryption based on an SDR,” *Sensors*, vol. 19, no. 10, pp. 617–620, 2019. doi: 10.3390/s19102220.
- [33] *Information Technology – Automatic Identification and Data Capture Techniques – Part 19: Crypto Suite Ramon Security Services for Air Interface Communications*, ISO/IEC 29167-19:2019, June 2019.
- [34] *Information Technology – Automatic Identification and Data Capture Techniques – Part 1: Security Services for RFID Air Interfaces*, ISO/IEC 29167-1:2014, Aug. 2014.

- [35] S. Choi, H. Kim, S. Lee, K. Lee, and H. Lee, "A fully integrated CMOS security-enhanced passive RFID tag," *ETRI J.*, vol. 36, no. 1, pp. 141–150, 2014. doi: 10.4218/etrij.14.0112.0674.
- [36] S. Wallner and K. Finkenzeller, "Secure and interference-robust ISO/IEC 18000-63 compatible UHF-RFID tags by cryptographic authentication primitives," *Int. J. Radio Freq. Identific. Technol. Appl.*, vol. 4, no. 4, p. 342, 2015. doi: 10.1504/IJRFITA.2015.070571.
- [37] M. Feldhofer, J. Wolkerstorfer, and V. Rijmen, "AES implementation on a grain of sand," *IEEE Proc. - Inf. Security*, vol. 152, no. 1, pp. 13–20, Oct. 2005. doi: 10.1049/ip-ifs:20055006.
- [38] M. Kim, J. Ryou, Y. Choi, and S. Jun, "Low-cost cryptographic circuits for authentication in radio frequency identification systems," in *Proc. IEEE Int. Symp. Consumer Electron.*, June 2006, pp. 1–5. doi: 10.1109/ISCE.2006.1689445.
- [39] A. S. W. Man, E. S. Zhang, V. K. N. Lau, C. Y. Tsui, and H. C. Luong, "Low power VLSI design for a RFID passive tag baseband system enhanced with an AES cryptography engine," in *Proc. 1st Annu. RFID Eurasia*, Sept. 2007, pp. 1–6. doi: 10.1109/RFIDEURASIA.2007.4368097.
- [40] H. Kim, T. Ki, S. Lee, and H. Lee, "CMOS security-enhanced passive (SEP) tag supporting to mutual authentication," *IEEE Trans. Ind. Electron.*, vol. 61, no. 9, pp. 4920–4930, Sept. 2014. doi: 10.1109/TIE.2013.2288197.
- [41] J. Ertl, T. Plos, M. Feldhofer, N. Felber, and L. Henzen, "A security-enhanced UHF RFID tag chip," in *Proc. Euromicro Conf. Digit. Syst. Design*, Sept. 2013, pp. 705–712. doi: 10.1109/DSD.2013.80.
- [42] N. X. Hieu, V. N. Nguyen, D. Park, D. Chung, H. Lee, and J. Lee, "A power efficient secure mutual authentication protocol for EPC Gen2v2 standard," in *Proc. Int. SoC Design Conf. (ISOCC)*, Nov. 2015, pp. 325–326. doi: 10.1109/ISOCC.2015.7401719.
- [43] X. Shen, D. Liu, Y. Yang, and J. Wang, "A low-cost UHF RFID tag baseband with an idea cryptography engine," in *Proc. 2010 Internet of Things (IOT)*, Nov. 2010, pp. 1–5. doi: 10.1109/IOT.2010.5678440.
- [44] Z. Liu, D. Liu, L. Li, H. Lin, and Z. Yong, "Implementation of a new RFID authentication protocol for EPC Gen2 standard," *IEEE Sensors J.*, vol. 15, no. 2, pp. 1003–1011, Feb. 2015. doi: 10.1109/JSEN.2014.2359796.
- [45] Q. Li et al., "Secure UHF-RFID tag for vehicular traffic management system," in *Proc. IEEE Int. Conf. RFID*, May 2017, pp. 26–29. doi: 10.1109/RFID.2017.7945582.
- [46] "Information Technology: Radio Frequency Identification–Air Interface Protocol at 800/900 MHz," *GB/T 29768-2013*, 2013.
- [47] B. Song, J. Y. Hwang, and K. Shim, "Security improvement of an RFID security protocol of ISO/IEC WD 29167-6," *IEEE Commun. Lett.*, vol. 15, no. 12, pp. 1375–1377, Dec. 2011. doi: 10.1109/LCOMM.2011.103111.111816.
- [48] Y. S. Kang, E. O'Sullivan, D. Choi, and M. O'Neill, "Security analysis on RFID mutual authentication protocol," in *Proc. Int. Workshop Inf. Security Appl.*, 2016, pp. 65–74. doi: 10.1007/978-3-319-31875-2_6.
- [49] A. Shahrafidz Khalid, E. Conchon, and F. Peyrard, "Evaluation of rain RFID authentication schemes," in *Proc. Int. Conf. Security Smart Cities, Ind. Control Syst. Commun. (SSIC)*, July 2016, pp. 1–8. doi: 10.1109/SSIC.2016.7571807.
- [50] K. ElMahgoub, "Pre-encrypted user data for secure passive UHF RFID communication," in *Proc. 12th Int. Comput. Eng. Conf. (ICENCO)*, Dec. 2016, pp. 26–29. doi: 10.1109/ICENCO.2016.7856440.
- [51] R. Miesen et al., "Where is the tag?" *IEEE Microw. Mag.*, vol. 12, no. 7, pp. S49–S63, Dec. 2011. doi: 10.1109/MMM.2011.942730.
- [52] A. Costanzo, D. Masotti, T. Ussmueller, and R. Weigel, "Tag, you're it: Ranging and finding via RFID technology," *IEEE Microw. Mag.*, vol. 14, no. 5, pp. 36–46, July 2013. doi: 10.1109/MMM.2013.2259392.
- [53] L. Görtschacher, "Novel UHF RFID tracking and sensing systems," Ph.D. thesis, Inst. Microwave Photonic Engineering, Graz Univ. Technol., Graz, Austria, 2019.
- [54] "Specifications USRP-2942," National Instruments. 2017. [Online]. Available: <https://www.ni.com/pdf/manuals/374410d.pdf>
- [55] "ZHL-1000-3W+," Mini-Circuits. 2015. [Online]. Available: <https://www.minicircuits.com/WebStore/dashboard.html?model=ZHL-1000-3W%2B>
- [56] "Zebra RFID antenna family," Zebra Technologies. 2015. [Online]. Available: https://www.zebra.com/content/dam/zebra_new_ia/en-us/solutions-verticals/product/RFID/Antenna/brochure/uhf-rfid-antennas-brochure-en-us.pdf
- [57] A. Buffi, P. Nepa, and F. Lombardini, "A phase-based technique for localization of UHF-RFID tags moving on a conveyor belt: Performance analysis and test-case measurements," *IEEE Sensors J.*, vol. 15, no. 1, pp. 387–396, Jan. 2015. doi: 10.1109/JSEN.2014.2344713.
- [58] A. Buffi, M. R. Pino, and P. Nepa, "Experimental validation of a SAR-based RFID localization technique exploiting an automated handling system," *IEEE Antennas Wireless Propag. Lett.*, vol. 16, pp. 2795–2798, Aug. 2017. doi: 10.1109/LAWP.2017.2747216.
- [59] S. Sarkka, V. V. Viikari, M. Huusko, and K. Jaakkola, "Phase-based UHF RFID tracking with nonlinear Kalman filtering and smoothing," *IEEE Sensors J.*, vol. 12, no. 5, pp. 904–910, May 2012. doi: 10.1109/JSEN.2011.2164062.
- [60] M. Scherhäufl, M. Pichler, and A. Stelzer, "Localization of passive UHF RFID tags based on inverse synthetic apertures," in *Proc. IEEE Int. Conf. RFID (IEEE RFID)*, Apr. 2014, pp. 82–88. doi: 10.1109/RFID.2014.6810716.
- [61] M. Scherhäufl, M. Pichler, and A. Stelzer, "UHF RFID localization based on evaluation of backscattered tag signals," *IEEE Trans. Instrum. Meas.*, vol. 64, no. 11, pp. 2889–2899, Nov. 2015. doi: 10.1109/TIM.2015.2440554.
- [62] T. Liu, Y. Liu, L. Yang, Y. Guo, and C. Wang, "BackPos: High accuracy backscatter positioning system," *IEEE Trans. Mobile Comput.*, vol. 15, no. 3, pp. 586–598, Mar. 2016. doi: 10.1109/TMC.2015.2424437.
- [63] R. Fischbacher, L. Görtschacher, F. Amtmann, P. Priller, W. Bösch, and J. Grosinger, "Localization of UHF RFID magnetic field sensor tags," in *Proc. IEEE Radio Wireless Symp. (RWS)*, 2020, pp. 169–172. doi: 10.1109/RWS45077.2020.9050026.
- [64] L. Görtschacher and J. Grosinger, "Localization of signal pattern based UHF RFID sensor tags," *IEEE Microw. Compon. Lett.*, vol. 29, no. 11, pp. 753–756, 2019. doi: 10.1109/LMWC.2019.2940082.
- [65] Information Technology – Automatic Identification and Data Capture Techniques – Part 10: Crypto Suite AES-128 Security Services for Air Interface Communications, ISO/IEC 29167-10:2017, Sept. 2017.
- [66] Information Technology – Automatic Identification and Data Capture Techniques – Part 22: Crypto Suite Speck Security Services for Air Interface Communications, ISO/IEC 29167-22:2018, Nov. 2018.
- [67] Information Technology – Automatic Identification and Data Capture Techniques – Part 16: Crypto Suite ECDSA-ECDH Security Services for Air Interface Communications, ISO/IEC 29167-16:2015, Nov. 2015.
- [68] Information Technology – Automatic Identification and Data Capture Techniques – Part 12: Crypto Suite ECC-DH Security Services for Air Interface Communications, ISO/IEC 29167-12:2015, May 2015.
- [69] Information Technology – Automatic Identification and Data Capture Techniques – Part 15: Crypto Suite XOR Security Services for Air Interface Communications, ISO/IEC TS 29167-15:2017, Sept. 2017.
- [70] Information Technology – Automatic Identification and Data Capture Techniques – Part 21: Crypto Suite Simon Security Services for Air Interface Communications, ISO/IEC 29167-21:2018, Oct. 2018.
- [71] Information Technology – Automatic Identification and Data Capture Techniques – Part 11: Crypto Suite Present-80 Security Services for Air Interface Communications, ISO/IEC 29167-11:2014, Aug. 2014.
- [72] Information Technology – Automatic Identification and Data Capture Techniques – Part 13: Crypto Suite Grain-128a Security Services for Air Interface Communications, ISO/IEC 29167-13:2015, May 2015.
- [73] Information Technology – Automatic Identification and Data Capture Techniques – Part 14: Crypto Suite AES OFB Security Services for Air Interface Communications, ISO/IEC 29167-14:2015, Oct. 2015.
- [74] Information Technology – Automatic Identification and Data Capture Techniques – Part 17: Crypto Suite Cryptogps Security Services for Air Interface Communications, ISO/IEC 29167-17:2015, June 2015.





©COURTESY OF MATTHIAS GAREIS

Stocktaking Robots, Automatic Inventory, and 3D Product Maps

*Matthias Gareis, Andreas Parr,
Johannes Trabert, Tom Mehner,
Martin Vossiek, and Christian Carlowitz*

Matthias Gareis (matthias.m.gareis@fau.de), Martin Vossiek (martin.vossiek@fau.de), and Christian Carlowitz (christian.carlowitz@fau.de) are with the Friedrich-Alexander University Erlangen-Nuremberg, Erlangen, 91058, Germany. Andreas Parr (andreas.parr@analog.com) is with Analog Devices, Neubiberg, 85579, Germany. Johannes Trabert (johannes.trabert@metralabs.com) and Tom Mehner (tom.mehner@metralabs.com) are with MetraLabs, Ilmenau, 98693, Germany.

Digital Object Identifier 10.1109/MMM.2020.3042443

Date of current version: 3 February 2021

In our age of global networks and the Internet of Things, communication and identification with a transponder tagged on goods and products have become increasingly important [1]. There is not only a need for the identification of the labeled objects but also for finding their exact positions in 3D space. Radio-frequency identification (RFID) offers both and is, in fact, already used in a vast field of applications, such as access control, goods logistics, indoor localization, automation, stocktaking, and many others [2]–[6]. Figure 1 illustrates a mobile robot platform for automatic inventory rounds that is used to acquire 3D product maps with ultrahigh-frequency (UHF)-RFID technology.

The introduction of EPCglobal class-1, generation-2 UHF-RFID standards [7] created a new field of research that expanded the market and thus decreased the cost of the tags. Sales forecasts for 2020 predict a total annual turnover exceeding US\$20 billion [8]; hence, many companies are interested in simplifying big firms' logistics, including increasing productivity and efficiency [9], by adding localization. Toward this end, at the output of a commercial off-the-shelf (COTS) reader, we obtain the received signal strength (RSS) value and the signal phase of the tag [10], both of which are dependent on the reader-to-tag distance and distortions from multipath propagation in dense indoor environments [11].

RSS-based localization techniques have been discussed by [12]–[14], all of which, due to multipath propagation, must deal with the interference of the additional signal paths caused by reflecting objects in indoor scenarios and, therefore, poor performance [15]. Considerable effort has been spent on minimizing this effect by creating multiple propagation models that better fit indoor scenarios [12], including real system and tag properties, such as the polarization of the antennas or an electromagnetic wave propagation model of the tag [13], [16]. In [14], the reference nodes on the ceiling of a building were used to achieve accuracies within 2.5 m in industrial, supply chain, and healthcare applications. Also, the use of multiple frequencies in combination with RSS-based localization for ranging was introduced to reduce the influence of multiple signal interference [17].

Time-of-arrival (ToA) position estimation is more accurate in strong multipath environments but is more challenging in terms of UHF-RFID since there is a low signal-to-noise ratio (SNR) and only a narrow bandwidth [18], [19]. A comparison between phase of arrival (PoA) and ToA showed that, for an ultranarrow-band system like UHF-RFID, PoA performs better [20]. Phase-evaluating systems seem to be extremely promising with respect to localization accuracy, compared to RSS- and ToA-based approaches. To achieve a unique position estimation due to the 2π phase periodicity,

multiple measurements with differing signal conditions (that is, different signal propagation paths) must be taken.

We differentiate between a static-antenna, moving-antenna, and moving-tag setup. For static antennas, a multifrequency approach can lead to disambiguity if the system bandwidth is large enough. One solution for frequencies from 902 to 922 MHz was presented by [21], where fixed frequencies were chosen with respect to the maximum unambiguous range and minimum tag-to-tag distance. For the European regulatory restrictions, which restrict frequency ranges from 865 to 868 MHz and total bandwidth to only 3 MHz, this approach is more difficult to realize. For their part, [22] and [23] proposed a frequency-stepped, continuous wave approach to reduce the multipath and increase localization accuracy. The evaluation of this concept leads to position errors lower than 50 mm in the 2D plane.



Figure 1. A mobile robot platform is equipped with a UHF-RFID reader that has multiple antennas for automatic and autonomous stocktaking in warehouse applications.

The moving-antenna concept considers moving tags while the reader is in a steady position. In [24], a relative localization algorithm was presented that used a phase-unwrapping Kalman filter in combination with a COTS reader with 180° phase ambiguity in a moderate multipath environment. Furthermore, there have been solutions with inverse synthetic aperture radars (SARs) providing absolute positions [25], [26]. The accuracy in the 2D plane is within a few centimeters; nevertheless, the error sources are still the multipath and noise.

The scope of this article focuses on the third group, the moving-reader antenna setup, which is perfectly suited for a stocktaking system as it is needed, for example, in warehouses. A lot of work has already been published on 2D positioning principles [22], [27]–[30] using different direction-of-arrival (DoA) techniques but only to a limited extent for 3D problems as they actually occur in the industry. This article demonstrates that a phase-based, backscatter SAR localization technique in which antennas mounted on a robot can perform the localization of goods within a few centimeters of accuracy. The robot drives along an aperture, while the reader measures in a full multiple input, multiple output (MIMO) configuration, creating additional signal paths that differ from each other, thus enabling phase-based backscatter SAR localization under strong multipath conditions.

System Model

For the proposed 3D, phase-based UHF-RFID backscatter SAR localization, we first define the geometrical associations between the antennas and tags.

System Geometry

Consider the setup displayed in Figure 2, where N antennas are mounted on a robot. The central position of the robot is known and, as a consequence, the position of the n th antenna at $\vec{r}_{a,n}$ is known, too. There are K tags with unknown positions mounted on objects. The k th tag is at $\vec{r}_{t,k}$, so we can define the antenna-to-tag distance as

$$d_{at,nk} = \|\vec{r}_{a,n} - \vec{r}_{t,k}\|. \quad (1)$$

When a tag is in the illuminated area of an antenna, we assume the radiation field to be isotropic, which simplifies the scenario in terms of the phase and gain and leaves only two states to take care of: the tag is read or the tag is not read.

The received signals of the antenna array can be written as

$$\mathbf{x}(\vec{r}_{t,k}) = \hat{A}\mathbf{a}(\vec{r}_{t,k}) = \hat{A}[e^{j\phi_{k,1}}, e^{j\phi_{k,2}}, \dots, e^{j\phi_{k,I}}]^T, \quad (2)$$

where $e^{j\phi_{k,i}}$ describes the measured phase value, \hat{A} is the amplitude value of the k th tag of the i th path, and $\mathbf{a}(\vec{r}_{t,k})$ is also known as the *array steering vector* [31].

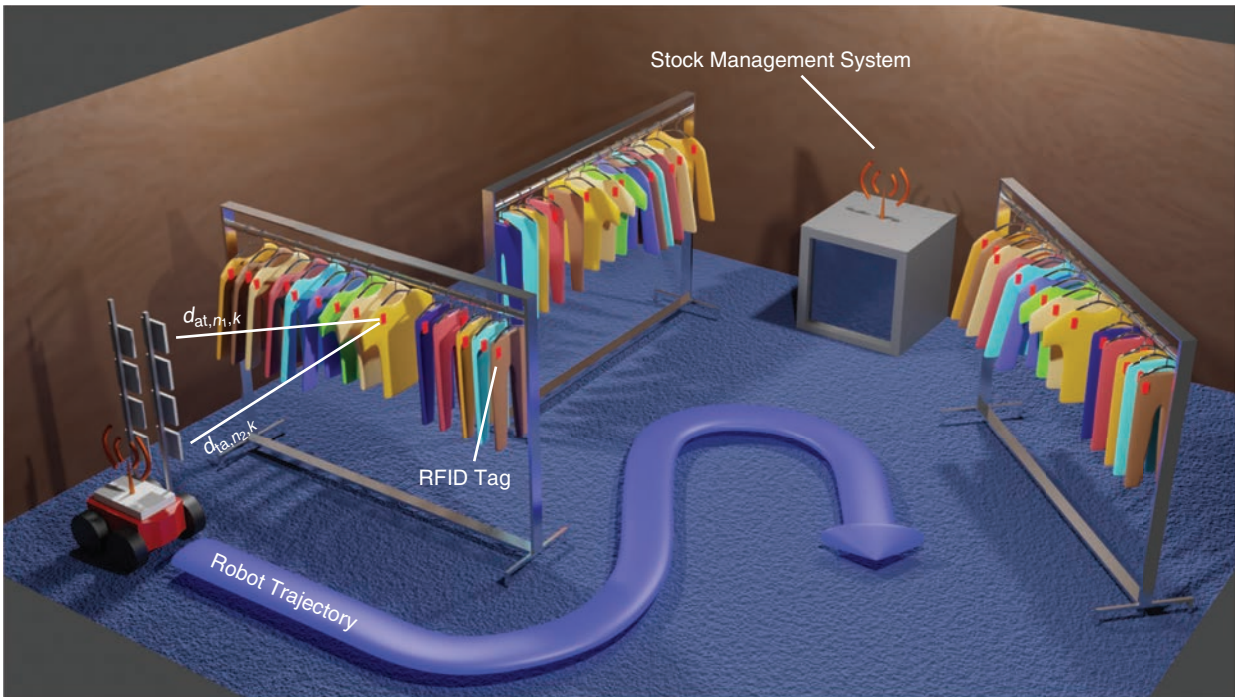


Figure 2. A typical scenario for a robot equipped with a multi-antenna RFID system for SAR positioning techniques. The robot drives on a trajectory and reads the tags labeled on different goods. The system can be used for complete autonomous retail and stocktaking rounds within a warehouse.

Signal Model

Modern RFID readers measure the signal phase and RSS of identified tags [10]. The signal phase consists of a stationary part φ_0 ; the phase φ_{bs} , which includes the backscatter modulation; and, most interesting for our purposes, the propagation phase φ_{prop} that is directly dependent on the antenna-to-tag and tag-to-antenna distances $d_{at,nk}$ and $d_{ta,nk}$, respectively, in a multistatic radar scenario. φ_0 represents the offset caused by cables, tag delay, and other receiver components. The reader also reports the ID of the measured tag; thus, for each tag and antenna combination, a signal path is created.

When all of the phase offsets are calibrated, the signal phase is

$$\varphi_{prop,i} = \left(2\pi \frac{d_{at} + d_{ta}}{\lambda_c} \right) \bmod 2\pi, \quad (3)$$

where λ_c is about 0.35 m for European UHF-RFID frequencies. Many COTS readers only have a 180° phase ambiguity, which leads to a phase φ_{prop} that can be reported as both φ_{prop} or $\varphi_{prop} + \pi$. This must be considered and corrected when the phase is used in localization algorithms. The 2π periodicity leads to an infinite number of possible positions $\tilde{r}_{t,k}$ placed on concentric ellipses and located at λ_c intervals in each case.

Positioning Principles

In general, there are separations between the maximum-likelihood (ML), subspace-based, and beamforming techniques adapted for the backscatter localization in DoA estimation [31]. The signal models received from the system model form the basis for the following approaches.

ML Techniques

The ML estimator (MLE) addressing narrowband source localization was proposed very early in the literature [32], [33]. The idea behind the MLE is to subtract an estimated signal that consists only the desired signal components from the received signal to obtain the smallest residual consisting only of interference and noise, assuming both to be spatially uncorrelated, and thus to reconstruct the desired signal [31]. The computational load of this technique, although extremely high compared to other techniques, may be legitimate for a scenario with a low SNR, a small sample number, or data sets including coherent signals [34].

In the literature, there have been several approaches to estimate the position of UHF-RFID tags with ML techniques considering their high computational effort [32]. A 1D MLE for a reader moving along a known trajectory was introduced by [15], showing the root-mean-square error (RMSE) dependent on the SNR. A 2D extension for the localization of books in a library

reaches accuracies with an RMSE value of 0.02 m in an indoor environment with a floor space of 3.5 m × 2.5 m [35] and a value of 0.054 m with reduced computing time [36]. However, due to the high computational effort or a lower accuracy compromise [32], a much work is put into other techniques, a few of which are described in the following.

Subspace-Based Techniques

Subspace-based localization resolution does not theoretically rely on the size of an array aperture when the observation time and SNR are large enough, so the spatial correlation matrix R_{xx} of the received signal can be estimated very precisely [37]. The foundational idea of this technique can be summarized as follows [31]. Because R_{xx} is a Hermetian symmetric matrix, its eigenvectors are orthogonal to each other, and it can thus be divided into a signal and a noise subspace orthogonal to each other as well. The subspace analysis compares and classifies these subspaces as a way of searching for directions in the signal subspace associated with steering vectors, and they are still orthogonal to the noise subspace and allow for the extraction of a parameter set.

In the following sections, the well-known multiple signal classification (MUSIC) algorithm and estimation of signal parameters via rotational invariance techniques (ESPRIT) algorithm are explained, and their usability for UHF-RFID is discussed. The signal correlation matrix R_{xx} is needed for all proposed methods and can be estimated as

$$R_{xx} \approx \hat{R}_{xx} = \frac{1}{N} \sum_{n=1}^N \mathbf{x}(t_n) \mathbf{x}^H(t_n), \quad (4)$$

where \mathbf{x} is the collected data vector from (2).

MUSIC

The MUSIC algorithm was originally introduced specifically as a DoA estimator [34], and it is thus well suited to multireader or multibeam setups as it is a superresolution direction-finding method [11], [31]. The basic principle of having a spatial correlation matrix R_{xx} that can be divided into two orthogonal subspaces spanned by its eigenvectors stays the same. The estimation of steering vectors that are orthogonal to the noise subspace and consequently in the signal subspace enables the determination of the DoA. Moreover, by extracting the signal parameter set, this estimate approaches the Cramer-Rao bound in cases of poorly correlated or even coherent signals [34], [38].

Researchers in [27] used a 2D MUSIC algorithm to estimate the angle and range of UHF-RFID tags, for which the phase offsets caused by the cables and antennas needed to be known. Furthermore, the authors

assumed near-field conditions and calibrated the angles separately. It is important to calibrate within the same environment because even small changes in the environmental setting cause deviations from the calibration and consequently degrade the estimation accuracy, making this 2D MUSIC algorithm costly in terms of the required time for regular recalibration. A solution for an accurate position estimation, even in impulsive noise environments, was demonstrated by [28] with the introduction of the propagator method using the fractional, lower-order correlation matrix between two sensors in a simulation environment.

ESPRIT

The ESPRIT algorithm is different from the MUSIC algorithm because it doesn't require knowing the exact array-steering matrix and consequently needs no exact knowledge of the antenna array geometry and no calibration of any offsets in the phase [31]. This is a big advantage since the calibration of an antenna array is very time consuming. Instead, it reduces the computational load compared to an ML estimation by using specific array structures, that is, two identical subarrays. MUSIC works in the noise subspace for finding the desired data parameter set and is thus able to obtain a position, while ESPRIT uses two signal subspaces of the same dimension linked with a rotating operator. The ESPRIT algorithm has a lower computational load than MUSIC because the signal parameters are found directly in the eigenvalues, while its performance is the same as the MUSIC algorithm [39]. A DoA estimation with two uniform linear arrays was demonstrated by [40].

Beamformer

The idea behind beamforming techniques is to steer the beam of an array for each measurement (in this case, by applying offline digital phase shifts for each timestamp and each tag) to a location $\vec{r}_{t,steer}$ to obtain the maximum power when the steering location is the DoA estimate [31], [34]:

$$P(\mathbf{w}) = \frac{1}{N} \sum_{n=1}^N \mathbf{w}^H \mathbf{x}(t_n) \mathbf{x}^H(t_n) \mathbf{w}, \quad (5)$$

where \mathbf{w} describes the weight vector. With the introduction of \mathbf{w} , different beamforming approaches can be selected.

Conventional Beamformer

In the conventional beamforming approach, an area is scanned by steering the beam of an array to every point of a mesh mapped onto the room. The k th tag is found when the phase of the steering vector

$\mathbf{a}(\vec{r}_{t,k})$ (2) is aligned to the received signal phases at all antennas, adding up the phases and amplitudes correctly and consequently maximizing the output power from (5). The weighting vector \mathbf{w} is hereby $\mathbf{w} = \mathbf{a}(\vec{r}_{t,k})$, acting as a spatial filter. To increase the resolution of this technique, more antenna elements can be added to the array [31]. A promising approach was published by [11]. The authors used a uniform rectangular array spanned by a robot arm to build up a 1D MIMO system that could detect tags with an accuracy within 30 cm in strong multipath environments assuming a double Ricean fading channel with $K = 10$ dB. The accuracy can be improved by increasing the synthetic aperture size, that is, by moving an antenna.

Capon's Beamformer

The conventional beamformer is able to handle only a single signal. When there are two incoming signals, the power is influenced by both. Capon's beamformer overcomes this problem by nulling all of the other directions and hence eliminating the other signals. The cost is a higher computation time because $\hat{\mathbf{R}}_{xx}$ needs to be inverted, which is not possible for correlated signals in which $\hat{\mathbf{R}}_{xx}$ becomes singular [31], [41].

Performance Bounds

We have already briefly reviewed the shortcomings of RSS- and ToA-based techniques in the introductory section, so this section focuses on analyzing the performance bounds of passive UHF-RFID-tag, phase-based spatial localization. The main contributor to positioning errors is the multipath, as illustrated in Figure 3. Reflecting objects that cause additional signal paths are numerous in industrial environments and cannot be avoided in real-world scenarios. Multiple paths superimpose the desired line-of-sight (LoS) signal and disturb the received phase. As is demonstrated in [42], the introduced error can easily lead to phase displacements on the order of 30° , causing wrong velocity assumptions of up to 0.5 m/s and localization errors of up to 1 m in frequency-modulated continuous wave approaches.

The impact of the signal bandwidth of a continuous wave in severe multipath environments was evaluated by [43]. The authors concluded that the multipath reflection could be resolved if the roundtrip time-of-flight (RTOF) of the multipath exceeded the RTOF of the LoS signal by more than the resolution limit, thus not disturbing the range estimation. Unfortunately, the resolution limit is inversely proportional to the bandwidth of the system:

$$\delta_{rad} \approx \frac{c_0}{2B}, \quad (6)$$

where B is the system link bandwidth and is only about 3 MHz, as it must be under European regulations.

However, subspace-based techniques and SAR may mitigate this effect [44]. The subspace-based localization algorithms are all dependent on the noise covariance matrix \mathbf{R}_{xx} that becomes nonfull rank and singular for highly correlated or even coherent signals, which is not unusual in dense multipath environments. To mitigate this issue, preprocessing must be applied to decorrelate the signals again [45], for example, spatial smoothing or forward-backward averaging. With those smoothing techniques, it is possible to reduce the effect of the multipath on these algorithms, making them powerful

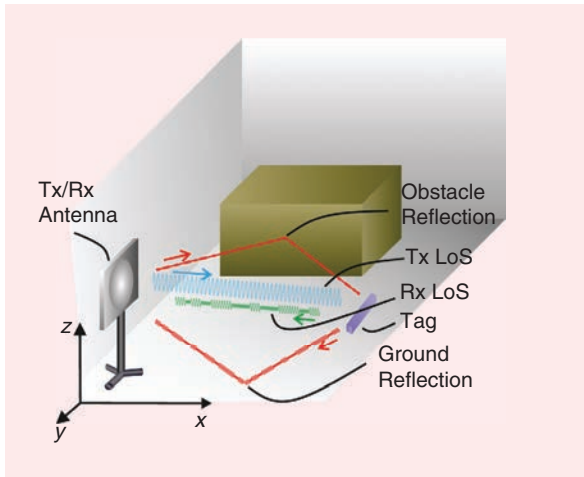


Figure 3. The multipath is caused by objects reflecting the waves from the purple tag. The transmitter (Tx) LoS path is pictured in blue, and the direct-LoS return path in green. Possible multipath reflections are colored in red. The multipath signals can be stronger at the receiver input than the LoS signal depending on the environment and consequently lead to bad positioning results. The variable z represents the tag elevation, and x and y represent the tag position in the azimuth plane parallel to the warehouse floor. Rx: receiver.

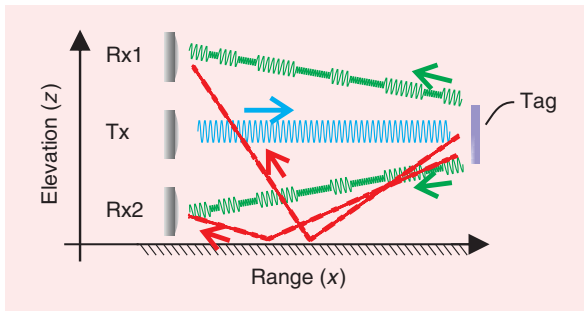


Figure 4. The multipath signals arriving at the two Rx antennas Rx1 and Rx2 (in red) differ from each other. Since a movement of the antennas causes the multipath to add up incoherently in the SAR algorithm, the multipath influence will be mitigated, even in dense multipath environments.

localization tools but requiring the knowledge of the number of correlated signals [31], [46]. The authors of [47] also verified the practical relevance of spatial smoothing for 2D direction finding. They introduced an iterative method that does not need repeating subarrays decreased in their effective size.

SAR approaches overcome the problems of the multipath on their own as they take advantage of the single good correlation result when, first, the assumption holds true that the hypothetical signal steers to the position of the measured signal and, consequently, second, that all of the acquired measurements superimpose coherently, while the multipath adds up incoherently because it differs between data points and does not match the assumed signal model [48]. As a result, multipath effects can be strongly reduced by using more sampling points as is done, for example, with a longer aperture size or a MIMO configuration. Figure 4 indicates that the multipath won't add up coherently as it varies with every antenna position in this static case. Considering a moving antenna scenario improves this effect significantly. Capon's beamformer can be beneficial, too, since it results in nulling all of the directions except the steering direction when there is no correlation between the signals [31], [41].

SAR Processing

The basic signal properties of a 2D SAR acquisition in a monostatic scenario are expressed in Figure 5. Consider the simplest case of an antenna moving along a straight line. The antenna is designed to exhibit a large azimuth angle to track the target, namely, the orange rectangle, as long as possible while moving past it to create a long synthetic aperture L_{SA} . The measured phase of this scenario is also indicated in Figure 5, where the orange tag is assumed to be located at position $\vec{r}_t = (\frac{z}{2})$ m and the antenna is moving along the x -axis from 0 to 4 m at $y = 0$ m. Each antenna position created by the movement has its own signal path linked to a measured phase.

For each phase and signal path, the beamforming technique is applied. A grid is used to search for the tag by steering the beam of the whole array synthesized by the moving antenna to every grid point, as seen in Figure 6, searching for the maximum power according to (5). Each hypothetical phase is determined by

$$\phi_{hyp} = \left(2\pi \frac{2\sqrt{\Delta x^2 + \Delta y^2}}{\lambda_c} \right) \bmod 2\pi \quad (7)$$

for each antenna and each grid point, where the factor 2 accounts for the up- and downlink path length of the signal and the root term is the distance from the antenna to the tag. The computational burden is directly proportional to the number of

samples taken, the grid spacing, and the grid dimensions. To achieve high accuracy, the antenna position error must be smaller than a fraction of a wavelength; otherwise, the superposition in the holographic reconstruction leads to a broadened power peak and thus lowers the maximum achievable accuracy.

As mentioned, one signal path is certainly not enough to localize the tag due to the 2π periodicity of the measured phase. Figure 7 illustrates the aforementioned scenario with two antenna positions and, for reasons of simplicity, a wavelength of $\lambda_c = 1$ m. Obviously, there is more than one possible location for the tag. Adding one more signal path to the setup, as in Figure 8, already reduces the possible locations of the tag.

To reduce the ambiguity, many data sets must be available, so the design of the antenna array requires particular attention. The sampling theorem in a mono-static antenna setup for the far-field condition states the distance between two samples as

$$x_s < \frac{\lambda_c}{4}. \quad (8)$$

The factor 4 results from the wave traveling back and forth. The theorem's boundary can be lowered by taking the antenna beamwidth θ into account, which gives

$$x_s < \frac{\lambda_c}{4 \sin \frac{\theta}{2}}. \quad (9)$$

SAR-based approaches can easily fulfill this constraint for x_s because the antennas achieve smaller distances to themselves through their movement, even lowering the constraint for near-field conditions [11]. While 2D localization requires a 1D trajectory to be unambiguous, for the 3D case, a 2D trajectory is needed [49].

Digital Signal Processing Techniques

The computational burden of the classical, grid search-based SAR approach is very high compared to the other digital signal processing (DSP) techniques covered in this section. Consider a room with a size of $5 \text{ m} \times 5 \text{ m} \times 2.5 \text{ m}$. In this room, there are K tags, and, for each tag, N measurements are required, where N describes the overall measured phases and each phase

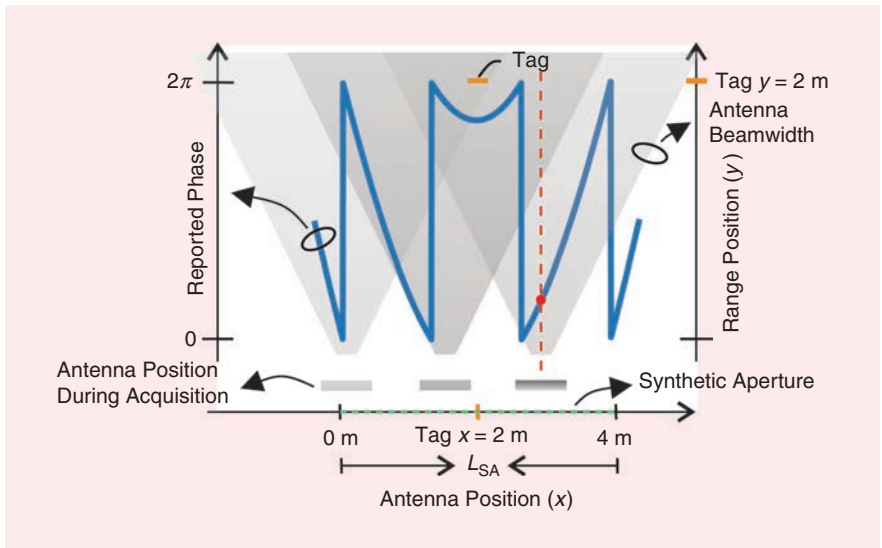


Figure 5. The generation of the synthetic aperture is done by moving an antenna along a trajectory. Each antenna position is linked to a measured data set for the reconstruction algorithm. The measured phase is 2π periodic. The tag position is represented by the orange lines on the x - and y -axes, while the size of the driven trajectory L_{SA} is indicated by the green dashed line.

value represents a measurement between a single antenna aperture position and a single tag. The classical approach is to apply a grid to the room and generate hypothetical phases for each grid point for each sample, that is, each antenna position, as seen in Figure 6 for the 3D case. The number of grid points depends on the desired resolution: the smaller the grid spacing, the better the theoretically attainable resolution as long as no other maximum-finding technique, such as a Parabel fit method, is used.

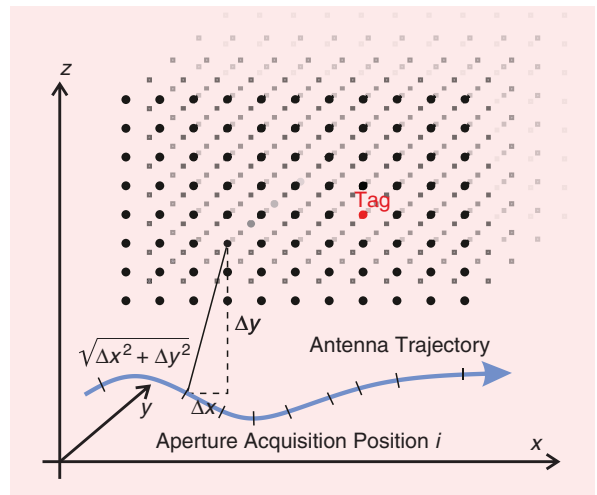


Figure 6. The steering point is calculated by knowing the exact position of the antenna. The procedure is repeated for every grid point chosen. The bigger the search space, the longer it takes to compute the steering vectors.

A grid spacing of 1 cm would lead to 62.5×10^6 hypothetical phase times $N \cdot K$ for each measurement, which corresponds to the proportional amount of needed calculations as they need to be complex conjugated and multiplied by the measured phases. A generalized solution was given by [49] and is adapted to

$$N_{\text{calc}} \sim N_{\text{Pixel},x} \cdot N_{\text{Pixel},y} \cdot N_{\text{Pixel},z} \cdot N_{\text{samples}} \cdot K. \quad (10)$$

The number of needed multiplications can be reduced by using DSP techniques, such as a variable grid search or a particle-based approach.

Variable Grid Search

The 3D case for a normal grid search is shown in Figure 6. Our variable grid search approach was performed as indicated in Figure 9. There are a few steps involved in searching for the steering vector that fits the position of the tag. In the first step, a widened grid spacing is used. At the estimated position on the grid that best matches the real position, which is where the maximal beamformer output power (5) occurs, a finer grid is applied, and the steering vector is recalculated. As the spatial sampling theorem is satisfied, there are no ambiguities in the position estimation. Depending on the desired resolution, the grid can always be refined or a Parabel fit for the maximum finding can be applied, which can significantly decrease the number of multiplications.

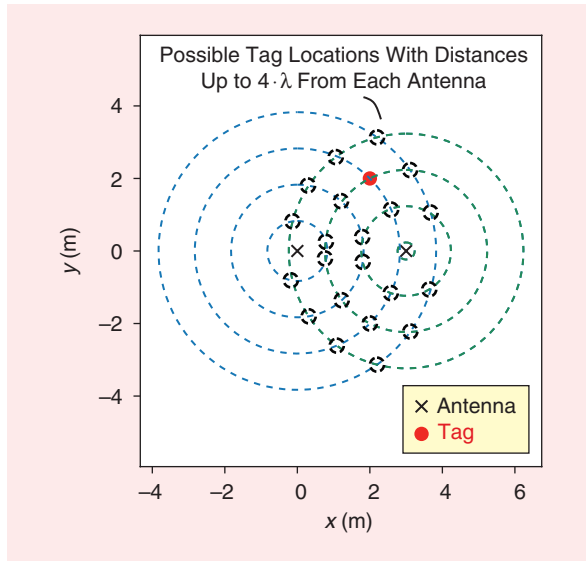


Figure 7. Two receiving antennas are placed at the coordinates (0, 0) and (3, 0). The reported phase is 2π -unambiguous, and the possible positions of the tags are thus endless. This example shows only the first four repetitions of the phase, in which the wavelength is assumed to be 1 m.

Particle Search

Another DSP technique that decreases the computation time is the particle-search algorithm. Figure 10 illustrates the basic concept [50]. The overall aperture spanned by the robot is divided into subapertures. In the very first step for the first aperture, a random set of particles with equal initial weights is generated for every particle. The weight is an indicator of the likeliness of a match to the actual position of the tag, that is, the correlation result. After the beamforming technique is applied for these particles, the weights of the particles are updated based on the evaluation of the beamformer, with the weight of the particles closer to the tag being higher than those far away.

For the next subaperture, the particles are resampled. This can be done in different ways. One way is to move the lowest weight particles to places with a higher probability of tag location. Another method removes low-weight particles and moves a reduced amount to the high-weight locations, thus decreasing the total number of particles, which, in turn, reduces the computational burden. The following steps are repeated for every further subaperture: predict the next positions of particles, update their weights, resample, and then evaluate the beamforming technique. Note that the computational effort is reduced to about 0.1% in comparison to a grid-based approach, while the localization accuracy is equal [50].

Measurement Setup

The measurement setup is assembled in such a way that it represents a test retail application in a warehouse.

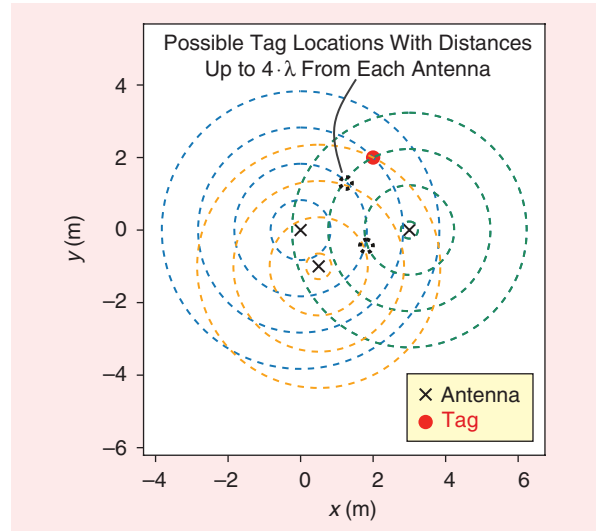


Figure 8. Three receiving antennas are placed at the coordinates (0, 0), (0.5, -1), and (3, 0). Clever placement of the antennas drastically reduces the possible tag positions due to the 2π periodicity. The figure shows only the first four repetitions of the reported phase, in which the wavelength is assumed to be 1 m.

Figure 2 illustrates the setting: eight antennas are mounted on a mobile robot pointing toward the tags, which are attached to plastic boxes with known locations. The antennas are located in the x - z plane with a circular polarization. The beamwidth of the antenna is about 70° with 7.5-dBi antenna gain, providing a total equivalent isotropically radiated power of 33 dBm. The size of the room is about $5\text{ m} \times 5\text{ m}$, and the room has multipath effects comparable to those in a warehouse.

The robot itself generates the synthetic aperture where all of the tags are in the read range of the antennas on every point on the trajectory; it also provides odometry data for reconstructing the approximate positions of the antennas. The antennas are connected to the COTS reader Sirit Infinity 610 via an antenna-switch matrix, which is needed because the reader provides only a bistatic channel configuration, that is, the transmitter and receiver antennas are connected to separate reader channels and thus enable a full eight-channel MIMO configuration.

The time needed for cycling through the different signal paths has to be considered in the robot movement velocity, which is set to 1 mm/s for this measurement. The reader's protocol settings are as follows: the uplink frequency is set to 866.3 MHz, the backscatter link frequency is set to 320 kHz, and the coding scheme is FM0. The communication is handled by a Python script

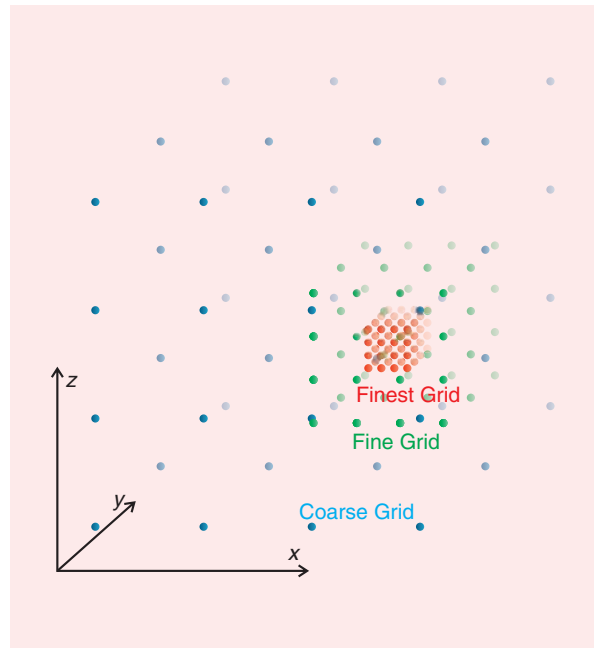


Figure 9. The variable grid search can be done in arbitrary steps. This example illustrates a three-stage control. The first stage is a coarse grid. At the most likely tag position, a finer grid is established, and the steering vectors are recalculated for the much smaller room area. Depending on the desired resolution, more stages can be added, as depicted in the figure. The finer grid is always applied to the most likely tag position.

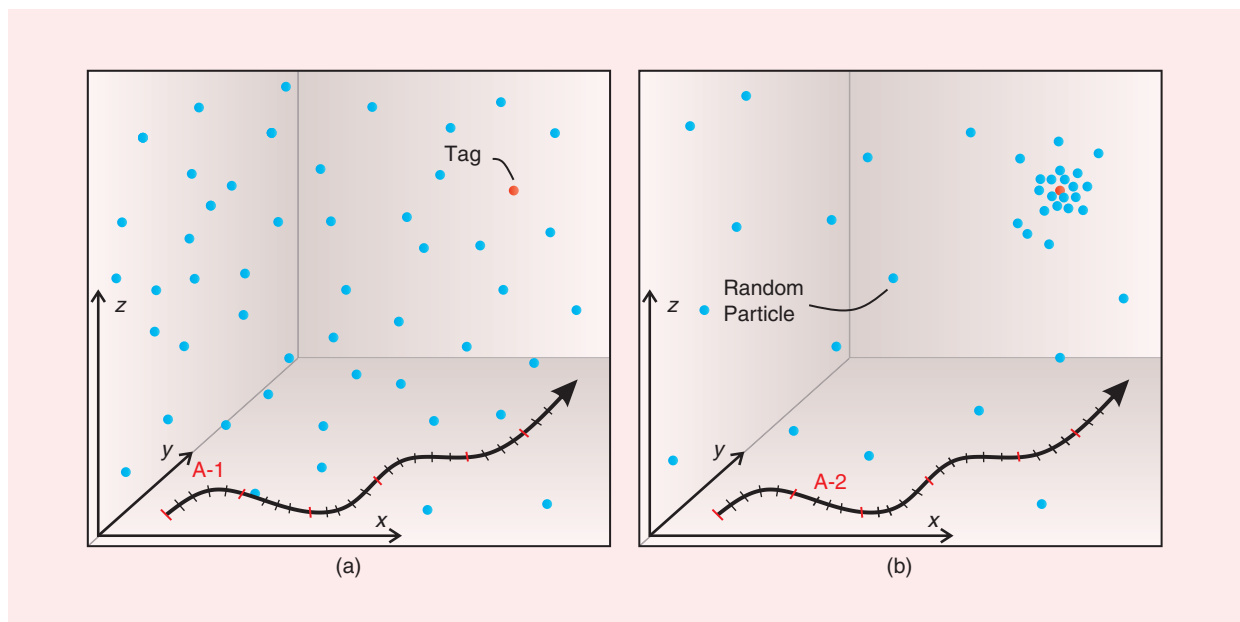


Figure 10. The total aperture is divided into the subapertures A-1, A-2, and so on. (a) In the first step and first aperture, the particles are generated randomly, namely, the blue dots. After applying and evaluating the beamformer at the particle positions, most particles are resampled to the most likely position of the tag, that is, the highest correlation between a random particle and the measured phase, which is shown as a red dot. Only a few are left in the rest of the room area of interest with lower weights than the particles closer to the tag position. (b) The more steps the algorithm performs, the more particles are generated close to the tag with increasing weight.

running on a computer placed on the robot. The data from the reader contain the tag ID, the received phase value, the switch configuration, (which is delivering the information of the active antennas), and a timestamp for



Figure 11. A mobile robot platform equipped with a UHF-RFID MIMO system and a computer generates an aperture, that is, a straight line of 3.2 m, along plastic boxes labeled with tags. The real tag positions are known and are compared to the estimated positions after the signal processing.

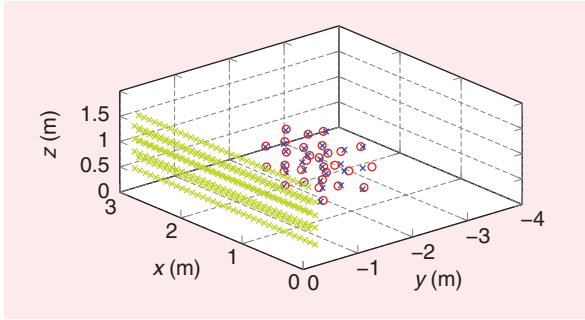


Figure 12. The position of 30 field tags mounted on plastic boxes is estimated. The aperture was driven 3.2 m along the x-axis. The blue “x” markers represent the real tag positions, the red circles show the estimated tag positions, and the lime “x” markers indicate the antenna positions along the aperture that were used in the localization algorithm.

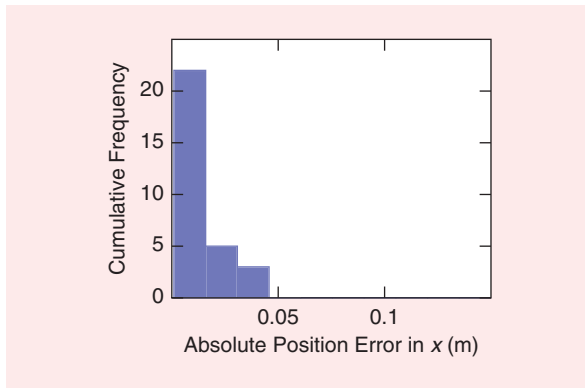


Figure 13. A histogram of the absolute position error in x directions of the localized tags.

each tag. The odometry data of the robot also contain a timestamp to synchronize the reader and robot data. It is important to guarantee timing synchronization because a wrong link between the odometry and tag data leads to wrong localization results, as the antenna positions would be assumed to be in the wrong positions for sending and receiving.

In our measurement scenario given in Figure 11, the robot path, namely, the aperture geometry, is a straight line of 3.2 m. Figure 12 depicts the evaluation of the standard SAR approach for a calibrated antenna array. The blue “x” markers represent the real tag positions, the red circles are the estimated positions for all 30 used tags, and the lime-colored “x” marks represent every thousandth antenna position to get an impression of the driving path. The localization accuracy is determined by

$$\text{RMSE} = \sqrt{\frac{1}{N_{\text{tags}}} \sum_{k=1}^{N_{\text{tags}}} \|\hat{r}_{\text{tag}}[k] - \tilde{r}_{\text{tag}}^{\text{ref}}[k]\|_2^2}, \quad (11)$$

where N_{tags} is the number of tags used (30 in this scenario).

An RMSE value of 0.054 m has been achieved. The mean errors for x, y, and z are shown in Figures 13–15.

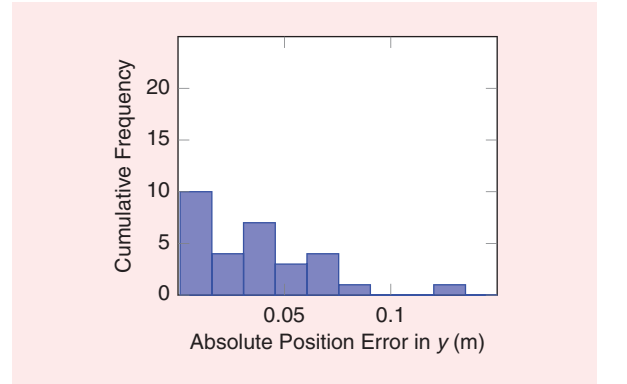


Figure 14. A histogram of the absolute position error in y directions of the localized tags.

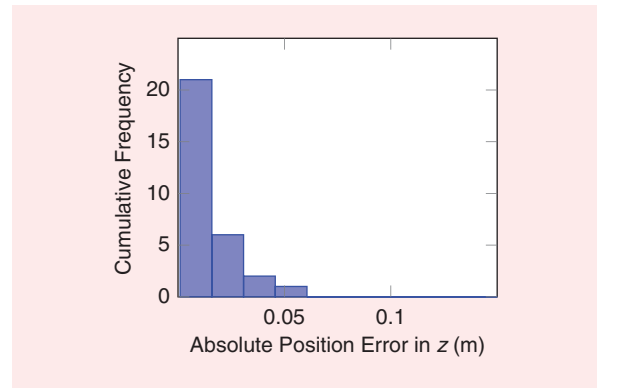


Figure 15. A histogram of the absolute position error in z directions of the localized tags.

The error in the x direction is the smallest due to the movement along the x -axis; accordingly, the y direction error is the biggest as there was no antenna movement on the y -axis at all. The total height of all of the mounted antennas was larger than 1 m, and the spacing was lower than one-half the wavelength, explaining the relatively small error for the z direction of the tags.

A real scenario is given in Figure 16 using the same system introduced in the test scenario, with 134 tags placed on articles of clothing. A comparison between the localization results in Figures 16 and 17 illustrates the good match between the geometry of the storing racks and the measured tag positions.

Conclusions

Presented here was comparison between different localization techniques for UHF-RFID tags focusing on a phase-based SAR approach. Measurement results were shown for an SAR scenario, in which a robot drove along an axis and tags were mounted on objects to be localized, as occurs, for example, in real warehouse environments. The presented algorithm, based on a grid-search beamformer, was able to locate tags with an RMSE of



Figure 16. A mobile robot platform equipped with a UHF-RFID MIMO system drives autonomously through a real warehouse scenario and streams the tag data to a computer, where the localization algorithm estimates the real tag positions.

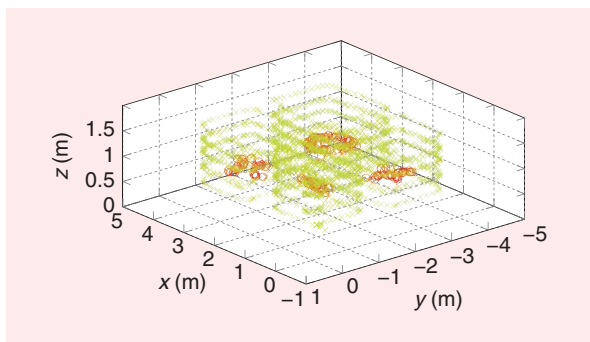


Figure 17. The position of 134 articles of clothing labeled with tags is estimated. The red circles represent the estimated tag positions, and the lime "x" markers represent the antenna positions along the aperture that are used in the localization algorithm.

0.054 m in an industrial environment, making it suitable for scenarios with even strong multipath influences. To lower the computational burden, grid refinement or particle-search implementation can be applied.

Acknowledgment

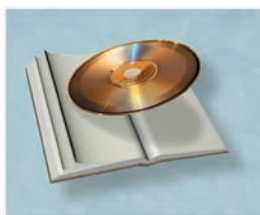
This work was funded by the Central Innovation Programme for SMEs (ZIM), Federal Ministry for Economic Affairs and Energy, Germany, grant ZF4226301PR6.

References

- [1] K. Finkenzeller, *RFID-Handbuch: Grundlagen und praktische Anwendungen von Transpondern, kontaktlosen Chipkarten und NFC*, 7. Auflage. Munich, Germany: Carl Hanser Verlag GmbH Co KG, Aug. 11, 2015.
- [2] A. Ghelichi and A. Abdelgawad, "A study on RFID-based Kanban system in inventory management," in *Proc. IEEE Int. Conf. Ind. Eng. Eng. Manag.*, Dec. 2014, pp. 1357–1361. doi: 10.1109/IEEM.2014.7058860.
- [3] E. Hidalgo, F. Muñoz, A. Guerrero de Mier, R. G. Carvajal, and R. Martín-Clemente, "Wireless inventory of traffic signs based on passive RFID technology," in *Proc. IECON - 39th Annu. Conf. IEEE Ind. Electron. Soc.*, Nov. 2013, pp. 5467–5471. doi: 10.1109/IECON.2013.6700026.
- [4] Y. Liang et al., "A method to make accurate inventory of smart meters in multi-tags group-reading environment," in *Proc. IEEE Int. Conf. RFID Technol. Appl. (RFID-TA)*, Sept. 2016, pp. 123–128. doi: 10.1109/RFID-TA.2016.7750743.
- [5] M. Hehn, E. Sippel, C. Carlowitz, and M. Vossiek, "High-accuracy localization and calibration for 5-DoF indoor magnetic positioning systems," *IEEE Trans. Instrum. Meas.*, vol. 68, no. 10, pp. 1–11, 2018. doi: 10.1109/TIM.2018.2884040.
- [6] V. Stanford, "Pervasive computing goes the last hundred feet with RFID systems," *IEEE Pervasive Comput.*, vol. 2, no. 2, pp. 9–14, Apr. 2003. doi: 10.1109/MPRV.2003.1203746.
- [7] "Class-1 Generation-2 UHF RFID Protocol for Communications at 860 MHz – 960 MHz," Version 2.0.1, Oct. 23, 2008. [Online]. Available: https://www.gs1.org/sites/default/files/docs/epc/Gen2_Protocol_Standard.pdf
- [8] U. Jyväskylä, Prognose zum weltweiten umsatz mit rfid-transpondern bis zum jahr 2020 (in milliarden us-dollar), Statista, Hamburg, Germany, 2019. [Online]. Available: <https://de.statista.com/statistik/daten/studie/295354/umfrage/umsatzprognose-auf-dem-weltmarkt-fuer-rfid-tags/>
- [9] J. Heidrich et al., "The roots, rules, and rise of RFID," *IEEE Microw. Mag.*, vol. 11, no. 3, pp. 78–86, May 2010. doi: 10.1109/MMM.2010.936075.
- [10] Impinj, "Low level user data support," Impinj, Seattle, WA, Sept. 2013. https://support.impinj.com/hc/en-us/article_attachments/200774268/SR_AN_IPJ_Speedway_Rev_Low_Level_Data_Support_20130911.pdf
- [11] A. Parr, R. Miesen, and M. Vossiek, "Comparison of phase-based 3d near-field source localization techniques for UHF RFID," *Sensors*, vol. 16, no. 7, p. 978, June 25, 2016. doi: 10.3390/s16070978.
- [12] J. L. Brchan, L. Zhao, J. Wu, R. E. Williams, and L. C. Pérez, "A real-time RFID localization experiment using propagation models," in *Proc. IEEE Int. Conf. RFID (RFID)*, Apr. 2012, pp. 141–148. doi: 10.1109/RFID.2012.6193042.
- [13] I. Kharrat, Y. Duroc, G. Andia Vera, M. Awad, S. Tedjini, and T. Aguilu, "Customized RSSI method for passive uhf RFID localization system," *J. Telecommun.*, vol. 10, no. 2, pp. 1–5, Sept. 2011.
- [14] M. Huchard, V. Paquier, A. Loeillet, V. Marangozov, and J. Nicolai, "Indoor deployment of a wireless sensor network for inventory and localization of mobile assets," in *Proc. IEEE Int. Conf. RFID-Technol. Appl. (RFID-TA)*, Nov. 2012, pp. 369–372. doi: 10.1109/RFID-TA.2012.6404548.

- [15] N. Decarli, "On phase-based localization with narrowband back-scatter signals," *EURASIP J. Adv. Signal Process.*, vol. 2018, no. 1, p. 70, Nov. 12, 2018. doi: 10.1186/s13634-018-0590-4.
- [16] S. Gakhar, J. Feldkamp, M. Perkins, R. Sun, and C. J. Reddy, "Engineering RFID systems through electromagnetic modeling," in *Proc. IEEE Int. Conf. RFID*, Apr. 2008, pp. 344–349. doi: 10.1109/RFID.2008.4519346.
- [17] V. Viikari, P. Pursula, and K. Jaakkola, "Ranging of UHF RFID tag using stepped frequency read-out," *IEEE Sensors J.*, vol. 10, no. 9, pp. 1535–1539, Sept. 2010. doi: 10.1109/JSEN.2010.2045497.
- [18] Frenzel and Koch, "Modeling the effect of human body on TOA ranging for indoor human tracking with wrist mounted sensor," in *Proc. 16th Int. Symp. Wireless Personal Multimedia Commun. (WPMC)*, June 2013, pp. 1–6.
- [19] C. Li, L. Mo, and X. Xie, "Localization of passive UHF RFID tags on assembly line based on phase difference," in *Proc. IEEE Int. Instrum. Meas. Technol. Conf.*, May 2016, pp. 1–6. doi: 10.1109/I2MTC.2016.7520577.
- [20] Y. Ma, K. Pahlavan, and Y. Geng, "Comparison of POA and TOA based ranging behavior for RFID application," in *Proc. IEEE 25th Annu. Int. Symp. Personal, Indoor, Mobile Radio Commun. (PIMRC)*, Sept. 2014, pp. 1722–1726. doi: 10.1109/PIMRC.2014.7136446.
- [21] X. Li, Y. Zhang, and M. Amin, "Multifrequency-based range estimation of RFID tags," in *Proc. IEEE Int. Conf. RFID*, Orlando, FL, Apr. 2009, pp. 147–154. doi: 10.1109/RFID.2009.4911199.
- [22] M. Scherhäufl, M. Pichler, D. Müller, A. Ziroff, and A. Stelzer, "Phase-of-arrival-based localization of passive UHF RFID tags," in *Proc. IEEE MTT-S Int. Microw. Symp. Dig. (MTT)*, June 2013, pp. 1–3. doi: 10.1109/MWSYM.2013.6697558.
- [23] M. Scherhäufl, M. Pichler, E. Schimbäck, D. J. Müller, A. Ziroff, and A. Stelzer, "Indoor localization of passive UHF RFID tags based on phase-of-arrival evaluation," *IEEE Trans. Microw. Theory Techn.*, vol. 61, no. 12, pp. 4724–4729, Dec. 2013.
- [24] M. Wegener, D. Froß, M. Rößler, C. Drechsler, C. Pätz, and U. Heinke, "Relative localisation of passive UHF-tags by phase tracking," in *Proc. 13th Int. Multi-Conf. Syst., Signals Devices (SSD)*, Mar. 2016, pp. 503–506. doi: 10.1109/SSD.2016.7473683.
- [25] A. Parr, R. Miesen, and M. Vossiek, "Inverse SAR approach for localization of moving RFID tags," in *Proc. IEEE Int. Conf. RFID (RFID)*, Apr. 2013, pp. 104–109. doi: 10.1109/RFID.2013.6548142.
- [26] A. Buffi, P. Nepa, and F. Lombardini, "A phase-based technique for localization of UHF-RFID tags moving on a conveyor belt: Performance analysis and test-case measurements," *IEEE Sensors J.*, vol. 15, no. 1, pp. 387–396, Jan. 2015. doi: 10.1109/JSEN.2014.2344713.
- [27] J. Huiting, A. B. J. Kokkeler, and G. J. M. Smit, "Near field phased array DOA and range estimation of UHF RFID tags," in *Proc. Int. EURASIP Workshop RFID Technol. (EURFID)*, Oct. 2015, pp. 103–107. doi: 10.1109/EURFID.2015.7332393.
- [28] S. Li, B. Lin, B. Li, and R. He, "Near field sources localization based on robust propagator method," in *Proc. IEEE Int. Conf. RFID Technol. Appl. (RFID-TA)*, Sept. 2018, pp. 1–6. doi: 10.1109/RFID-TA.2018.8552790.
- [29] N. Honma, K. Toda, and Y. Tsunekawa, "DoA estimation technique of back-scattering signal from RFID for gesture recognition," in *Proc. 9th Eur. Conf. Antennas Propag. (EuCAP)*, Apr. 2015, pp. 1–2.
- [30] P. V. Nikitin, R. Martinez, S. Ramamurthy, H. Leland, G. Spiess, and K. V. S. Rao, "Phase based spatial identification of UHF RFID tags," in *Proc. IEEE Int. Conf. RFID (IEEE RFID 2010)*, Apr. 2010, pp. 102–109. doi: 10.1109/RFID.2010.5467253.
- [31] Z. Chen, G. Gokeda, and Y. Yu, *Introduction to Direction-of-arrival Estimation*. Norwood, MA: Artech House, 2010, p. 196.
- [32] I. Ziskind and M. Wax, "Maximum likelihood localization of multiple sources by alternating projection," *IEEE Trans. Acoust., Speech, Signal Process.*, vol. 36, no. 10, pp. 1553–1560, Oct. 1988. doi: 10.1109/29.7543.
- [33] F. Schwegge, "Sensor-array data processing for multiple-signal sources," *IEEE Trans. Inf. Theory*, vol. 14, no. 2, pp. 294–305, Mar. 1968. doi: 10.1109/TIT.1968.1054121.
- [34] H. Krim and M. Viberg, "Two decades of array signal processing research: The parametric approach," *IEEE Signal Process. Mag.*, vol. 13, no. 4, pp. 67–94, July 1996. doi: 10.1109/79.526899.
- [35] M. Scherhäufl, M. Pichler, and A. Stelzer, "UHF RFID localization based on evaluation of backscattered tag signals," *IEEE Trans. Instrum. Meas.*, vol. 64, no. 11, pp. 2889–2899, Nov. 2015. doi: 10.1109/TIM.2015.2440554.
- [36] M. Scherhaeufl, M. Pichler, and A. Stelzer, "Maximum likelihood position estimation of passive UHF RFID tags based on evaluation of backscattered transponder signals," in *Proc. IEEE Topical Conf. Wireless Sensors and Sensor Netw. (WiSNet)*, Jan. 2016, pp. 24–26. doi: 10.1109/WISNET.2016.7444312.
- [37] G. Bienvenu and L. Kopp, "Adaptivity to background noise spatial coherence for high resolution passive methods," in *Proc. ICASSP '80. IEEE Int. Conf. Acoust., Speech, Signal Process.*, Apr. 1980, vol. 5, pp. 307–310. doi: 10.1109/ICASSP.1980.1171029.
- [38] R. Schmidt, "Multiple emitter location and signal parameter estimation," *IEEE Trans. Antennas Propag.*, vol. 34, no. 3, pp. 276–280, Mar. 1986. doi: 10.1109/TAP.1986.1143830.
- [39] R. Roy and T. Kailath, "ESPRIT-estimation of signal parameters via rotational invariance techniques," *IEEE Trans. Acoust., Speech, Signal Process.*, vol. 37, no. 7, pp. 984–995, July 1989. doi: 10.1109/29.32276.
- [40] R. T. L. Peñas and J. C. D. Cruz, "Accuracy improvement of ESPRIT-extracted direction-of-arrival estimates using least mean-squares filter for passive RFID inventory application," in *Proc. Int. Conf. Humanoid, Nanotechnol., Inform. Technol., Commun. Control, Environ. Manag. (HNICEM)*, Dec. 2015, pp. 1–6. doi: 10.1109/HNICEM.2015.7393216.
- [41] J. Capon, "High-resolution frequency-wavenumber spectrum analysis," *Proc. IEEE*, vol. 57, no. 8, pp. 1408–1418, Aug. 1969. doi: 10.1109/PROC.1969.7278.
- [42] T. Faseth, M. Winkler, H. Arthaber, and G. Magerl, "The influence of multipath propagation on phase-based narrowband positioning principles in UHF RFID," in *Proc. IEEE-APS Topical Conf. Antennas Propag. Wireless Commun.*, Sept. 2011, pp. 1144–1147. doi: 10.1109/APWC.2011.6046829.
- [43] G. Li, D. Arnitz, R. Ebel, U. Muehlmann, K. Witrisal, and M. Vossiek, "Bandwidth dependence of CW ranging to UHF RFID tags in severe multipath environments," in *Proc. IEEE Int. Conf. RFID*, Apr. 2011, pp. 19–25. doi: 10.1109/RFID.2011.5764631.
- [44] R. Miesen et al., "Where is the tag?" *IEEE Microw. Mag.*, vol. 12, no. 7, pp. S49–S63, Dec. 2011. doi: 10.1109/MMM.2011.942730.
- [45] K. P. Ray, R. K. Kulkarni, and B. K. Ramkrishnan, "DOA estimation in a multipath environment using covariance differencing and iterative forward and backward spatial smoothing," in *Proc. Int. Conf. Recent Adv. Microw. Theory Appl.*, Nov. 2008, pp. 794–796. doi: 10.1109/AMTA.2008.4763086.
- [46] K. Sekine, N. Kikuma, H. Hirayama, and K. Sakakibara, "DOA estimation using spatial smoothing with overlapped effective array aperture," in *Proc. Asia Pacific Microw. Conf.*, Dec. 2012, pp. 1100–1102. doi: 10.1109/APMC.2012.6421837.
- [47] G. Hislop and C. Craeye, "Spatial smoothing for 2d direction finding with passive RFID tags," in *Proc. Loughborough Antennas Propag. Conf.*, Nov. 2009, pp. 701–704. doi: 10.1109/LAPC.2009.5352444.
- [48] M. Vossiek, A. Urban, S. Max, and P. Gulden, "Inverse synthetic aperture secondary radar concept for precise wireless positioning," *IEEE Trans. Microw. Theory Techn.*, vol. 55, no. 11, pp. 2447–2453, Nov. 2007. doi: 10.1109/TMTT.2007.908668.
- [49] R. Miesen, F. Kirsch, and M. Vossiek, "UHF RFID localization based on synthetic apertures," *IEEE Trans. Autom. Sci. Eng. (from July 2004)*, vol. 10, no. 3, pp. 807–815, July 2013. doi: 10.1109/TASE.2012.2224656.
- [50] G. Li, R. Ebel, and M. Vossiek, "Particle filter based synthetic aperture reconstruction approach for real-time 3d wireless local positioning," in *Proc. 7th German Microw. Conf.*, Mar. 2012, pp. 1–4.





Book/Software Reviews

A Must-Have Reference on Antenna Technology

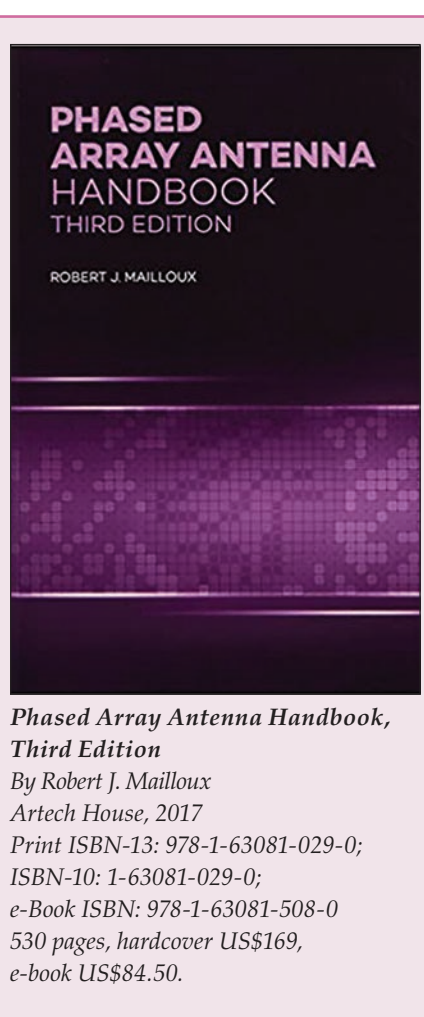
■ James Chu

Dr. Robert J. Mailloux received his Ph.D. degree in applied physics from Harvard University in 1965. He worked with NASA's Electronics Research Center and then with the U.S. Air Force Research Laboratory system, retiring in 2004. Dr. Mailloux also served as a research professor at the University of Massachusetts Amherst and as an adjunct professor at Northeastern University and the U.S. Air Force Institute of Technology. He is a Fellow of IEEE and a member of the IEEE Antennas and Propagation Society and IEEE Microwave Theory and Techniques Society. His research interests are antenna theory, periodic structures, arrays, and subarray techniques. He has received many IEEE awards and other distinctions, and he is an honorary professor at the University of Trento, Italy.

Phased Array Antenna Handbook is intended to provide a collection of design data for radar and communication system and array designers. As such,

James Chu (james.cc.chu@ieee.org), IEEE Senior Life Member, is an RF engineering consultant.

Digital Object Identifier 10.1109/MMM.2020.3042040
Date of current version: 3 February 2021



Phased Array Antenna Handbook, Third Edition

By Robert J. Mailloux
Artech House, 2017

Print ISBN-13: 978-1-63081-029-0;

ISBN-10: 1-63081-029-0;

e-Book ISBN: 978-1-63081-508-0

530 pages, hardcover US\$169,

e-book US\$84.50.

it only briefly addresses the details of electromagnetic analysis. Additional materials in this third edition include the areas of fabrication and computation, addressing array control, RF circuitry, and array elements on the same substrate or even incorporated into monolithic microwave integrated circuit packaging. This edition also introduces recent changes in fabrication capability, describing the huge impact of high-performance computational tools on antenna technology—from element design to synthesis.

Chapter 1, “Phased Arrays in Radar and Communication Systems,” emphasizes array selection and highlights those parameters that determine the fundamental measurable properties of arrays (including gain, beamwidth, bandwidth, size, polarization, and grating lobe radiation) and also the tradeoff between passive and active arrays. In addition, this chapter discusses arrays with phase shifters or with time-delay control as well as analog, digital, and hybrid beamforming.

Chapter 2, “Pattern Characteristics of Linear and Planar Arrays,” describes the fundamental definitions of radiation integrals and examines many of the important issues in array design,

including the mutual coupling effects of the element pattern. Another major subject is thinned arrays related to probabilistic, peak sidelobe, and quantized amplitude distributions.

Chapter 3, “Pattern Synthesis for Linear and Planar Arrays,” is a brief treatment of array synthesis. It lists basic formulas and references on a wide variety of techniques for producing low-sidelobe or slot antenna patterns, such as Dolph–Chebyshev synthesis, Taylor line-source synthesis, Bayliss line-source difference patterns, and Elliott’s modified Taylor patterns. The chapter also includes a discussion of pattern optimization techniques, such as those for adaptive array antennas, as well as generalized patterns using covariance matrix inversion.

Chapter 4, “Patterns of Nonplanar Arrays,” covers arrays on nonplanar surfaces, such as those on circular and cylindrical arrays, and the patterns of elements and arrays on conducting cylinders. It also briefly introduces spherical, hemispherical, and truncated conical arrays.

Chapter 5, “Elements for Phased Arrays,” starts with wire antenna elements and then moves on to dipoles and monopoles. The discussion of dipoles also includes bowtie and microstrip dipoles and microstrip patch elements. The chapter continues with coverage of slot antenna elements, Vivaldi arrays, and bunny ear antennas. At the end of this chapter, the author discusses the elements and polarizers used for polarization diversity. He

gives five examples of elements for radiating circular polarization and describes the elements of polarization grid sheets.

Chapter 6, “Summary of Element Pattern and Mutual Impedance Effects,” discusses some of the effects of mutual coupling among array elements. This interaction modifies the active array element patterns and can cause a significant change in impedance with a scan of finite and infinite scanning arrays. The final section covers several useful simulators.

Chapter 7, “Array Error Effects,” describes pattern distortion caused by random phase and amplitude errors at the array elements and phase and

amplitude quantization across the array. All of the correlated errors can be removed, and the remaining residual, uncorrelated phase and amplitude errors can be treated as random and residual (average) sidelobe errors estimated by statistical procedures.

Chapter 8, “Multiple Beam Antennas,” summarizes techniques for three kinds of special-purpose, multiple-beam array systems. It discusses orthogonality loss, the Stein limit, the multiple-beam lens, and reflector systems.

Finally, Chapter 9, “Special Arrays for Limited Field-of-View and Wideband Coverage,” discusses a specialized group of array systems that take advantage of restrictions in the scan coverage to produce a very-high-gain scanning system. Many of these systems are based on the multiple-beam properties of reflectors and lens systems. Numerous real-world examples are included.

Overall, this book is the bible of array antenna design, development, and research and a must-have reference for those pursuing higher education in antenna technology. Unfortunately for such a valuable resource, this third edition could use a good proofreading.



Chapter 8 summarizes techniques for three kinds of special-purpose, multiple-beam array systems.

Errata

Due to a copyediting error, on page 23 of [1], the acronym “TEM” was spelled

out incorrectly. The correct term is “transverse electromagnetic.” We apologize for any confusion this may have caused.

Reference

- [1] S. Bastioli and R. V. Snyder, “Nonresonating modes do it better!” *IEEE Microw. Mag.*, vol. 22, no. 1, pp. 20–45, Jan. 2021. doi: 10.1109/MMM.2020.3027934.

Digital Object Identifier 10.1109/MMM.2020.3046119

Date of current version: 3 February 2021



Health Matters

Sonic Health Attacks by Pulsed Microwaves in Havana Revisited

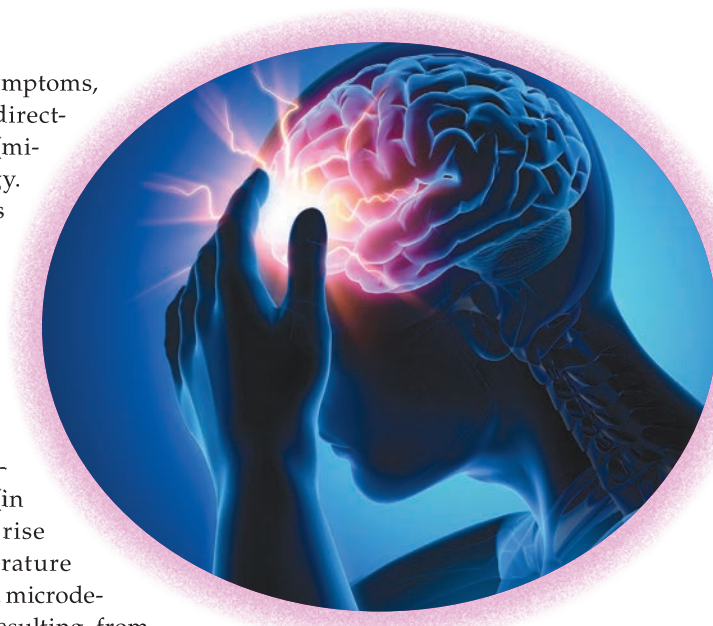
■ James C. Lin

The U.S. National Academies of Sciences, Engineering, and Medicine (NASEM) recently released its study report “An Assessment of Illness in U.S. Government Employees and Their Families at Overseas Embassies” [1]. As I write this in December 2020, it is almost exactly three years since the publication of my article “Strange Reports of Weaponized Sound in Cuba” [2]. There, it was first hypothesized that “[a]ssuming that the reported events are reliable, there is actually a scientific explanation for the source of sonic energy. It could well be from a targeted beam of high-power microwave pulse radiation” [2].

In examining plausible causes of the described illnesses, the NASEM report [1] makes that point that, among the mechanisms the study committee considered, the most plausible mechanism to explain these cases, especially in individuals with

distinct early symptoms, appears to be directed, pulsed RF (microwave) energy. The hypothesis of the microwave auditory effect [2] was based on years of published laboratory and theoretical research. A minuscule but rapid (in microseconds) rise in tissue temperature (on the order of a microdegree Celsius), resulting from the absorption of pulsed microwave energy, creates a thermoelastic expansion of brain matter. This small, theoretical elevation is hardly detectable by any currently available temperature sensors, let alone felt as a thermal sensation or heat. Nevertheless, it can launch an acoustic wave of pressure that travels inside the head to the inner ear. There, it activates the hair-cell nerves in the cochlea, which then relay it to the central auditory system for perception via the same

process involved in normal sound hearing [3]–[5]. Depending on the power of the impinging microwave pulses, the level of induced sound pressure could be considerably above the threshold of auditory perception at the cochlea—approaching or exceeding levels of discomfort (including the reported headaches, ringing in the ears, nausea, and problems with balance or vertigo) and even causing potential brain-tissue injury.



©SHUTTERSTOCK.COM/PETERSCHREIBER MEDIA

James C. Lin (lin@uic.edu) is with the University of Illinois, Chicago, Illinois, 60607, USA.

Digital Object Identifier 10.1109/MMM.2020.3044125
Date of current version: 3 February 2021

It is important to note that recent clinical magnetic resonance imaging (MRI) examinations of brains of personnel in Havana, compared to those of individuals not experiencing the loud bursts of sound, revealed significant differences in whole-brain white matter volume, regional gray and white matter volumes, cerebellar tissue microstructural integrity, and functional connectivity in the auditory and visuospatial subnetworks but not in the executive control subnetwork [6]. However, the clinical importance of these disparities is not definitive. A high-power, microwave-pulse-generated acoustic pressure wave can be initiated in the brain and then reverberate inside the head, potentially reinforcing the initial pressure and causing injury to the brain matters [5].

Furthermore, while the clinical symptoms presented are concussion like, the MRI images did not resemble the usual presentations of traumatic brain injury or concussion. However, clinical experiences with concussion are derived mostly from externally inflicted impact wounds, such as a blow to the head when hitting the ground or another rigid body, which may set brain tissues into violent motion against the skull. A high-power, microwave-pulse-generated acoustic pressure wave could be initiated in the brain and then resonate inside the

head (see the results of the computer simulations in [5]), potentially reinforcing the initial pressure and resulting in injury to the brain matter. Thus, it is conceivable that the MRI images associated with high-power, microwave-induced pressure or shock waves may indicate entirely different manifestations of the brain injury or concussion. The clinical importance of these differences is uncertain at present and may command future study for clarification.

The known near-zone thresholds determined under controlled laboratory conditions for the peak microwave power density of auditory perception in human subjects with normal hearing are listed in Table 1. Note that, while there are wide variations in measured threshold values over the range of 1–70 μ s of pulsewidths involved, the subset of data for 10–32 μ s falls within a narrower range. Considering that the ambient noise levels in all three experiments were essentially the same, it may be reasonable to conclude that the averaged threshold power densities of 2.1–40 kW/m^2 , or 14 kW/m^2 , is a realistic threshold peak power density for the induction of the microwave auditory effect in the near field of 1,250–3,000-MHz microwaves with pulsewidths between 10 and

30 μ s. In other words, the 14- kW/m^2 -per-pulse peak power density generates a barely audible sound level of 0 dB. Generating sound at 60 dB (the audible level for normal conversation) requires a 1,000-fold higher power density per

pulse. To generate a tissue-injuring level of sound at 120 dB would take another 1,000-fold increase in required peak power density, or 14 GW/m^2 per pulse. The corresponding theoretical temperature elevation would

be about 1 $^{\circ}\text{C}$, which is safe by current protection guidelines.

For plane-wave equivalent exposures, the available computations provide two sets of data that are suitable for comparison with the results described previously. In one case, the reported threshold peak incident power density for an anatomical head model is 3 kW/m^2 for 20- μ s pulses at 915 MHz [11]. For the other, the threshold is about 50 kW/m^2 for 20- μ s pulses at 2,450 MHz [12]. The corresponding peak incident power densities at the 120-dB injury level are therefore between 3 and 50 GW/m^2 per pulse, which bracket the value of 14 GW/m^2 per pulse from the previous calculation for near-zone exposures. These peak power densities are close to and encompass the 23.8- GW/m^2 value for the dielectric breakdown of air. As the dielectric permittivity of all biological and physical materials is greater than that of air or free space, their intrinsic impedances are always smaller than that of air. The breakdown peak power density in skin, muscle, and brain tissues, for example, would be a factor of six to seven higher, or 142–166 GW/m^2 for a microwave pulse at 1,000–3,000 MHz.

Thus, if the microwave auditory effect is weaponized at sufficiently high powers for either lethal or nonlethal applications, the pulses are likely to injure the brain or auditory pathway nervous tissues through the reverberating sonic shock waves. The damage

Thus, the pulses may approach or exceed levels of discomfort or result in brain-tissue injury.

TABLE 1. Thresholds of microwave-induced auditory sensation in adult humans with normal hearing determined in controlled laboratory studies.

Frequency (MHz)	Pulsewidth (μ s)	Peak Power Density (kW/m^2)	Ambient Noise Level (dB)	Reference
1,245	10–70	0.9–6.3	45*	[7]
2,450	1–32	12.5–400	45	[8], [9]
3,000	10–15	2.25–20	45**	[10]
Pulsewidth Between 10 and 32 μs				
1,245	10–30	2.1–6.3	45*	[7]
2,450	10–32	12.5–40	45	[8], [9]
3,000	10–15	2.25–20	45**	[10]

*Typical sound pressure level for microwave anechoic chambers lined with absorbing materials.
 **With plastic foam earmuffs.

would not be caused by microwave pulse-induced hyperthermia through excessive temperature elevation in the brain or by a dielectric breakdown of brain, muscle, or skin tissues. Note that the units of measure of kW/m² or GW/m² per pulse refer to power per square meter, not the total output power of any source. In summary, depending on the power of the impinging microwave pulses, the level of induced sound pressure in the brain could be considerably higher than the threshold of auditory perception. Thus, the pulses may approach or exceed levels of discomfort or result in brain-tissue injury. A high-power, microwave-pulse-generated acoustic pressure wave initiated in the brain and reverberating inside the head could bolster the initial pressure and cause damage to the brain matters.

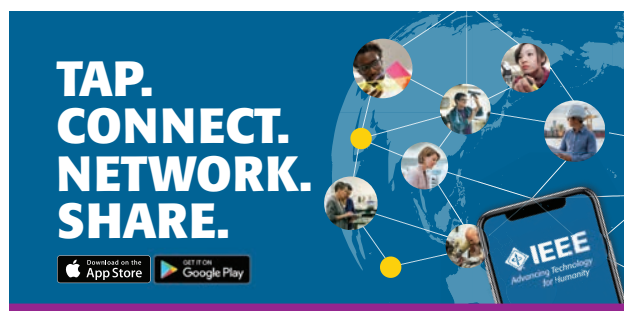
Postscript

The author of this article was invited by the NASEM study committee to present on “Multidisciplinary Analysis of Microwave Pulse-Induced Sound and Pressure in Human Heads.” The talk was based on his extensive research on the microwave auditory effect.







References

- [1] R. A. Relman and J. A. Pavlin, “An assessment of illness in U.S. government employees and their families at overseas embassies,” National Academies Press, Washington, D.C., Dec. 2020. [Online]. Available: <https://www.nationalacademies.org/news/2020/12/new-report-assesses-illnesses-among-us-government-personnel-and-their-families-at-overseas-embassies>
- [2] J. C. Lin, “Strange reports of weaponized sound in Cuba,” *IEEE Microw. Mag.*, vol. 19, no. 1, pp. 18–19, Jan. 2018.
- [3] J. C. Lin, “The microwave auditory phenomenon,” *Proc. IEEE*, vol. 68, no. 1, pp. 67–73, doi: 10.1109/PROC.1980.11583.
- [4] J. C. Lin and Z. W. Wang, “Hearing of microwave pulses by humans and animals: Effects, mechanism, and thresholds,” *Health Phys.*, vol. 92, no. 6, pp. 621–628, June 2007. doi: 10.1097/01.HP.0000250644.84530.e2.

- [5] J. C. Lin and Z. W. Wang, “Acoustic pressure waves induced in human heads by RF pulses from high-field MRI scanners,” *Health Phys.*, vol. 98, no. 4, pp. 603–613, 2010. doi: 10.1097/HP.0b013e3181c829b5.
- [6] R. Verma et al., “Neuroimaging findings in US government personnel with possible exposure to directional phenomena in Havana, Cuba,” *JAMA*, vol. 322, no. 4, pp. 336–347, 2019. doi: 10.1001/jama.2019.9269.
- [7] A. H. Frey and R. Messenger Jr., “Human perception of illumination with pulsed ultrahigh-frequency, electromagnetic energy,” *Science*, vol. 181, no. 4097, pp. 356–358, 1973. doi: 10.1126/science.181.4097.356.
- [8] A. W. Guy, C. K. Chou, J. C. Lin, and D. Christensen, “Microwave induced acoustic effects in mammalian auditory systems and physical materials,” *Ann. NY Acad. Sci.*, vol. 247, pp. 194–218, Feb. 1975. doi: 10.1111/j.1749-6632.1975.tb35996.x.
- [9] A. W. Guy, J. C. Lin, and C. K. Chou, “Electrophysiological effects of electromagnetic fields on animals,” in *Fundamentals and Applied Aspects of Nonionizing Radiation*. New York: Plenum Press, 1975, pp. 167–211.
- [10] C. A. Cain and W. J. Rissman, “Mammalian auditory response to 3.0 GHz microwave pulses,” *IEEE Trans. Biomed. Eng.*, vol. BME-25, no. 3, pp. 288–293, 1978. doi: 10.1109/TBME.1978.326343.
- [11] Y. Watanabe, T. Tanaka, M. Takai, and S. I. Watanabe, “FDTD analysis of microwave hearing effect,” *IEEE Trans. Microw. Theory Techn.*, vol. 48, no. 11, pp. 2126–2132, 2000. doi: 10.1109/22.884204.
- [12] N. M. Yitzhak, R. Rupp, and R. Hareuveni, “Numerical simulation of pressure waves in the cochlea induced by a microwave pulse,” *Bioelectromagnetics*, vol. 35, no. 7, pp. 491–496, 2014. doi: 10.1002/bem.21869.

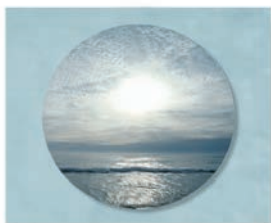


Connect to IEEE—no matter where you are—with the IEEE App.

-  Stay up-to-date with the latest news
-  Schedule, manage, or join meetups virtually
-  Get geo and interest-based recommendations
-  Read and download your IEEE magazines
-  Create a personalized experience
-  Locate IEEE members by location, interests, and affiliations

Download Today!





In Memoriam

George Matthaei

Dr. George Matthaei was a true pioneer in the development of microwave technology. He got involved in the days when generating a 1-GHz signal was almost science fiction. Throughout his career, he made major contributions in academia and industry. Dr. Matthaei died on 20 October 2020 at the age of 97.

Born in Tacoma, Washington, Dr. Matthaei showed an early interest in aeronautics, and in his teens he won prizes for his model airplane designs. After graduating high school in 1941, he attended the University of Washington, Seattle, and studied aeronautical engineering until April 1943. At that time, he was called up to active duty in the army during World War II. His career in microwave technology came about in a fortuitous manner. He was separated from his unit due to an illness. When he recovered, his unit had already shipped out, so he was assigned to an antiaircraft unit in the South Pacific. That unit had a radar. He appointed himself to work on the radar and learned the details of the system and electronics by reading the



Dr. George Matthaei, 1923–2020.

manuals by flashlight while on nighttime standby duty.

After the war, he returned to school and received his B.S. degree from the University of Washington in 1948. He went on to attain his master's degree, professional engineering degree, and Ph.D. degree from Stanford University in 1952. Then, for several years, he taught at the University of California at Berkeley until 1955. His specialty was network synthesis, which supported his interest in microwaves.

Deciding to branch out, Dr. Matthaei took an industrial leave of absence for a position at the Ramo-Wooldridge Corporation (later to become TRW). There, he performed system analysis and research on microwave components. He later joined

the Stanford Research Institute (SRI), where he participated in writing a book on microwave filters for the U.S. Army Signal Corps. The end result of this effort was the publication of *Microwave Filters, Impedance-Matching Networks, and Coupling Structures* (McGraw-Hill, 1964). This book, written in collaboration with Dr. Seymour Cohn, is a classic and can be found on the shelf of almost every microwave engineer. In 1962, Dr. Matthaei was promoted to manager of the Electromagnetics Techniques Laboratory at SRI.

In July 1964, he joined the Department of Electrical Engineering, University of California at Santa Barbara, as a professor. In July 1991, he retired as a professor emeritus and joined the staff of Superconductor Technologies Inc., Santa Barbara, California, working on a part-time basis until he was 85.

Aside from *Microwave Filters, Impedance-Matching Networks, and Coupling Structures*, he authored or coauthored numerous papers and was a contributor to several other books. Dr. Matthaei received the 1961 IEEE Microwave Theory and Techniques Society (MTT-S) Microwave Prize and the 1986 MTT-S Microwave Career Award. He was a Fellow of IEEE and a member of Sigma Xi and Tau Beta Pi.

Dr. Matthaei's relaxation was in the outdoors. He met his wife, Jean, while on a Sierra Club pack trip, and they

Compiled by Jerry Hausner (jhausner@aol.com), IEEE Microwave Theory and Techniques Society Memorials Committee chair.

Digital Object Identifier 10.1109/MMM.2020.3042032
Date of current version: 3 February 2021

married in June 1953. Once their daughters, Janie and Susie, were born, Dr. Matthaei and Jean introduced them to hiking early by carrying them as babies in an early model of a backpack baby carrier. Sunday afternoon hikes to explore the wilds of California were a regular part of Dr. Matthaei's family life for decades. Once Susie and Janie were grown up and had families of their own, summer trips to Mammoth Mountain for hiking became a tradition for the next 20 years, even as mobility for Jean and Dr. Matthaei became more difficult in their late 80s. There is a classic picture of Dr. Matthaei heading uphill on a trail near Mammoth while assisting Jean's walker with a

rope pull of his own construction! In addition, Dr. Matthaei, along with his wife, volunteered as docents at the Santa Barbara Museum of Natural History, sharing their mutual passion for nature and science.

California was Dr. Matthaei's adopted home, but, until health issues began to limit his travels, he made a point of returning to Washington every summer with Jean and the children. Both daughters have fond memories of visits with cousins, aunts, uncles, and grandparents; rides on ferries and other boats to explore Puget Sound; and trips to Mt. Rainier, the Cascades, the Olympic Peninsula, and the San Juan Islands.

Dr. Matthaei is survived by his daughters, Jane Bell (Douglas) and Susan Larsen (James); grandchildren, Laura and Lisa Bell, Rebecca Wendlandt (Jansen), and Matthew Larsen (Jennifer); and great grandchildren, Taevyn and Daylen Wendlandt and Gunnar Larsen.

Acknowledgments

Much of the information was provided by Dr. George Matthaei himself and his daughter Jane Matthaei Bell. Additional sources were Adelaide Payne of the *Microwave Journal* staff and MTT-S Ombuds Officer Ed Niehenke.



From the Editor's Desk *(continued from page 5)*

expanding the material into a series of articles that can be made into a focus issue for the magazine. Of course, we are always looking for review or tutorial articles, so, if you have an idea for an article, please contact me at microwave.editor@ieee.org.

Keeping with the technical theme of the March issue, we have another "Microwave Bytes" column from Dr. Steve Cripps, who takes a look at transmission line couplers and provides insight into their operation and fabrication (or, possibly, their fabrication impossibility). In spite of the pandemic and associated cessation of all but the most important travel, there is still significant activity besides just virtual conferences in the MTT-S's MHz to THz community. This month,

MTT-S President Dr. Greg Lyons introduces several new members of the MTT-S Administrative Committee; check out his column to learn about these new members and their perspectives on the direction of the Society.

We have our usual "MicroBusiness" column, which shows how failure can be considered a positive outcome; a review of a book on phased-array antennas; and a "New Products" column introducing new microwave-related components that may be of interest to you. Our "Enigmas, etc." column presents a new problem for you to tackle as part of Dr. Ohira's continuing series on switching power amplifier fundamentals. In addition, our "MTT-S Society News" column covers the activities of the MTT-S Kerala, India,

Chapter, which include continuing technical presentations in the Chapter's "Learn From Leaders, Learn From Legends" remote seminar series as well as the inauguration of a new Student Branch Chapter.

Finally, we have a report on the passing of Dr. George Matthaei. In addition to being the recipient of the MTT-S Microwave Prize and Microwave Career Award, he was the coauthor of the seminal book *Microwave Filters, Impedance-Matching Networks, and Coupling Structures*, which many microwave engineers have on their bookshelves and is a standard reference among microwave engineering textbooks. You can read about his life and career in our "In Memoriam" column. He will be greatly missed by the Society.





MTT-S Society News

Inauguration of the GECBH Student Branch Chapter and L4 Talk Series

■ Chinmoy Saha

The Kerala, India, Chapter of the IEEE Microwave Theory and Techniques Society (MTT-S) initiated a Learn From Leaders, Learn From Legends (L4) talk session as well as a Student Branch Chapter (SBC) at the Government Engineering College, Barton Hill (GECBH) during an online ceremony held 17 September 2020 (Figure 1). In attendance were

- Dr. Alaa Abunjaileh (2020 MTT-S president)
- Dr. Rashaunda Henderson (chair, MTT-S Education Committee)
- Dr. Ramesh Gupta (former chair, MTT-S Education Committee)
- Dr. Shibam Koul (IEEE MTT-S Region 10 coordinator)
- Dr. Ajay Poddar [IEEE Antennas and Propagation Society and MTT-S Administrative Committee (AdCom) member]
- Dr. Goutam Chattopadhyay (MTT-S AdCom member)

- Dr. Nuno Borges Carvalho (chair, MTT-S Member and Geographic Activities Committee)
- Dr. D.C. Pande
- Dr. Jawad Y. Siddiqui
- Dr. Chinmoy Saha (associate professor, Department of Avionics, Indian Institute of Space Science

and Technology and chair of the MTT-S Kerala Chapter)

- Shri Anu Mohamed (faculty advisor, MTT-S GECBH).

Dr. Saha described the L4 initiative's operation during the pandemic lockdown and highlighted how the multiple themes of the series, such as focused technical talks by seasoned experts, focused colloquiums, and panel discussions, would cater to and benefit students and young researchers. After a short video presentation by Saha on MTT-S Kerala Chapter activities and a Power Point presentation by Shri Arijit Mitra (Vikram Sarabhai Space Center, Kerala), Ms. Shri Sivada, and Ms. Shri Gopika, Dr. Abunjaileh opened the L4 series and the GECBH SBC. Abunjaileh expressed his appreciation for the unique initiation of the MTT-S Kerala Chapter and ensured the full support of the MTT-S for this and any such future activities.

To mark the occasion, a presentation slide symbolizing the dedication of the GECBH SBC and the L4 series was displayed (Figure 2). Dr. Henderson, Dr. Gupta, Dr. Borges Carvalho, Dr. Koul, Dr. Poddar, Dr. Chattopadhyay, Dr. Pande, and Dr. P.S. Birenjith greeted and addressed the community. Prof.



©SHUTTERSTOCK.COM/INGO MENHARD

Chinmoy Saha (csaha@ieee.org) is the IEEE Microwave Theory and Techniques Society Kerala Section Chapter chair.

Digital Object Identifier 10.1109/MMM.2020.3042047
Date of current version: 3 February 2021

The event fostered excellent interaction among MTT-S leaders, technical speakers, and attendees, and the feedback was positive.

Mohammed, Shri Mitra, and Akshat A. Philip (chair, GECBH SBC) expressed their gratitude. Koul (Indian Institute of Technology Delhi) delivered a webinar about the role of MTT-S volunteers in shaping the future of engineering students after COVID-19.

The inauguration was followed by the first L4 talk, "Energy-Efficient Simultaneous Wireless Backscatter and Power Communications," by Dr. Borges Carvalho (Instituto de Telecomunicacoes, Universidade de Aveiro, Portugal). The talk was moderated by Dr. Saha and focused on efficient system designs and adaptations in the power communications field. The highly successful event was attended by 150 participants from around the globe, including professional MTT-S members, scientists from the Indian Space Research Organization, and academics, faculty members, and students from various colleges. The proceedings were



Figure 1. MTT-S leaders and local organizers inaugurate the L4 series and the GECBH SBC.



Figure 2. The dedication slide for the L4 series and GECBH SBC.

streamed live on YouTube. In summary, the event fostered excellent interaction among MTT-S leaders, technical

speakers, and attendees, and the feedback was positive.



Are You Moving?



Don't miss an issue of this magazine—update your contact information now!

Update your information by:

E-MAIL: address-change@ieee.org

PHONE: +1 800 678 4333 in the United States
or +1 732 981 0060 outside the United States

If you require additional assistance regarding your IEEE mailings, visit the IEEE Support Center at supportcenter.ieee.org.



© ISTOCKPHOTO.COM/BRIANAJACKSON



IMS

Connecting Minds. Exchanging Ideas.

IEEE MTT-S
INTERNATIONAL
MICROWAVE
SYMPOSIUM

IMS2021

EXHIBITION & SPONSORSHIP PREVIEW

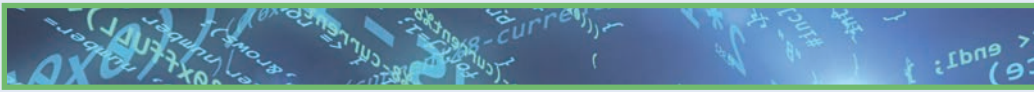


Digital Object Identifier 10.1109/MMM.2021.3049937

6-11 June 2021
ATLANTA • GEORGIA
www.ims-ieee.org/ims2021



MTT-S™
IEEE MICROWAVE THEORY &
TECHNIQUES SOCIETY



Join us in Atlanta, as we come together once again for the world's premier RF and microwave industry conference and tradeshow: IMS2021. Now in its 64th year, IMS is the place to be each year for professionals buying and developing materials, devices, components, systems, design & simulation software, and test & measurement equipment for products operating from RF to THz.

9000 participants from over 50 countries include senior management, engineering management, engineers, and R&D personnel from academia, commercial industry, and government/military. Participating exhibitors can establish new US and international connections, present products directly to industry leaders, and see the state of the art in a showcase of the best developments for applications that enable us to connect for a smarter, safer world.

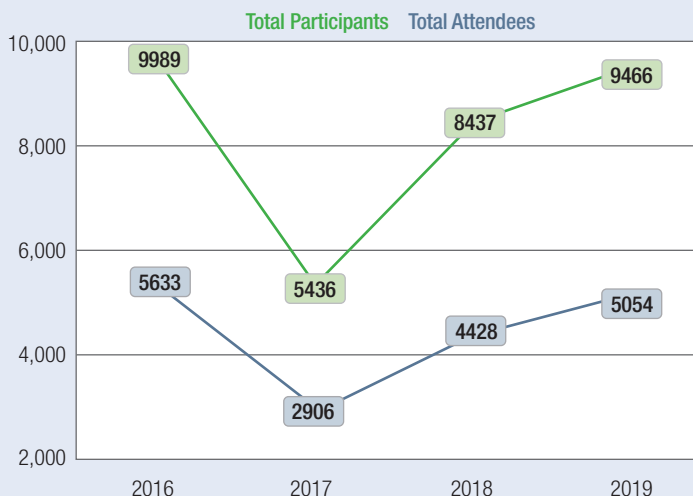
Georgia World Congress Center

In the heart of Atlanta, the Georgia World Congress Center is at the forefront of the meeting industry, on the vanguard of event health and safety, and offers these features and benefits:

- Largest combined convention, sports, and entertainment campus in North America
- 220 acres anchored by Georgia World Congress Center, Centennial Olympic Park, and Mercedes-Benz Stadium
- 12,000 hotel rooms within walking distance
- 1.5 million square feet of prime exhibit space
- World's largest LEED certified convention center
- Ample meeting space for exhibitor meetings
- Branding opportunities within the facility
- Wi-Fi throughout the facility
- Inexpensive Public Transportation via Metropolitan Atlanta Rapid Transit Authority (MARTA) from Atlanta area and Hartsfield-Jackson Atlanta International Airport to GWCC/CNN Station (W-1)

Reserve your IMS exhibition booth today!

Attendee Snapshot
IMS Four Year Attendance Numbers



Contact your sales representative or exhibits@horizonhouse.com to discuss exhibit and sponsorship opportunities at IMS2021.

Why Become a Sponsor at IMS 2021?

Beyond the Booth:

Market to attendees throughout the convention center, inviting them to your booth on the show floor. Whether you are looking to promote a product, build your brand, or connect with customers, a sponsorship helps raise your profile. Our expert sales team can help you construct the sponsorship plan that best meets your marketing goals.

Expo Floor – Exhibit Options

Exhibitor Benefits

Exhibitors will enjoy the following benefits before, during and after the conference:

Pre-Show:

- An IMS exhibitor console. Dedicated area to showcase your profile.
- Access to 2021 promotional opportunities
- Choice of hotel accommodations including hospitality suites and meeting space

On-Site:

- A listing in the official Conference Program/Exhibition Catalog
- Priority space selection for the IMS2022
- Access to discounted conference registrations
- General exhibit hall security service
- Daily aisle cleaning service

Post-Show:

- Post-event report with conference audit and attendee demographics

STANDARD EXHIBIT BOOTH

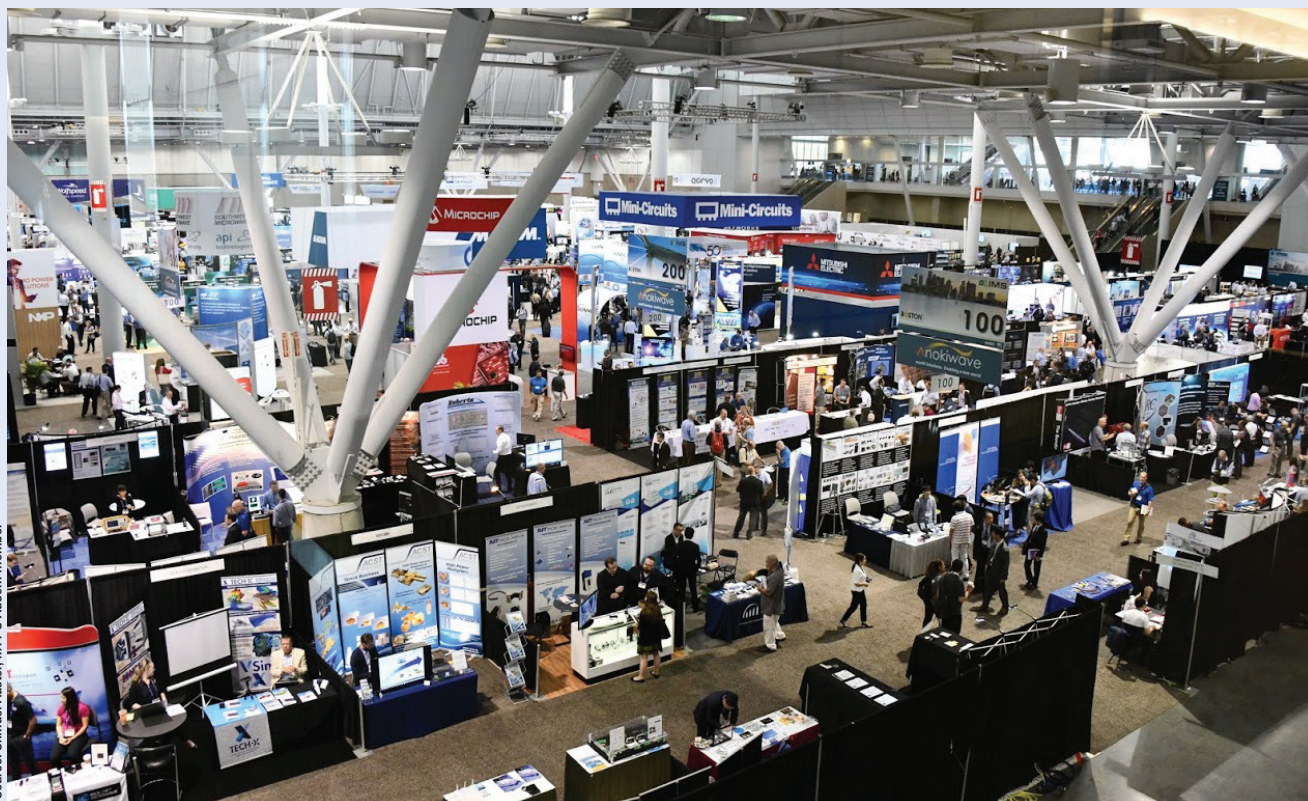
IMS2021 Exhibit Space is \$3,800 per 10x10 booth.

- Illuminated exhibit space with 8' high backwall drape if needed and 3' high side rails (in-line booths only).
- A 7" x 44" identification sign with the exhibitor's name and booth number (in-line booths only).
- Furnished booth packages and booth decor available in the Exhibitor Manual through the event decorator.

5G Pavilion

The 5G pavilion offers a special turnkey position on the show floor to introduce and showcase your 5G products. All participants receive the following for \$3,400:

- 6ft draped table, 2 chairs and electrical
- Identified as a 5G Pavilion participant on all 5G signage
- Promotional listing on the 5G web page, pages in the printed Conference Program/Exhibition Catalog
- Highlighted in IMS attendee promotions and featured on IMS website
- Option to lead a talk in the theater on 5G



Source: Simuel Auster, MTT-S AdCom member



IMS

Connecting Minds. Exchanging Ideas.

For details, visit: <https://ims-ieee.org/ims2021>



SALES REPRESENTATIVES

For General Inquiries

Call (781) 619-1994
or email
exhibits@horizonhouse.com

Eastern and Central Time Zones

Michael Hallman
Sales Manager
4 Valley View Court
Middletown, MD 21769
Tel: (301) 371-8830
FAX: (301) 371-8832
mhallman@horizonhouse.com

Pacific and Mountain Time Zones

Brian Landy
Western Reg. Sales Mgr.
(CA, AZ, OR, WA, ID, NV, UT, NM, CO, WY,
MT, ND, SD, NE & Western Canada)
144 Segre Place
Santa Cruz, CA 95060
Tel: (831) 426-4143
FAX: (831) 515-5444
blandy@horizonhouse.com

International Sales

Richard Vaughan
International Sales Manager
16 Sussex Street
London SW1V 4RW, England
Tel: +44 207 596 8742
FAX: +44 207 596 8749
rvaughan@horizonhouse.co.uk

Germany, Austria, and Switzerland

(German-speaking)
WMS Werbe- und Media Service
Brigitte Beranek
Gerhart-Hauptmann-Street 33,
D-72574 Bad Urach
Germany
Tel: +49 7125 407 31 18
FAX: +49 7125 407 31 08
bberanek@horizonhouse.com

France

Gaston Traboulsi
Tel: 44 207 596 8742
gtraboulsi@horizonhouse.com

Israel

Dan Aronovic
Tel: 972 50 799 1121
aronovic@actcom.co.il

Korea

Young-Seoh Chinn
JES MEDIA, INC.
F801, MisahausD EL Tower
35 Jojeongdae-Ro
Hanam City, Gyeonggi-Do 12918 Korea
Tel: +82 2 481-3411
FAX: +82 2 481-3414
yschinn@horizonhouse.com

China

Shenzhen
Michael Tsui
ACT International
Tel: 86-755-25988571
FAX: 86-755-25988567
michaelt@actintl.com.hk

Shanghai

Linda Li
ACT International
Tel: 86-021-62511200
lindal@actintl.com.hk

Beijing

Cecily Bian
ACT International
Tel: +86 135 5262 1310
cecilyb@actintl.com.hk

Hong Kong, Taiwan, Singapore

Mark Mak
ACT International
Tel: 852-28386298
markm@actintl.com.hk

Japan

Katsuhiko Ishii
Ace Media Service Inc.
12-6, 4-Chome,
Nishiiko, Adachi-Ku
Tokyo 121-0824, Japan
Tel: +81 3 5691 3335
FAX: +81 3 5691 3336
amskatsu@dream.com

CONNECTING FOR A SMARTER, SAFER WORLD



New Products

■ Ken Mays, Editor

Products listed in *IEEE Microwave Magazine* are restricted to hardware, software, test equipment, services, applications, and publications for use in the science and practice of RF/microwave or wireless engineering. Product information is provided as a reader service and does not constitute endorsement by IEEE or the IEEE Microwave Theory and Techniques Society. Absolute accuracy of listings cannot be guaranteed. Contact information is provided for each product so that interested readers may make inquiries directly.

Please submit "New Products" column information to microwave.newproducts@ieee.org.

Welcome to a further installment of the "New Products" column in *IEEE Microwave Magazine*. In this issue, we present six items that may be of interest to the RF/microwave and wireless communities.

Bidirectional SSPA Supports CW/FM and QAM Signals

Triad RF Systems has announced the development of a dual bidirectional amplifier that supports 2×2 multiple input, multiple output (MIMO) radio applications. Model TTRM2005D is a solid-state power amplifier (SSPA) that operates at a frequency of 2,200–2,500 MHz. It is designed for military and com-

mercial use and supports a variety of signal types, from simple continuous wave/frequency modulation (CW/FM) signals to complex, highly modulated carriers, such as 64 and 256 quadrature amplitude modulation (QAM).

The technical features of each channel on this dual bidirectional amplifier include a transmit (Tx) signal gain of 25 dB, a receive (Rx) signal gain of 12 dB, an Rx noise figure of 2.5 dB, and ~20-W binary phase-shift keying power $\times 2$ (40 W off the total RF power). Supply voltage is an ultrawide 12–30 Vdc. Using the latest laterally diffused metal-oxide semiconductor (LDMOS) transistor technology, it's capable of either achieving highly linear power with low distortion or performing at peak power with extremely high efficiencies. Its operational features

include manual or automatic Tx/Rx switching, temperature monitor output, over-temperature protection, and amplifier status output. It measures 3.4 in \times 2.6 in \times 0.65 in and weighs just 5 ounces, making it the smallest standardized amplifier of its kind.

In addition to the MIMO radio, further applications for this class-AB LDMOS SSPA module include other military and commercial radio systems, software-defined radios, and general-purpose RF amplification. It is capable of supporting any signal type and modulation format, including 3G and 4G telecom, wireless local area network, orthogonal frequency-division multiplexing, digital video broadcasting, QAM, and CW/amplitude modulation/frequency modulation technologies.

Learn more about the innovative TTRM2005D dual bidirectional SSPA at



Digital Object Identifier 10.1109/MMM.2020.3042029
Date of current version: 3 February 2021

<https://triadrf.com/updates/bi-directional-sspa-supports-cwfm-and-qam-signals/>.

Pasternack Introduces New, Highly Flexible VNA Cables Supporting Frequencies Up to 70 GHz

Pasternack, an Infinite Electronics brand and a leading provider of RF, microwave, and millimeter wave products, has launched a new line of highly flexible vector network analyzer (VNA) test cables designed to address a wide range of demanding lab and test applications.

Pasternack's new, highly flexible VNA test cables display excellent electrical properties, such as an exceptional phase stability of $\pm 6^\circ$ C at 50 GHz and $\pm 8^\circ$ C at 70 GHz with flexure as well as a voltage standing-wave ratio (VSWR) of 1.3:1 at 50 GHz and 1.4:1 at 70 GHz. The new 50-GHz assemblies are terminated with 2.4-mm connectors, while the 70-GHz assemblies utilize 1.85-mm connectors. The braided stainless steel armoring surrounding the coaxial provides a rugged yet flexible cable with a flexure life exceeding 100,000 cycles, making these test cables ideal for use in precise benchtop testing, semiconductor probe testing, and lab/production testing where the requirement for a durable yet highly flexible cable solution is a must.

These new VNA test cables are terminated with rugged stainless steel connectors that provide up to 5,000 mating cycles when attached with proper care. Both the 50- and 70-GHz versions are offered with NMD-style connectors, which are often used on test sets and network analyzers. Additionally, the flexibility of these cables makes it easier and safer to test a device under

test (DUT). Swept, right-angle 2.4- and 1.85-mm connector options allow these cables to fit into tight spaces and reduce the length of cable, as required in many applications. These new VNA test cables not only offer performance up to 70 GHz but can also withstand 100,000 flexure cycles while still exhibiting excellent phase stability and amplitude to the given frequency.

For inquiries, contact Pasternack by telephone at +1-949-261-1920.

B&K Precision Launches New 5.5 and 6.5 Digit Bench Multimeters



B&K Precision, a leading designer and manufacturer of reliable, cost-effective test and measurement instruments, announces a new generation of 5.5 and 6.5 digit benchtop multimeters designed for accuracy, repeatability, and ease of use. Both the 5492C (5.5) and 5493C (6.5) models deliver measurement speeds up to 1,000 readings per second and support 12 measurement functions, while the 6.5 digit model provides greater accuracy, higher resolution, and rear input terminals to simplify connections.

The easy-to-read, 4.3-in LCD offers a variety of measurement display modes, including numeric, bar meter, trend chart, and histogram. Other built-in functions include the limit mode to quickly verify that measurements are within a user-defined range, probe hold mode to capture a sequence of stable readings, and dual measurement capabilities.

The 5490C series provides USB (USBTMC-compliant), local area network, and RS232 interfaces standard with an optional General Purpose Interface Bus. The included operating software supports remote instrument control, measurement, monitoring, and data logging. A LabVIEW driver

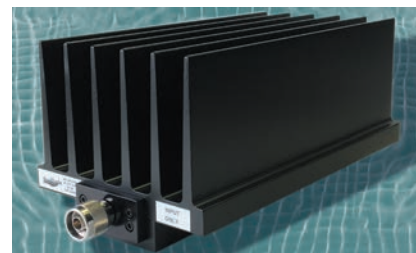
is available for download to help simplify system integration and instrument control.

For additional technical specifications, accessories, photos, and support documents, visit <https://www.bkprecision.com/products/multimeters/5492C-5-1-2-bench-digital-multimeter.html>.

New BroadWave 500-W Fixed Attenuator Line

BroadWave Technologies introduces a new line of high-power fixed attenuators. Model series 352–363 are 50- Ω fixed attenuators rated 500-W average power with 1.45:1 maximum VSWR. The operating frequency range is dc–8.5 GHz; attenuation values are 10, 20, 30 and 40 dB; operating temperature range is -55° C to $+125^\circ$ C; and RF connectors are N male input, N female output. Useful for analyzing harmonic signals or isolating a DUT, these attenuators reduce the amount of power delivered in a transmission line without introducing much noise or distortion. Applications include test equipment, telecommunication systems, base stations, radar applications, and high-precision applications such as military and defense programs. There is an application note available in the support section of our website.

For additional information visit www.broadwavetechnologies.com.



Fairview Microwave Introduces a New Series of Biphasic Modulators Operating in 0.5–40-GHz Frequency Bands

Fairview Microwave Inc., an Infinite Electronics brand and a leading provider of on-demand RF, microwave, and millimeter wave components, has



released a new line of biphas modulators covering broad octave frequency bands from 0.5 to 40 GHz. These models use transistor-transistor logic (TTL) to phase-modulate data onto an RF carrier signal using two-phase shift keying (2PSK). Applications include military and commercial communications systems, microwave radio, radar, high-data-rate test and measurement, serial data transmission, and wireless base station infrastructure.

Fairview Microwave's new series of 0° to 180° C biphas modulators includes nine models that offer impressive performance such as a low insertion loss of 2.5-dB, a fast switching speed of 40-nsec, a low VSWR of 1.8:1, and maximum peak RF input power of 0.5 W. All designs require dual-bias voltages, and input and output RF ports are bidirectional. These compact and rugged packages utilize solder pins for TTL control, dc bias and ground, and field-replaceable or 2.92-mm female connectors. They operate across a wide temperature range, from -40 °C to +85 °C. All models are highly reliable, meeting Mil-Std-202 environmental test conditions for humidity, shock, vibration, altitude, and temperature cycle. Same-day shipping is available, avoiding the usual 22-24 week production lead times.

For inquiries, contact Fairview Microwave by telephone at +1-972-649-6678.



Rohde & Schwarz First to Bring 1-GHz Analysis Bandwidth to a Midrange Signal and Spectrum Analyzer

Manufacturers of future cellular and wireless systems, infrastructure, and amplifiers can now profit from a wide-band signal test solution that was previously available only in high-end instruments. Rohde & Schwarz (R&S) has added an unparalleled internal analysis bandwidth of up to 1 GHz to its R&S FSVA3000 midrange signal and spectrum analyzer. The new R&S FSV3-B1000 hardware option is available for all models, from 7.5 to 44 GHz, while comparable solutions offer just 160-MHz analysis bandwidth.

Thanks to its usability and high measurement speed, the R&S FSVA3000 supports manufacturers in the development and production of 5G New Radio (NR) base stations, mobile phones, and components, especially in the 28- and 39-GHz bands, while meeting tight time-to-market requirements. In combination with the supported 5G NR downlink and uplink measurement options, this makes the R&S FSVA3000 a solution that is easy to set up for analyzing 5G NR signals with several component carriers. The

instrument, which also addresses users in aerospace and defense and automotive applications, can characterize wide-band amplifiers or be used for troubleshooting, capturing even very short events.

The R&S FSVA3000, which comes with an advanced autoset feature allowing the quick configuration of frequently performed measurements, now offers sufficient bandwidth for scanning electron microscope and adjacent channel leakage ratio measurements of wide-band signals as well as in in-phase/quadrature mode. The analyzer's outstanding RF performance allows capture, predistortion (for instance, a 200-MHz-wide signal), and measurement of the effects of distortion up to the fifth harmonic. The R&S FSVA3000 also supports measurement of short rise and fall times (down to a 1-ns system rise time) and detection of ultrashort pulses. This allows analysis of frequency-agile signals within 1 GHz as used in radar and tactical radio.

The new R&S FSV3-B1000 1-GHz analysis bandwidth option for the R&S FSVA3000 is now available. For further information, visit R&S at <https://www.rohde-schwarz.com/product/fsva3000>.





IEEE MTT-S International Conference on Microwave Acoustics & Mechanics

July 19–21, 2021, Munich, Germany

Conference General Chair

Amelie Hagelauer

Universität Bayreuth
Bayreuth, Germany
chairs.icmam@mtt.org

Conference General Co-Chair

Andreas Tag

Qorvo
Apopka, FL, USA

Technical Program Chair

Holger Maune

Technische Universität Darmstadt
Darmstadt, Germany
tpc.icmam@mtt.org

Technical Program Co-Chair

Andreas Link

Qorvo
Munich, Germany

Songbin Gong

University of Illinois
Urbana, IL, USA

Conference Finance Chair

Stefan J. Rupitsch

Friedrich-Alexander-Universität
Erlangen-Nürnberg, Germany
finance.icmam@mtt.org

Venue

**Rohde & Schwarz
Training Centre Munich**

Sponsor

ROHDE & SCHWARZ
Make ideas real



Call for Papers

The International Conference on Microwave Acoustics & Mechanics (IC-MAM) represents a unique and unprecedented opportunity to bring together researchers and practitioners of different background (materials scientists, physicists, microwave engineers and process technologists), to share the most recent advances in new materials and manufacturing processes as well as components and devices, which represent the key for the development of future RF, microwave, mm-wave and THz devices, circuits and systems based on RF-MEMS and Acoustics. IC-MAM is organized by the IEEE Microwave Theory and Techniques Society (MTT-S) and features an exciting technical program and invited talks by worldwide recognized experts of RF-MEMS and BAW/SAW technologies.

Conference Topics

Perspective authors are cordially invited to submit papers in all areas of Microwave Acoustics and RF MEMS including but not limited to:

- Acoustic/MEMS Device Applications
- Acoustic/MEMS Device Design
- Acoustic/MEMS Device Modeling
- Materials & Propagation
- Advances in Filter and Multiplexer Technology
- SAW and BAW Sensor Devices and Applications
- Multi-Band RF Modules for Multi-Standard/-Mode Systems
- Fusion of Major Transmit and Receive Functionality in Single Modules
- Tunable & Reconfigurable Devices, like Bulk and Thin-film Components and Devices, e.g., based on Ferroelectrics, Phase-Change Materials

Submitted papers should be three to four pages in length. Authors must adhere to the format of the IEEE conference paper template.

Submission deadline:	April 12, 2021
Notification of acceptance:	May 11, 2021
Final paper submission:	May 31, 2021
Conference date:	July 19–21, 2021

Technical Sponsor

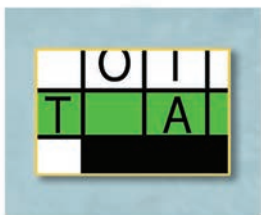


Technical Co-Sponsors



<http://www.icmam-ieee.org>





Enigmas, etc.

Sinusoidal Wave Output

■ Takashi Ohira

To create a power amplifier with a sinusoidal wave output, a series inductor-capacitor resonator is added to the sawtooth wave generator described in last month's "Enigmas, etc." column (see Figure 1). The resonator enables only the fundamental harmonic wave to flow. Hence, we can write the output current waveform as

$$i(t) = I_P \sin \omega t + I_Q \cos \omega t, \quad (1)$$

where ω denotes the switching angular frequency and $\omega = 2\pi/T$. Coefficients I_P and I_Q represent the sinusoidal in-phase and quadrature components.

The resonator functions not only as a filter but also as a reactor. By carefully adjusting the reactance, we can nullify the transistor's collector voltage at the time of turning it on and thus avoid an undesired surge current and switching power loss. This is called the *zero-voltage-switching (ZVS)* condition [1]–[5]. When the reactance is adjusted to meet the ZVS condition, we observe a specific dc-to-RF current proportion. Now, given the dc input current I_{dc} , find the specific I_P among the following candidates:

- a) πI_{dc} b) $\frac{\pi}{2} I_{dc}$ c) $\frac{\pi}{3} I_{dc}$ d) $\frac{\pi}{4} I_{dc}$.

Solution to Last Month's "Enigmas, etc." Challenge

Recall the sawtooth-like voltage waveform. Focusing on the time interval $0 < t < T/2$, the shunt capacitor's voltage increases linearly as

Takashi Ohira (ohira@tut.jp) is with Toyohashi University of Technology, Aichi, Japan. He is a Life Fellow of IEEE.

Digital Object Identifier 10.1109/MMM.2020.3042048
Date of current version: 3 February 2021

$$v(t) = \frac{8V_{dc}}{T} t. \quad (1)$$

According to this voltage, the energy

$$\begin{aligned} U &= \int_0^{\frac{T}{2}} v(t) I_{dc} dt = \int_0^{\frac{T}{2}} \frac{8V_{dc} I_{dc}}{T} t dt \\ &= \frac{8V_{dc} I_{dc}}{T} \left[\frac{1}{2} t^2 \right]_0^{\frac{T}{2}} = V_{dc} I_{dc} T \end{aligned} \quad (2)$$

is accumulated in the shunt capacitor. This is consistent with the law of energy conservation because the final right-hand side of (2) refers to the dc energy supplied

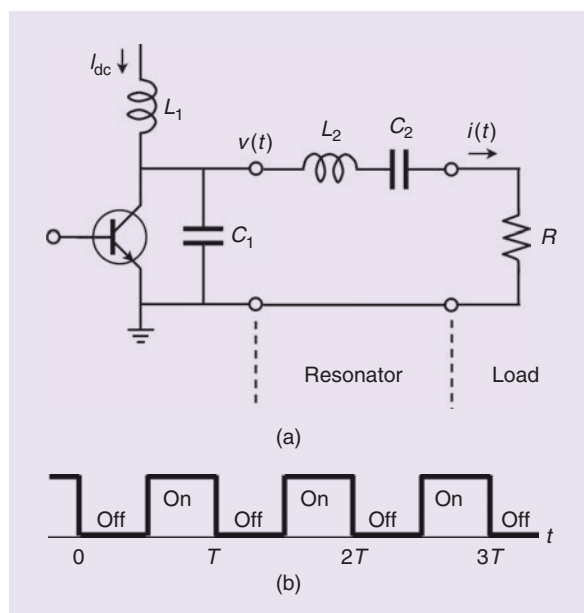


Figure 1. The switch-mode power amplifier that outputs a sinusoidal wave. (a) The circuit scheme. (b) The base input signal.

to the circuit for a period T . In other words, there is no dissipation of power inside the circuit, at least before the transistor turns on. We then recall the dc voltage-to-current relation

$$I_{dc} = \frac{8CV_{dc}}{T} \quad (3)$$

from last month's solution. Substituting (3) into (2), we obtain

$$U = 8CV_{dc}^2. \quad (4)$$

When the transistor turns on, power dissipation takes place abruptly. The stored energy U instantaneously disappears at the moment when the shunt capacitor is short-circuited by the transistor. This event periodically repeats f times per second, where f stands for the transistor's switching frequency: $f = 1/T$. Therefore, the power dissipation P in question counts

$$P = fU = 8fCV_{dc}^2. \quad (5)$$

We thus conclude that the correct answer to last month's quiz is "d."

The preceding dissipated power P is called *turn-on loss* or *switching loss*, which is undesirable for system

applications because it causes excess heat generation and power efficiency degradation. A question may then arise as to whether we can really utilize such a problematic topology for practical RF power amplifiers. The answer is yes if we can convert the energy stored in the shunt capacitor into a sinusoidal wave and effectively redirect it to the output port. A clever idea of how to do that will appear in the next "Enigmas, etc." problem.

References

- [1] G. D. Ewing, "High-efficiency RF power amplifiers," Ph.D. Thesis, Oregon State Univ., Corvallis, Apr. 1965.
- [2] R. Redl, B. Molnár, and N. O. Sokal, "Class E resonant regulated DC/DC power converters: Analysis of operations, and experimental results at 1.5 MHz," *IEEE Trans. Power Electron.*, vol. PE-1, no. 2, pp. 111–120, Apr. 1986. doi: 10.1109/TPEL.1986.4766289.
- [3] R. E. Zulinski and K. J. Grady, "Load-independent class-E power inverters. I. Theoretical development," *IEEE Trans. Circuits Syst.*, vol. 37, no. 8, pp. 1010–1018, Aug. 1990. doi: 10.1109/31.56074.
- [4] A. Grebennikov and F. H. Raab, "A history of switching-mode class-E techniques," *IEEE Microw. Mag.*, vol. 19, no. 5, pp. 26–41, July–Aug. 2018. doi: 10.1109/MMM.2018.2821062.
- [5] T. Ohira, "Load impedance perturbation formulas for class-E power amplifiers," *IEICE Commun. Express*, vol. 9, no. 10, pp. 482–488, 2020. doi: 10.1587/comex.2020XBL0085.



Microwave Bytes (continued from page 15)

time was spent performing extensive "fine tuning" on the cascades of balanced modules. The amount of tuning time was something of a closely guarded issue, albeit much discussed internally. Quite apart from the economics of the process, there were tricky documentation issues as well; every unit was strictly speaking a "special" inasmuch as the tuning pad (and/or silver paint) placements were not the same every time; "discretionary wiring," as I once heard a salesman euphemistically describe the process! But it posed some technical questions as well. Most notably, I remember being puzzled as to why we frequently appeared to be doing asymmetrical tuning inside the couplers; surely this would upset the

balanced behavior, we frequently asked. Well, the balanced modules did not always have a great VSWR over octave, or even greater bandwidths, and as such would be unbalanced by the imperfect termination looking into the next balanced stage. So I think the asymmetrical tuning was beneficial in restoring, to some extent, this effect.

It's nice to explain some of life's mysteries, albeit 30 years late. Talking of which, I should quote from Kurakawa's seminal paper [4], now 55 years old, concerning the subject: The requirements on the terminations which are connected to the couplers to absorb the transistor reflections are not stringent: VSWR's less than 1.4 should be acceptable. Just a bit optimistic, I would say.

References

- [1] S. C. Cripps, "Chasing Chebyshev [Microwave Bytes]," *IEEE Microw. Mag.*, vol. 8, no. 6, pp. 34–44, 2007. doi: 10.1109/MMM.2007.906917.
- [2] S. C. Cripps, "Couplers talk: Take 2 [Microwave Bytes]," *IEEE Microw. Mag.*, vol. 8, no. 2, pp. 34–41, 2007. doi: 10.1109/MMW.2007.335524.
- [3] L. S. Napoli and J. J. Hughes, "Characteristics of coupled microstrip lines," *RCA Rev.*, vol. 31, pp. 479–498, Sept. 1970.
- [4] K. Kurokawa, "Design theory of balanced transistor amplifiers," *Bell Sys. Tech. J.*, vol. 44, no. 8, pp. 1675–1698, 1965. doi: 10.1002/j.1538-7305.1965.tb04198.x.
- [5] J. Lange, "Interdigitated stripline quadrature hybrid," *IEEE Trans. Microw. Theory Tech.*, vol. 17, no. 12, pp. 1150–1151, 1969. doi: 10.1109/TMTT.1969.1127115.
- [6] D. J. Shepphard, J. Powell, and S. C. Cripps, "An efficient broadband reconfigurable power amplifier using active load modulation," *IEEE Microw. Wireless Comp. Lett.*, vol. 26, no. 6, pp. 443–445, 2016. doi: 10.1109/LMWC.2016.2559503.





Conference Calendar

Editor's Note: Please check the website of each conference for any changes to paper or workshop deadlines or conference dates and modality (in person, virtual, or hybrid).

APRIL 2021

2021 IEEE 21st Annual Wireless and Microwave Technology Conference (WAMICON)

14–16 April 2021

Location: Clearwater, Florida, United States (Virtual Conference)

MAY 2021

2021 IEEE Texas Symposium on Wireless and Microwave Circuits and Systems (WMCS)

18–20 May 2021

(Virtual Conference)

2021 IEEE MTT-S Latin America Microwave Conference (LAMC)

26–28 May 2021

Location: Cali, Colombia

JUNE 2021

2021 IEEE Wireless Power Transfer Conference (WPTC);

2021 IEEE PELS Workshop on Emerging Technologies: Wireless Power Transfer (WoW)

1–4 June 2021

Location: San Diego, California, United States

2021 IEEE Radio Frequency Integrated Circuits Symposium (RFIC)

6–8 June 2021

Location: Atlanta, Georgia, United States

2021 IEEE/MTT-S International Microwave Symposium—IMS 2021

6–11 June 2021

Location: Atlanta, Georgia, United States

2021 97th ARFTG Microwave Measurement Conference (ARFTG)

11 June 2021

Location: Atlanta, Georgia, United States

JULY 2021

2021 Fourth International Workshop on Mobile Terahertz Systems (IWMTS)

5–6 July 2021

Location: Essen, Germany

2021 IEEE MTT-S International Conference on Numerical Electromagnetic and Multiphysics Modeling and Optimization (NEMO)

7–9 July 2021

Location: Limoges, France

IEEE MTT-S International Conference on Microwave Acoustics and Mechanics (IC-MAM)

19–21 July 2021

Location: Munich, Germany

AUGUST 2021

2021 IEEE 19th International Symposium on Antenna Technology and Applied Electromagnetics (ANTEM)

8–11 August 2021

Location: Winnipeg, Manitoba, Canada

2021 46th International Conference on Infrared, Millimeter and Terahertz Waves (IRMMW-THz)

29 August–3 September 2021

Location: Chengdu, China

OCTOBER 2021

2021 32nd International Symposium on Space Terahertz Technology (ISSTT)

4–7 October 2021

Location: Baeza, Spain

2021 51st European Microwave Conference (EuMC), 2021 16th European Microwave Integrated Circuits Conference (EuMIC), and 2021 18th European Radar Conference (EuRAD)

11–15 October 2021

Location: London, United Kingdom

2021 IEEE 30th Conference on Electrical Performance of Electronic Packaging and Systems (EPEPS)

17–20 October 2021

Location: Austin, Texas, United States



IEEE Transactions on Microwave Theory and Techniques

Special Issue on

Microwave and Millimeter-Wave Communication and Sensor Systems

NEW Submission Date: 26 February 2021, Publication Date: October 2021

Motivation

The aim of this Special Issue is to publish technical papers in microwave and millimeter-wave communication and sensor systems. In recent years, we have seen a strong resurgence in such systems due to 5G and satellite communications, automotive radars, precise location services, UAV tracking, imaging radars, STAR (simultaneous transmit and receive systems also known as self-duplex), power amplifiers with digital pre-distortion, antenna tuning with closed loop functions, etc. Also, silicon chips are becoming more complex with multiple transmit and receive beamforming channels, up and down-conversion mixers, synthesizers, ADCs and DACs and even digital signal processing decision circuitry all on the same die. The silicon (and III-V front-end) solutions can be considered as stand-alone and are connected to antennas (or antenna arrays) for operation. For such complex systems, it is not required to know the detailed operation of every circuit or component, and it is more important to look at the solution from a systems perspective, such as co-design of the RF blocks with the antennas and with the DSP back-end, and the decision algorithms for the respective application areas. Also, calibration and test of such complex systems is critical, and novel techniques are needed to reduce the calibration cost which can lead to a reduction in system cost. The increased impact of microwave and millimeter-wave systems is noticeable throughout society, especially in 5G communications, automotive radars, safety/security applications, and in bio-medical sensors.

Topics of interest to be covered by the Special Issue include, but are not limited to

- *Systems and system-level demonstrations for communications and radar sensing*, including but not limited to: active and passive phased arrays using different beamforming technologies, MIMO arrays, repeaters, self-duplex and active nulling arrays, polarization diversity, closed-loop antenna tuning solutions, dual- or multi-band arrays, reconfigurable arrays, calibration and test techniques, etc. Applications for 5G, point-to-point links, SATCOM, automotive radars, position sensing, and other standards are especially welcome.
- *System-level integrated circuits and/or sub-systems using multiple chips*, including but not limited to: communication and radar chips with multi-channel transceivers, power amplifiers with wideband digital pre-distortion and envelope tracking, signal cancelling chips for self-duplex systems at the RF, IF and DSP level, and other complex systems on a chip. Circuits using solid-state (BiCMOS, SiGe, CMOS, SOI CMOS, GaAs, GaN and any combination) and non-solid-state technologies (RF MEMS, BST, liquid crystal, phase-change, etc.) are solicited.
- *Packaging and module technologies*, including but not limited to: complex packaging design for multifunction wideband systems, high power/thermal considerations, module technologies for receivers and transmitters, antennas-in-package and wafer-scale systems.
- *Review papers*, including but not limited to: papers summarizing the state of the art in automotive radars, SATCOM, 5G, point-to-point links, sensing systems, power amplifier digital predistortion, etc. are also encouraged. Potential authors should contact the editors to discuss their submission and to get approval for this special category.

Authors must consult the link <https://www.mtt.org/author-information-transactions/> for submission instructions.

Guest Editors

Prof. Gabriel M. Rebeiz

University of California, San Diego, USA

rebeiz@ece.ucsd.edu

Prof. James F. Buckwalter

University of California, Santa Barbara, USA

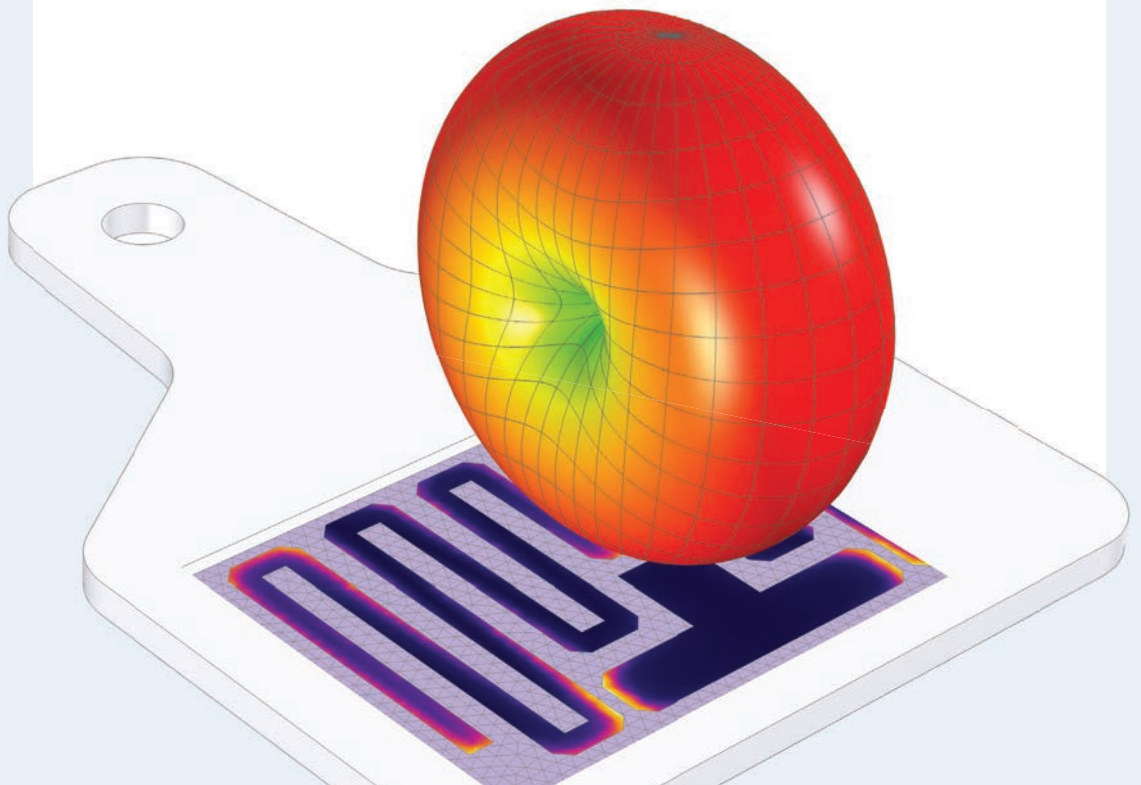
buckwalter@ece.ucsb.edu

SIMULATION CASE STUDY

Smartphones, smart homes, smart...healthcare?

RFID tags are used across many industries, but when it comes to healthcare, there is a major design challenge: size. If wearable RFID tags are too big and bulky, they could cause patient discomfort. Or, if the tag is for a biomedical implant, it has to be smaller than a grain of rice! Design engineers can optimize the size of an RFID tag for its intended purpose using RF simulation.

LEARN MORE comsol.blog/biomed-RFID-tags



The COMSOL Multiphysics® software is used for simulating designs, devices, and processes in all fields of engineering, manufacturing, and scientific research.